RARE-EARTH INTERMETALLIC COMPOUNDS FOR MAGNETIC APPLICATIONS

SYNTHESIS, STRUCTURAL AND MAGNETIC PROPERTIES OF RARE-EARTH INTERMETALLIC COMPOUNDS

BY

YAN YIN JANICE CHEUNG, B.Sc.

A Thesis

Submitted to the School of Graduate Studies

in Partial Fulfillment of the Requirements

for the Degree

Master of Science

McMaster University

MASTER OF SCIENCE (2012) McMaster University

Department of Chemistry and Chemical Biology Hamilton, Ontario

TITLE: Synthesis, Structural and Magnetic Properties of Rare-Earth Intermetallic Compounds

AUTHOR: Yan Yin Janice Cheung, B.Sc. (McMaster University)

SUPERVISOR: Professor Yurij Mozharivskyj

NUMBER OF PAGES: xi, 128

Abstract

Series of rare-earth intermetallic compounds were synthesized and studied.

The $Gd_4Ge_{3-x}Pn_x$ (*Pn* = P, Sb, Bi; x = 0.5 - 3) series of compounds were synthesized to explore the stability of the non-existent Gd_4Ge_3 binary through partial *Pn* substitutions to increase valence electron concentrations. Electronic band structure calculations were performed to elucidate the relationships between the hypothetical "Gd_4Ge_3" and Gd_5Ge_4 binaries. All $Gd_4Ge_{3-x}Pn_x$ phases order ferromagnetically with relatively high Curie temperatures of 234 to 356 K.

The $Gd_5Ge_{4-x}P_x$ phases were synthesized to explore the effects of both atomic size and valence electron concentration differences between Ge and P atoms. Partial substitution of P for Ge atoms occur on the interslab site, which causes the interslab distances to increase. In $Gd_5Ge_{4-x}P_x$, only a small amount of P substitution (x = 0.25) is required to induce ferromagnetic ordering. The appearance of a Griffiths phase is also discussed.

The temperature dependence of the different RE_2Fe_{17} (*RE* = Gd - Ho) phases was tracked by reciprocal space images generated from single crystal X-ray diffraction.

$GdCo_4B$ was synthesized by arcmelting and tri-arc techniques to confirm the presence of magnetostriction. Single crystal and powder X-ray diffraction, dilatometer and magnetic measurements were done.

Acknowledgments

First of all, I would like to thank my supervisor Dr. Yurij Mozharivskyj for all the guidance, coaching and support he has given me over the past four years of my studies at McMaster University. Thank you for always being understanding and patient with me. A big thank you to my supervisory committee member, Dr. John Greedan for all the helpful advice and comments. They were exceptional and invaluable to my research.

Next, I would like to thank former group member Dr. Volodymyr Svitlyk for all the help and supervision he has provided me during my undergraduate studies. Without him, many of my projects would not have existed. To my research group members, Dr. Jinlei Yao, Peng Wang and Scott Forbes, thank you for all the assistance and support over the years. To Dr. Tomoko Aharen and Dr. Farshid Ramezanipour, thank you for always bringing me joy and laughter.

I am very grateful to all the staff from BIMR and Department of Chemistry, especially Dr. Jim Britten for all the help and advice on X-ray crystallography, Dr. Paul Dube for the guidance in magnetic measurements and Dr. Hanna Dabkowska and Dr. Anton Dabkowski for all the kindness and support. I would also like to thank Debra Farquhar for always brightening up my day. I will always keep those encouragements in my heart.

A special thank you to Fan and Nicholas who have always been such great friends. To Nathan, I would never forget all the help, support and encouragements you have given

me over the years. Especially during my final undergraduate year, you gave me the courage and confidence that I needed when I was having doubts with my own capabilities.

Lastly, I would like to thank my family for all the support over the years. Mom and dad, I hope that both of you will be proud of my achievements. To Billy, I am grateful to have you as my brother, one who would always fight and argue with me but also one who can give me great advice whenever I need one.

Table of Contents

Chapter 1: Magnetism 1

1.1 Introduction 1

1.1.1 Magnetization and magnetic susceptibility 1

1.2 Origin of magnetism 4

1.2.1 Spin and orbital angular momentum 4

1.2.2 Magnetic moments 6

1.3 Temperature dependency of magnetic susceptibility 8

1.3.1 The Curie Law 8

1.3.2 The Curie-Weiss Law 9

1.3.3 Hysteresis 11

1.4 Magnetocaloric effect 13

1.4.1 Magnetic entropy 14

1.4.2 Thermodynamics of magnetocaloric effect 15

1.4.3 Magnetic refrigeration 17

1.4.4 Mechanism of magnetic refrigeration 18

1.4.5 Giant magnetocaloric effect and the RE_5T_4 phases 19

1.5 Magnetic susceptibility measurements 20

1.5.1 Superconducting QUantum Interference Device (SQUID) 20

1.5.2 Experimental set-up and measurements 21

Chapter 2: X-ray Diffraction 23

2.1 Introduction of X-ray diffraction 23

2.2 Characteristic X-ray spectra 23

2.3 Interplanar distance and miller indices 25

2.4 Bragg's Law 26

2.5 Reciprocal lattice and Ewald's sphere 27

2.6 Structure Factor 29

2.7 Fourier Transform 31

2.8 Powder X-ray diffraction 32
2.8.1 Origin of the powder diffraction pattern and Ewald's sphere 32
2.8.2 Sample preparation and experimental set-up 34
2.8.3 Rietveld refinement 34
2.9 Single crystal X-ray diffraction 36
2.9.1 Experimental set-up and measurements 36

Chapter 3: $Gd_4Ge_{3-x}Pn_x$ (*Pn* = P, Sb, Bi, x = 0.5 - 3): stabilizing the non-existing Gd_4Ge_3 binary through valence electron concentration. Electronic and magnetic properties of $Gd_4Ge_{3-x}Pn_x$ 38
3.1 Abstract 38
3.2 Introduction 39
3.3 Experimental 41
3.3.1. Synthesis and X-ray analysis 41
3.3.2 Quantitative elemental analysis 46
3.3.3 Band structure calculations 47
3.3.4 Magnetic measurements 49
3.4 Results and Discussion 49
3.4.1 Composition and stability of $Gd_4Ge_{3-x}Pn_x$ 49
3.4.2 Electronic structure 53
3.4.3 Magnetic properties of $Gd_4Ge_{3-x}Pn_x$ 55
3.5 Conclusions 58
3.6 Supporting Information 59

Chapter 4: Structural and magnetic properties of $Gd_5Ge_{4-x}P_x$ (x = 0.25 - 0.63) 67
4.1 Abstract 67
4.2 Introduction 67
4.3 Experimental 69
4.3.1 Synthesis and X-ray structure analysis 69
4.3.2 Electronic structure calculations 74

4.3.3 Magnetic measurements 74
4.4 Discussion 75
4.4.1 Homogeneity Region and Structural Properties of $Gd_5Ge_{4-x}P_x$ 75
4.4.2 Electronic band structure calculations of Gd_5Ge_3P 77
4.4.3 Magnetic properties of $Gd_5Ge_{4-x}P_x$ 80
4.5 Conclusions 88
4.6 Acknowledgements 88
4.7. Supporting Information 89

Chapter 5: Tracking the Th_2Zn_{17}- and Th_2Ni_{17}-type phases in RE_2Fe_{17} (*RE* = Gd - Ho) by single crystal X-ray diffraction 93
5.1 Abstract 93
5.2 Introduction 93
5.3 Experimental 96
5.3.1 Synthesis and X-ray analysis 96
5.3.2 Electron probe microanalysis (EPMA) 103
5.4 Results and Discussion 103
5.4.1 Phase composition of the RE_2Fe_{17} (*RE* = Gd - Ho) samples 103
5.4.2 Structural features and composition of the RE_2Fe_{17} (*RE* = Gd - Ho) phases 107
5.5 Conclusions 109

Chapter 6: Physical and magnetic properties of $GdCo_4B$ 110
6.1 Introduction 110
6.2 Experimental 111
6.3 Discussion 118
6.4 Conclusion 121

References 122

List of Figures

Figure 1.1 Different types of magnetism with positive susceptibilities represented in a two-dimensional system. 3

Figure 1.2 Vector model of the spin and orbital angular momenta for s = 1/2 and l = 2 5

Figure 1.3 Magnetic susceptibility of a paramagnet, ferromagnet and antiferromagnet 10

Figure 1.4 Hysteresis loop of a soft (left) and hard (right) ferromagnet. 12

Figure 1.5 The magnetocaloric effect (MCE) 14

Figure 1.6 Entropy plotted as a function of temperature and applied field. 16

Figure 1.7 Magnetic and conventional refrigeration cycles 19

Figure 2.1 (left) Intensity as a function of wavelength with varied applied voltages. (right) The characteristic X-ray spectra of a typical element consisting of K_α and K_β radiations. 25

Figure 2.2 A visual representation of the Bragg's law. The black dots correspond to atoms that sit on crystallographic planes with interplanar distance, d_{hkl}. 27

Figure 2.3 Visual representation of the relationship between the Ewald's sphere and the reciprocal lattice. 29

Figure 2.4 Cones of diffraction with corresponding Miller indices intersecting Ewald's sphere. 33

Figure 3.1 Lattice parameters vs. *Pn* amount in $Gd_4Ge_{3-x}Pn_x$ (*Pn* = P, Sb, Bi; x = 0.5 - 3). 46

Figure 3.2 Magnetization vs. temperature plots for $Gd_4Ge_{2.5}P_{0.5}$ (left), $Gd_4Ge_{3-x}Sb_x$ (x = 1 - 3) (center) and $Gd_4Ge_{3-x}Bi_x$ (x = 0.5 - 3) (right). 49

Figure 3.3 Density of States (DOS) and Crystal Orbital Hamilton Population (COHP) for Gd_4Sb_3 (left), Gd_4Ge_3 (center) and Gd_5Ge_4 (right). 55

Figure 3.4 Curie temperatures (T_C) as a function of the *Pn* amount for $Gd_4Ge_{3-x}Pn_x$ (*Pn*: P, Sb, Bi; x = 0 - 3). 57

Figure 4.1 The crystal structure of Sm_5Ge_4-type $Gd_5Ge_{4-x}P_x$. 71

Figure 4.2 (Top) Total and projected densities of states (DOS). (Bottom) Crystal orbital Hamilton population (COHP) plots for the interslab *T*1-*T*1 (solid blue line) and intraslab *T*2-*T*3 (dashed red line) interactions in Gd_5Ge_3P. 79

Figure 4.3 Magnetization of the cast (blue squares) and annealed (red circles) $Gd_5Ge_{4-x}P_x$ (x = 0.25, 0.5, 0.75) samples in the FC mode with a 100 Oe applied field. The Curie temperatures are denoted by T_c. 81

Figure 4.4 Field dependent magnetization measurements at 5 K for $Gd_5Ge_{3.75}P_{0.25}$, $Gd_5Ge_{3.5}P_{0.5}$ and $Gd_5Ge_{3.25}P_{0.75}$. 83

Figure 4.5 Inverse susceptibility vs. temperature for $Gd_5Ge_{4-x}P_x$ (x = 0.25, 0.5, 0.75) cast and annealed samples.....84

Figure 5.1 The parent $CaCu_5$-type structure (top), the Th_2Zn_{17} and the Th_2Ni_{17}-type structures with M/T planes stacked in the ABCABC sequences (bottom left) and ABABAB sequences (bottom right) respectively. 95

Figure 5.2 A graphical representation of the structural types present in the RE_2Fe_{17} (RE = Gd-Ho) phases. 97

Figure 5.3 A (*h*0*l*) layer image generated from a single crystal extracted from the Tb_2Fe_{17} sample annealed at 1000°C. 105

Figure 5.4 Several (*h*0*l*) layer images extracted from the Gd_2Fe_{17} and Ho_2Fe_{17} samples annealed at 850°C and 1250°C. 106

Figure 5.5 The visual crystallographic representation of Gd_2Fe_{17} and Ho_2Fe_{17} sample annealed at 850°C. 108

Figure 6.1 Crystal structures of the $GdCo_5$ (left) and $GdCo_4B$ (right) compounds.111

Figure 6.2 Linear thermal expansion data (ΔL) obtained from dilatometer measurement. 112

Figure 6.3 Refined lattice parameters *a* (top), *c* (middle) and unit cell volume (bottom) of the $GdCo_4B$ structure (with error bars) as a function of temperature ($450 \leq T \leq 700$ K). 114

Figure 6.4 Magnetization vs. Temperature plot for the $GdCo_4B$ cast sample under an applied field of 100 Oe. 117

Figure 6.5 Magnetization vs. Temperature plot for the $GdCo_4B$ tri-arc sample under an applied field of 100 Oe. 117

Figure 6.6 The refined powder X-ray pattern for the $GdCo_4B$ cast sample.....118

Figure 6.7 The refined powder X-ray pattern for the $GdCo_4B$ tri-arc sample. 119

List of Tables

Table 3.1 Crystallographic data and refinement results for the $Gd_4Ge_{2.51(5)}P_{0.49(5)}$, $Gd_4Ge_{2.49(3)}Bi_{0.51(3)}$ and $Gd_4Ge_{1.97(4)}Sb_{1.03(4)}$ single crystals. 43

Table 3.2 Atomic and isotropic temperature parameters (U, Å^2) for the $Gd_4Ge_{2.51(5)}P_{0.49(5)}$, $Gd_4Ge_{2.49(3)}Bi_{0.51(3)}$ and $Gd_4Ge_{1.97(4)}Sb_{1.03(4)}$ single crystals 44

Table 3.3 Compositions based on the EPMA, LA-ICP-MS and the X-ray single crystal analyses. 47

Table 3.4 Experimental distances for Gd_4Sb_3, Gd_4Bi_3 and calculated ones for Gd_4Ge_3. 52

Table 3.5 Curie temperatures (T_C, K) of $Gd_4Ge_{3-x}Pn_x$ (Pn = P, Sb, Bi; x = 0.5 - 3) ... 56

Table 4.1 Crystallographic and refinement data for the $Gd_5Ge_{4-x}P_x$ (x = 0.25, 0.5, 0.75) single crystals. 72

Table 4.2 Atomic and isotropic temperature parameters (U, Å^2) from single crystal refinements for $Gd_5Ge_{3.74(1)}P_{0.26(1)}$, $Gd_5Ge_{3.50(2)}P_{0.50(2)}$ and $Gd_5Ge_{3.37(2)}P_{0.63(2)}$. 73

Table 4.3 Magnetic ordering temperatures, calculated Weiss temperatures (θ) and effective magnetic moment (μ_{eff}) extracted from the paramagnetic data above T_G for the $Gd_5Ge_{4-x}P_x$ (x = 0.25 - 0.75) samples..... 75

Table 5.1 The lattice parameters (Å) from single crystal X-ray diffraction and the estimated amount of each phase. 98

Table 5.2 Single crystal data and structure refinement for Gd_2Fe_{17} and Ho_2Fe_{17}... 101

Table 5.3 Atomic and isotropic temperature parameters (U, Å^2) for $Gd_{1.967(7)}Fe_{17.07(8)}$ and $Ho_{1.89(1)}Fe_{17.2(1)}$ from single crystal diffraction data..... 102

Table 5.4 Results obtained from EPMA. 103

Table 6.1 Single crystal and refinement data obtained from the $GdCo_4B$ cast (left) and tri-arc (right) samples. 115

Table 6.2 Atomic and isotropic temperature parameters (U, Å^2) from single crystal X-ray diffraction data. 116

Chapter 1: Magnetism

1.1 Introduction

Magnetism is an intrinsic property that all materials exhibit. Depending on the nature of the material and its electron configuration, the magnitude of the magnetic response can vary greatly as an external magnetic field is applied. Magnets can be found everywhere, ranging from the needle of a compass to the naturally occurring minerals of the planet Earth itself, which is also a magnet. The history of magnetism can be dated back to over two millennia ago, before the discovery of electrons. Later, many physicists explained the behaviour of magnetic fields based on circular electric currents through a wire loop. However, the origin of magnetism was not fully understood until the use of quantum mechanics, a more modern field of science. This will be further discussed in the next section.

1.1.1 Magnetization and magnetic susceptibility

The total response inside a material is known as magnetic induction, *B*, or the magnetic flux density, which depends on the magnetic field, *H*, applied to the material and the induced magnetization, *M*, of the material itself. The relationship is shown in Eq. 1.1.1 in cgs (centimeter-gram-second) units, where the unit of magnetic induction, *B*, is in G (Gauss).

$$B = H + 4\pi M \tag{1.1.1}$$

Dividing Eq. 1.1.1 by the applied field, *H*, yields the magnetic susceptibility, χ. (Eq. 1.1.2). The susceptibility is commonly used to determine the magnetic behaviour of a material based on its response to an applied magnetic field.

$$\chi = \frac{M}{H} \tag{1.1.2}$$

Depending on the flux density difference between the inside and outside of the magnetic material and the attraction of the material to the magnetic field, the materials can be classified as paramagnetic or diamagnetic. Diamagnetic materials contain paired electrons that repel the magnetic field. Thus, the internal flux density is less than the external one. Conversely, if the internal flux density is greater than the external one, the materials contain unpaired electrons that are attracted to the magnetic field. This is known as paramagnetism. The former case has a small negative magnetic susceptibility ($\chi_D \sim -10^{-6}$ emu/mol) that is temperature and field independent. As such, it is only considered as a correction during the calculation of the experimental susceptibility. On the contrary, paramagnets have large positive susceptibility values ($\chi_P \sim 10^{-2} - 10^{-5}$ emu/mol) which are generally temperature dependent. The magnetic response inside these materials is present solely when an external magnetic field is applied. Once the field is removed, the magnetization also disappears.

In a zero magnetic field, the magnetic dipole moments in paramagnets are randomly oriented, which result in zero net magnetization (**Figure 1.1, top left**). At lower temperatures, the magnetic dipole moments can align in an ordered fashion, in which the material can be either ferromagnetic (**Figure 1.1, top right**), antiferromagnetic (**Figure**

1.1, bottom left) or ferrimagnetic (**Figure 1.1, bottom right**). Each individual arrow corresponds to a magnetic dipole moment, which holds both magnitude and direction. The magnetic dipole moments align in parallel fashion for ferromagnets and in antiparallel fashion for antiferromagnets and ferrimagnets. In antiferromagnets, the magnitudes of the moments in the different directions are identical whereas in ferrimagnets, the magnitude of one component is greater than the other, resulting in a net magnetization. Ferrimagnetism is often termed as "weak ferromagnetism" due to its similar net magnetization response with a ferromagnet in bulk. However, depending on the magnetic ions, the spontaneous magnetization in a ferrimagnet can be much smaller compared to a ferromagnet.

Generally, ferromagnetic materials have the strongest magnetic susceptibility ($\chi \sim 10^4$ emu/mol), being field and temperature dependent. Remanence and hysteresis are often characteristics of this class of materials. For antiferromagnets, their susceptibility is weaker than that of normal paramagnets and it is temperature and usually field dependent.

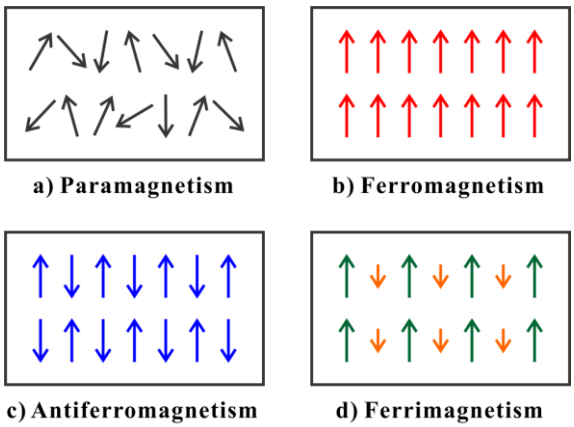

Figure 1.1 Different types of magnetism with positive susceptibilities represented in a two-dimensional system.

1.2 Origin of magnetism

As the magnetic field is applied, the response given by the material arises from the movement of the electrons. The intrinsic effects coming from the magnetic moments give rise to the macroscopic effects of magnetism that can only be explained using quantum mechanics. Therefore, the atom, which is the simplest unit of matter, must be first discussed to further explain the magnetic behaviour observed.

1.2.1 Spin and orbital angular momentum

In each atom, the negatively charged electrons orbit around the central nucleus. In the classical approach, the orbital motion of all the electrons create an electronic current that induces a magnetic field. In quantum mechanics, the origin of magnetism arises from both the spin and orbital motions of the electrons that precess quickly and indefinitely in orbits that resemble cones around the field direction. The orbits are quantized, which take only certain projections depending on the magnitude of the spin and orbital angular momenta. Under the presence of a magnetic field, both spin and orbital angular momenta precess in a cone around the field direction. Each electron spins around its own axis with a spin quantum number, s = 1/2. The magnitude of the spin angular momentum, $|S|$, of an electron can be represented in units of $\hbar$ by Eq. 1.2.1. The component of spin angular momentum along the field direction is given by $\pm m_s\hbar$, where m_s is the magnetic spin quantum number with values m_s = +1/2 and -1/2 respectively.

$$|S| = \sqrt{s(s+1)}\hbar \tag{1.2.1}$$

Aside from electrons residing in the s orbitals (l = 0), the orbital angular momentum of an electron has to be taken into consideration. The magnitude of the orbital

angular momentum, $|L|$, of an individual electron that precesses around the field direction in units of $\hbar$ can be calculated with Eq. 1.2.2, where l is the orbital momentum quantum number.

$$|L| = \sqrt{l(l+1)}\hbar \tag{1.2.2}$$

After determining l, the orbital magnetic quantum number, m_l, which is the component of orbital angular momentum along the field direction in units of $\hbar$ can also be calculated by using Eq. 1.2.3. An example of a vector model of the spin and orbital angular momenta for s = 1/2 and l = 2 is shown in **Figure 1.2**.

$$m_l = -l, (-l+1), \dots, (l-1), +l \tag{1.2.3}$$

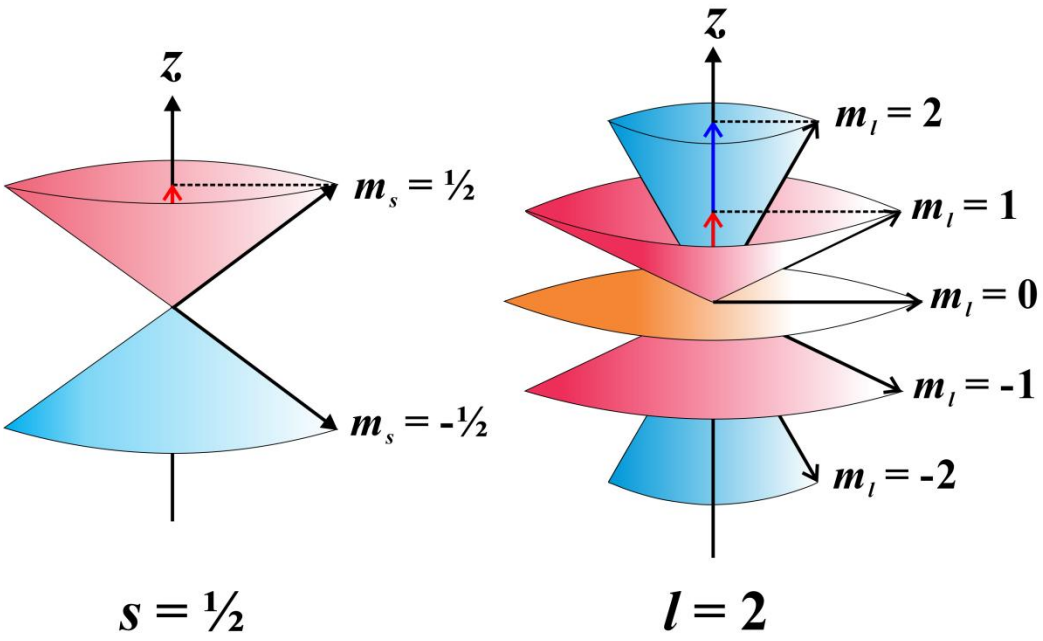

Figure 1.2 Vector model of the spin and orbital angular momenta for s = 1/2 and l = 2.

In light atoms, the sum of all the electron spins (*S*) and the sum of all the orbital angular momenta (*L*) combine separately to form the total angular momentum (*J*) (Eq. 1.2.4). This is known as the *Russell-Saunders coupling* or *LS coupling*.

$$J = S + L = \sum_i s_i + \sum_i l_i \tag{1.2.4}$$

In heavier atoms with larger nuclear charges, there are strong spin-orbit coupling interactions. Each individual electron spin (s_i) and angular momentum (l_i) first combine to form the individual total angular momentum (j_i). Then, these individual total angular momenta combine to form the total angular momentum (*J*) (Eq. 1.2.5). This is called the *jj coupling*.

$$J = \sum_i j_i = \sum_i (s_i + l_i) \tag{1.2.5}$$

1.2.2 Magnetic moments

Because of the negative charge of the electron, the magnetic moment vector is in opposite direction with the spin and orbital angular momenta. The component of the magnetic moment that precesses in a cone in the direction of the applied field can be represented by Eq. 1.2.6 or Eq. 1.2.7, depending if there are spin-orbit coupling interactions. These are saturated moments that can also be derived from the Brillouin function in Eq. 1.3.1.

$$\mu_{sat} = -(g_s S + L)\mu_B \tag{1.2.6}$$

$$\mu_{sat} = -g_J J \mu_B \tag{1.2.7}$$

$$g_J = \frac{3}{2} + \frac{S(S+1) - L(L+1)}{2J(J+1)} \tag{1.2.8}$$

The g-factor of an electron, g_s, is approximately equal to 2 in a free electron. The Landé splitting factor, g_J (Eq. 1.2.8), is a correction term that resulted from the non-collinearity of the magnetic moment (μ) and the total angular momentum (J). The Bohr magneton, μ_B, is an elementary unit of magnetic moment for an electron.

In light transition 3*d* metal ions, the strength of the crystal field splitting is much stronger than the spin-orbit coupling. The orbital angular momentum is quenched by the surrounding anions. Thus, the μ_{eff} gets reduced to the "spin-only" formula (Eq. 1.2.9). Although there are slight deviations between the calculated and experimental values, the "spin-only" model has shown to have the best agreement.

$$\mu_{eff} = \sqrt{4S(S+1)}\,\mu_B \tag{1.2.9}$$

In heavy transition metal and lanthanide ions, the spin and orbital angular momentum interactions increase for heavier atoms. There are strong spin-orbit coupling interactions. In the 4*f* elements, the effect from the crystal field splitting is relatively small due to the core nature of the 4*f* electrons. The effective magnetic moment (μ_{eff}) is calculated using the quantum number *J* (Eq. 1.2.10).

$$\mu_{eff} = g_J\sqrt{J(J+1)}\mu_B \tag{1.2.10}$$

This free ion approximation has been demonstrated to correspond well with experimental values.

1.3 Temperature dependency of magnetic susceptibility

1.3.1 The Curie Law

The applied field and temperature can be seen as two competing factors to the magnetic ordering of a material. The thermal energy prevents the alignment of magnetic moments with respect to the magnetic field. As mentioned, each magnetic moment can be expressed by Eq. 1.2.6 or Eq. 1.2.7. Here, we consider only the case of spin-orbital interactions with total angular momentum J in units of cgs. By summing up all the magnetic moments, the Brillouin function (indicated by rectangular bracket), is obtained where $\alpha = g_J J \mu_B H / k_B T$ and k_B = 1.3806503 x 10^{-23} $m^2 \cdot kg/s^2$ is the Boltzmann constant. The α term can be seen as the ratio of magnetic energy to thermal energy.

$$M = N g_J J \mu_B \left[\frac{2J+1}{2J} coth \frac{2J+1}{2J} \alpha - \frac{1}{2J} coth \frac{1}{2J} \alpha \right] = N g_J J \mu_B B_J(\alpha) \qquad (1.3.1)$$

At the high field or low temperature limit, $\alpha >> 1$, $B_J(\alpha) \rightarrow 1$ and magnetization is saturated. The equation will equal to Eq. 1.2.7. In the low field or high temperature limit, $\alpha << 1$, magnetization becomes Eq. 1.3.2.

$$M = N g_J \mu_B J(J+1) \frac{g_J \mu_B H}{3 k_B T} \qquad (1.3.2)$$

By dividing the above equation by the magnetic field, the magnetic susceptibility, χ, of a paramagnet known as the Curie Law is obtained (Eq. 1.3.3). The law states that χ and T are inversely proportional. In addition, the Curie constant, C, is derived (Eq. 1.3.4).

$$\chi = \frac{M}{H} = \frac{N g_J{}^2 \mu_B{}^2 J(J+1)}{3 k_B T} = \frac{C}{T} \qquad (1.3.3)$$

$$C = \frac{N g_J{}^2 \mu_B{}^2 J(J+1)}{3k_B} \tag{1.3.4}$$

1.3.2 The Curie-Weiss Law

The Curie Law can satisfy the behaviour of a simple paramagnet. In reality, most magnetic susceptibilities calculated from experiments do not obey the Curie Law. This discrepancy can be explained by the assumption of isolated magnetic moments and the lack of consideration of the magnetic interactions existing in the system. For ferromagnets, antiferromagnets or ferrimagnets, a correction term has to be added to the original Curie Law equation. The resulting equation is known as the Curie-Weiss Law (Eq. 1.3.5).

$$\chi = \frac{C}{T-\theta} \tag{1.3.5}$$

The θ term is known as the Weiss temperature. A positive value indicates that the material is ferromagnetic and a negative value denotes antiferromagnetism. For these materials, their magnetic behaviours are similar to paramagnets above their corresponding magnetic ordering temperatures. The temperature dependent magnetic susceptibilities for a paramagnet, ferromagnet and antiferromagnet are illustrated in **Figure 1.3**.

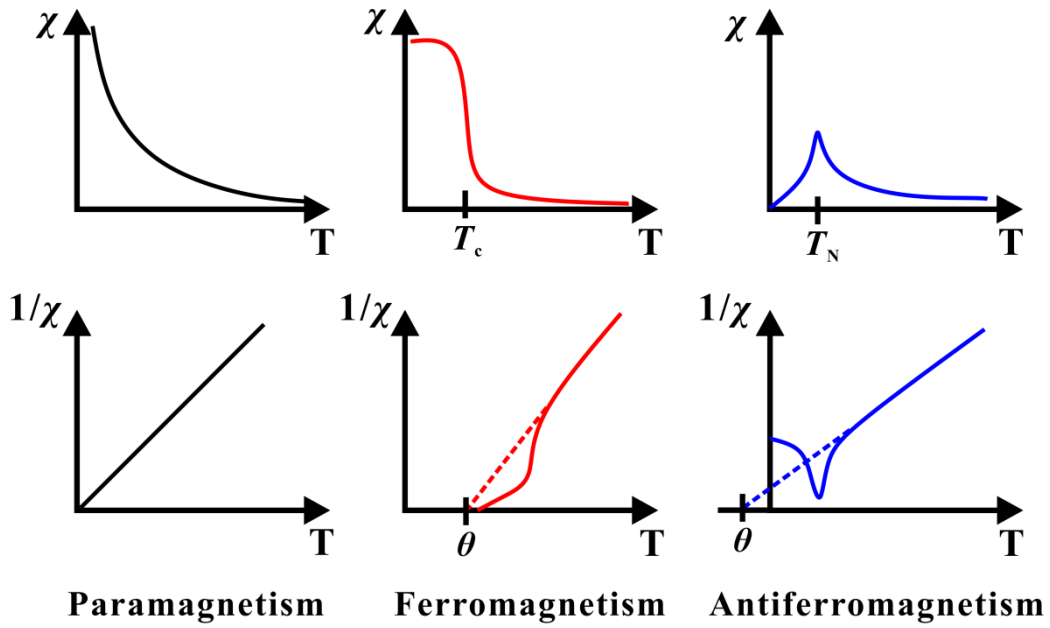

Figure 1.3 Magnetic susceptibility of a paramagnet, ferromagnet and antiferromagnet

Paramagnetism (indicated in black) contains randomly oriented magnetic moments. Upon magnetic ordering, subdivisions of this class include: ferromagnetism (indicated in red) with aligned moments that order in parallel at the Curie temperature (denoted by T_c) with a positive Weiss (θ) temperature; antiferromagnetism (indicated in blue) with aligned moments that order in antiparallel at the Néel temperature (denoted by T_N) with a negative Weiss (θ) temperature.

For ferromagnets, there is spontaneous magnetization at low temperatures that favours the alignment of magnetic moments along the field direction. Magnetic susceptibility decreases as temperature increases due to the increasing influence of thermal disorder over the interatomic exchange. The temperature at which interatomic electronic exchange forces are overcome by thermal disorder is known as the Curie temperature (T_c). Above T_c, the thermal energy randomizes the magnetic dipoles and the material behaves like a paramagnet. Ferromagnetism is the strongest class of magnetism

and it is the only class that can create forces powerful enough to be observable by the human eye.

The temperature at which antiferromagnetic interactions are invoked is known as the Néel temperature (T_N). Below T_N, the sublattices magnetize spontaneously and they couple in antiparallel fashion such that the net magnetization becomes nearly zero. The average magnetic susceptibility of a powdered sample is increased by 1/3 due to the difference in anisotropic susceptibilities, parallel and perpendicular to the direction of the external magnetic field. As temperature lowers, the magnetization parallel to the field direction decreases towards zero while the magnetization perpendicular to the field direction remains the same.

1.3.3 Hysteresis

One feature of ferromagnetic materials is the spontaneous magnetization that is often associated with hysteresis, which is a magnetic memory retained after the applied field is removed. It can be determined by a plot of magnetization as a function of external magnetic field depicted by a hysteresis loop (**Figure 1.4**). Initially, the ferromagnet is not magnetized with separate domains pointing in random directions, similar to the behaviour of a paramagnet. As an external field is applied, the domains begin to orient themselves and magnetize spontaneously until it reaches saturation magnetization, M_s. The magnetization that is retained after the removal of an external field is known as remanent magnetization, M_r, and the material will remain magnetized until a field is applied in the opposite direction. The field that is required to remove all magnetization from the material is known as a coercivity field, H_c. The coercivity and the broadness of the

hysteresis loop determines whether the material is a soft or hard magnet. An ideal soft magnet will contain no hysteresis, so the magnetization will be lost once the magnetic field is removed. However, due to multiple domains and domain walls, all soft magnets contain low remanence and coercivity, illustrated by narrow hysteresis loops. Applications of soft magnets include transformers and circuits where hysteresis must be kept at a minimum so that the material can be demagnetized easily to minimize energy loss. Hard magnetic materials are also known as permanent magnets because of their ability to retain magnetization. Applications include magnetic recording such as tapes and discs, refrigerator magnets and credit cards. Examples of this class of materials include RE_2Fe_{17}, $SmCo_5$, and $NdFe_{14}B$, the most powerful magnet known.

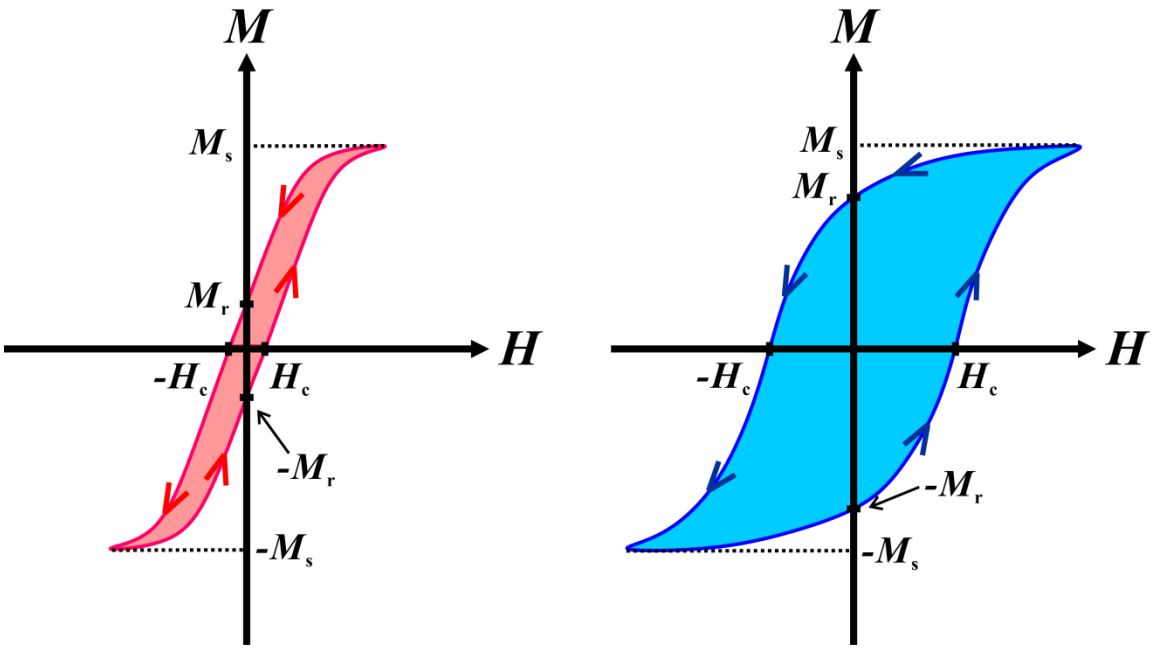

Figure 1.4 Hysteresis loop of a soft (left) and hard (right) ferromagnet.

1.4 Magnetocaloric effect

The magnetocaloric effect is the adiabatic temperature change (ΔT_{ad}) of a material as it undergoes external field applications. At constant pressure, the total entropy of a system must remain constant ($\Delta S = 0$) where an external field is applied adiabatically to the system. Besides the lattice, S_{Lat} and electronic S_{El} entropies involved, there will be an additional magnetic entropy component, S_{Mag}, that will contribute to the total entropy (Eq. 1.4.1). The coupling of the magnetic moments to the field will lower ΔS_{Mag}, which results in the increase of ΔS_{Lat} and ΔS_{El}. Therefore, the material heats up (**Figure 1.5, right side**). Conversely, the material can be cooled down by removing the field (**Figure 1.5, left side**).

$$S = S_{Mag} + S_{Lat} + S_{El} \tag{1.4.1}$$

The MCE was initially discovered in pure iron by Warburg in 1880 [1]. This effect is present in all paramagnetic materials with positive susceptibilities. However, the isothermal entropy change is the greatest in ferromagnetic materials around their Curie temperature because of the spontaneous magnetization introduced by the applied field. Hence, the maximum ΔS value will be reached at the Curie temperature, T_c, of the material.

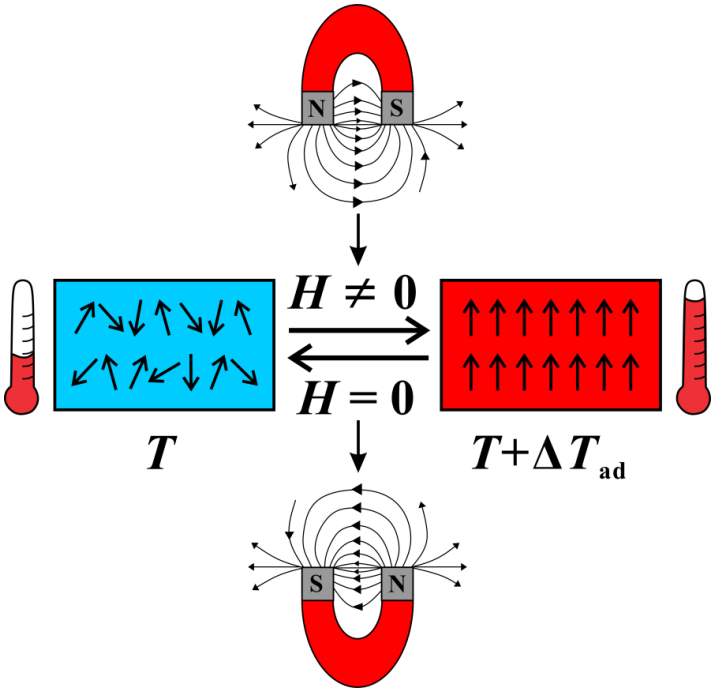

Figure 1.5 The magnetocaloric effect (MCE)

1.4.1 Magnetic entropy

The entropy of a system can be calculated using the Boltzmann equation (Eq. 1.4.2), where k_B is the boltzmann constant (1.3806053 x 10^{-23} J/K) and Ω is the number of possible states.

$$S = k_B \ln \Omega \tag{1.4.2}$$

For magnetic entropy, the number of states correspond to the number of possible magnetic states. Hence, Eq. 1.4.2 can be rewritten to Eq. 1.4.3, where N_A is Avogadro's number and J is the total magnetic quantum number.

$$S_{Mag} = N_A k_B ln\,(2J + 1) \tag{1.4.3}$$

For one mole of atom, the universal gas constant, R = 8.3144621 J/mol·K, can be used instead.

During adiabatic field application, if all the magnetic moments align in the field direction (ferromagnetic behaviour), there is only one possible orientation. Then, S_{mag} will be equal to zero (Eq. 1.4.4). The total magnetic entropy change, ΔS_{mag}, of the system, from paramagnetic to ferromagnetic, will be negative (Eq. 1.4.5).

$$S_{Mag} = Rln(1) = 0 \tag{1.4.4}$$

$$\Delta S_{Mag} = -Rln(2J + 1) \tag{1.4.5}$$

1.4.2 Thermodynamics of magnetocaloric effect

Under isobaric conditions, S, can be expressed as a function of temperature, and magnetic field, (T, H), depicted in **Figure 1.6** for a reversible process. The total entropy function, S, (black solid line), comprises of the S_{Mag} (blue dashed line) and (red dotted line). In general, the S_{Mag}, S_{Lat} and S_{El} increase as temperature increases. However, under constant field application ($H \neq 0$), the ΔS_{Mag} across two magnetic fields (H = 0 and $H \neq 0$) decreases as the material heats up.

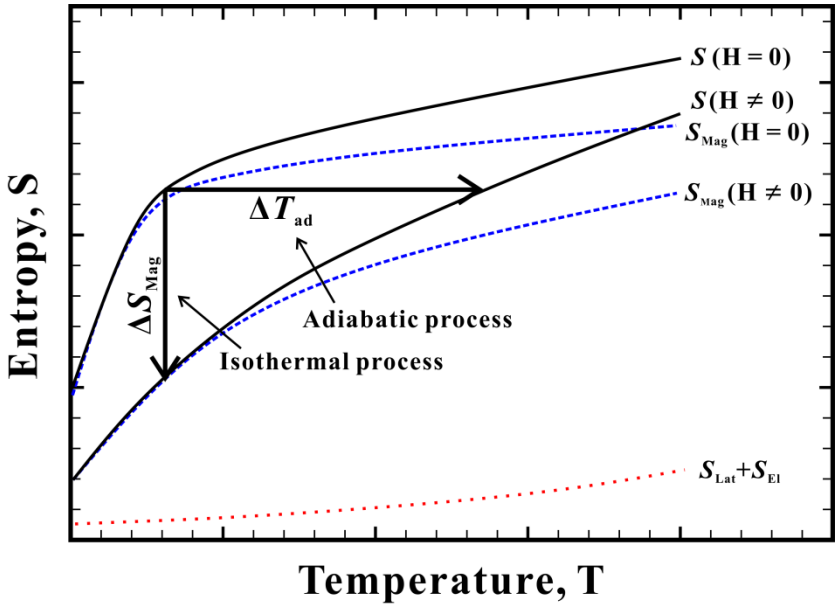

Figure 1.6 Entropy plotted as a function of temperature and applied field.
The figure is reproduced from [2].

For materials with a reversible second-order phase transition, the isothermal magnetic entropy, ΔS_{Mag}, and adiabatic temperature change, ΔT_{ad}, can be derived from the Maxwell relations. These quantities can be calculated by Eq. 1.4.6 and Eq. 1.4.7, respectively. The heat capacity, C_H, is temperature and field dependent.

$$(\Delta S_{Mag})_T = \int_{H_i}^{H_f} \left(\frac{\partial M}{\partial T}\right)_H dH \tag{1.4.6}$$

$$(\Delta T_{ad})_S = -\int_{H_i}^{H_f} \frac{T}{C_H} \left(\frac{\partial M}{\partial T}\right)_H dH \tag{1.4.7}$$

1.4.3 Magnetic refrigeration

Energy conservation has become a global effort in hopes of reducing the overall energy consumption and increasing energy efficiency. Possible solutions include replacing technologies that use conventional energy sources such as fossil fuels with clean, renewable ones and modifying existing processes to increase the overall energy efficiency.

Magnetic refrigeration is an alternative cooling technology, which is based on the magnetocaloric effect and it involves magnetization and demagnetization of a magnetic material. This refrigeration process can be viewed as analogous to the compression and expansion mechanisms used in conventional vapour cycle refrigeration (**Figure 1.7**). By using solid materials as refrigerants, the magnetic refrigeration eliminates the use of hazardous chemicals such as ozone depleting chloroflurocarbon (CFC), greenhouse hydrochlorofluorocarbon (HCFC) and hydrofluorocarbon (HFC) gases and hazardous ammonia (NH_3). Also, solid materials allow for more compact refrigeration systems that would generate less noise. A study done by Zimm *et al.* [3] has demonstrated that the cooling efficiency of room temperature magnetic refrigeration using Gd can be as high as 60% of the theoretical limit, compared to the 45% upper limit for conventional vapour-based methods, based on the Carnot cycle.

Although the magnetocaloric effect (MCE) was discovered in iron over a century ago, its application towards refrigeration was not demonstrated until more than 50 years later when Giauque and MacDougall used gadolinium sulphate as the refrigerant to reach

0.25 K [4]. Today, magnetic refrigeration remains a crucial process for applications in ultra-low cooling and gas liquefaction.

1.4.4 Mechanism of magnetic refrigeration

As mentioned, the magnetic refrigeration requires a solid material, preferably a ferromagnet as refrigerant, operating around its Curie temperature to achieve the highest MCE for certain applied field change. In magnetic refrigeration, an external field is applied adiabatically to the refrigerant, inducing alignment of the magnetic moments in the field direction, thereby decreasing S_{Mag} and increasing $S_{Lat} + S_{El}$. As a result of the positive ΔT_{ad}, a heat transfer fluid can be used to expel the heat out to the surroundings and bring the system back to its initial temperature. At this point, removing the external field from the refrigerant will cause the magnetic moments to disorient, which will increase S_{Mag} and decrease $S_{Lat} + S_{El}$. Consequently, the system cools down for refrigeration applications. The heat lost from the object being cooled is transferred to the system and the refrigeration cycle continues (**Figure 1.7, left**).

Ideally, there should be minimal hysteresis loss in the material so that the refrigerant can survive through repetitive cycles. However, materials that give large ΔS tend to have first-order magnetic transitions where the MCE process is irreversible. Although numerous studies have been performed on reducing hysteresis loss, either by Fe substitution [5] or size reduction of the material to nano-scale [6], no promising results have so far emerged.

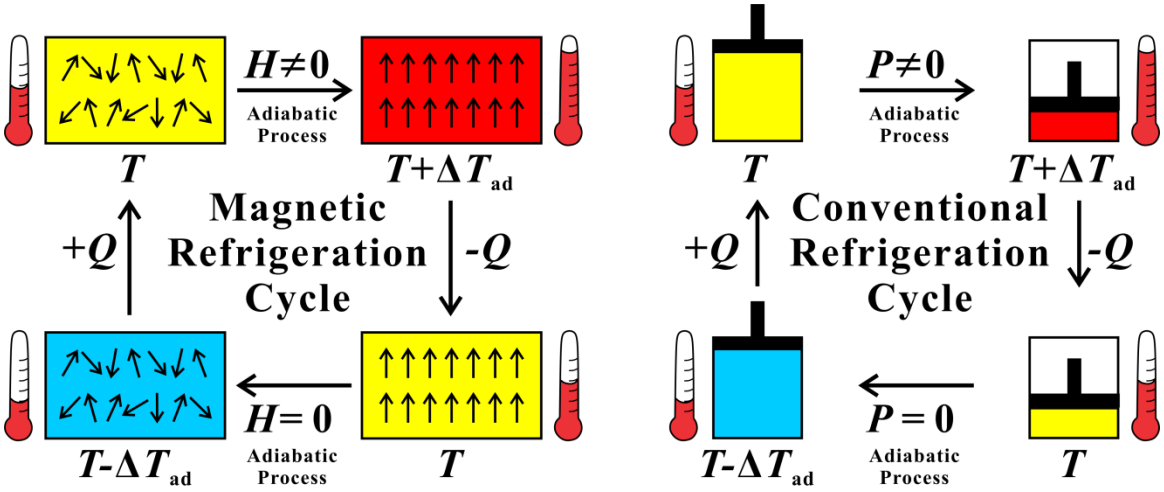

Figure 1.7 Magnetic and conventional refrigeration cycles

The magnetic refrigeration cycle (left) operates by using an adiabatic magnetic field to orient and disorient magnetic moments in a solid ferromagnetic refrigerant. This is analogous to the conventional refrigeration cycle (right), which uses external pressure to compress and decompress the gaseous refrigerant under adiabatic conditions.

1.4.5 Giant magnetocaloric effect and the RE_5T_4 phases

Aside from the large magnetic moment that lies in rare-earth elements, Gd has a near room temperature transition temperature (T_c = 294 K), which makes this element and its alloys ideal for potential room-temperature magnetic refrigeration. The discovery of giant magnetocaloric effect (hence large MCE) in $Gd_5Si_2Ge_2$ in 1997 [7] has motivated researchers to extensively explore the RE_5T_4 (*RE* = rare-earth element, *T* = *p*-elements) phases. The MCE discovered in $Gd_5Si_2Ge_2$ is greater than triple the value found in elemental Gd and it is called a giant MCE (GMCE).

Structurally, the interslab dimers of the monoclinic $Gd_5Si_2Ge_2$ ($P2_1/a$) structure are half intact and half broken. This structure can be seen as an intermediate between the

orthorhombic Gd_5Si_4 and Gd_5Ge_4 parent structures, where the interslab dimers are fully intact or broken. Upon application of magnetic field, the interslab dimers of the $Gd_5Si_2Ge_2$ become fully intact and its symmetry change from monoclinic to orthorhombic (*Pnma*), which results in the coupled magneto-structural transition, causing a GMCE.

In terms of the magnetic properties, the $Gd_5Si_2Ge_2$ and Gd_5Si_4 are ferromagnetic with magnetic ordering temperatures (T_c) 276 K [7] and 335 K [8]. The Gd_5Ge_4 phase is anti-ferromagnetic with T_N = 128 K. The near room temperature transition and large ΔT_{ad} make $Gd_5Si_2Ge_2$ a great potential candidate for magnetic refrigeration. Previous research has shown that the interslab dimers can be reformed or broken via partial substitution on the *p*-element site, which are governed by two main effects: the size and valence electron concentration (VEC) effects. In Gd_5Si_4, it was shown that a partial substitution of electron-richer P [9] or larger Sb [10] for Si can break the interslab dimers. Similarly, introduction of electron-poor Ga [11] or smaller Si [7] into Gd_5Ge_4 can reform the interslab dimers.

1.5 Magnetic susceptibility measurements

1.5.1 Superconducting QUantum Interference Device (SQUID)

As mentioned, determining the nature of a magnetic ordering in a material allows for a better understanding and optimization of its properties. The instrument used for all experiments in this thesis is the high sensitivity Superconducting QUantum Interference Device (SQUID) in the Magnetic Property Measurement System (MPMS) sample magnetometer. Depending on the power supply, there are the Direct Current (DC) and

Radio Frequency (RF) SQUIDs. Both types employ the Josephson junction, which is a thin insulating layer that separates the superconducting loop. In DC SQUID, a magnetic flux generates a current in a superconducting coil that contains two parallel Josephson junctions that destroy the superconductivity and a voltage reading can be taken. This is known as the DC Josephson effect. Alternatively, in less sensitive RF SQUID, there is only one Josephson junction and it is based on the AC Josephson effect. A fixed voltage difference is taken across the junction as a result of flux oscillations.

1.5.2 Experimental set-up and measurements

All the experiments are conducted using a RF SQUID cooled with liquid helium with a temperature range between 5 and 400 K. The measured sample can be in the form of a solid chunk or powder. For a solid sample, the sample is weighed, placed at a specific height of the rod free from other magnetic species with Apiezon grease and secured by teflon tape. For samples in powder form, the powders are embedded in a pre-weighed gelatin capsule and secured at the correct height in an empty straw with no other magnetic sensitive materials present. If the material has a high magnetic response (ferromagnetic material), only a small amount of sample (10 - 50 mg) is required. There are two measurement modes, which are DC and RSO (reciprocating sample option). Both modes are highly sensitive. The former passes the sample through the inductive coils in discrete steps and a number of pre-set times to obtains an average value. The latter rapidly oscillates the sample about the center of the coils. The saturation magnetization is higher in DC compared to the RSO mode. However, the RSO mode speeds up the measurement

while maintaining high sensitivity accuracy. Therefore, most measurements are done in the RSO mode.

A field-cooled measurement done in this thesis is usually performed with an applied field of 100 Oe to determine a magnetic transition temperature and the magnetic nature of the material. A field-dependent isothermal measurement can be conducted in the field range $0 \leq H \leq 5$ T at low temperatures to determine the true magnetic nature of the specimen and around the transition temperature to determine the magnetocaloric effect if the material is ferromagnetic in nature. If the transition temperature of the investigated material lies above 350 K, an oven attachment is usually required, which allows for magnetic measurements to run from room temperature until 650 K.

Chapter 2: X-ray Diffraction

2.1 Introduction of X-ray diffraction

The year 2012 marks the centennial discovery of the X-ray diffraction (XRD) technique, in which the concept of using X-rays to study crystalline materials was developed. Today, tremendous amounts of research has been done using this technique to investigate the structure and composition of materials. The wavelength range of X-rays ($0.1 \leq \lambda \leq 100$ Å) makes them suitable to study materials with atomic resolution. For solid state materials, the atomic structure of a studied specimen as well as its short and long range structural environments involved can be explored. The determination of elemental and structural compositions and their relationships to physical properties allow further design of new and improved materials. The subjects studied with this technique can range widely from crystals in solids to proteins in biological systems. For the purpose of this thesis study, all the crystal structures explored are solid and metallic with potential magnetic applications.

2.2 Characteristic X-ray spectra

The typical laboratory X-ray source involves an X-ray tube, where characteristic X-rays are generated from the collision of high-energy electrons with a metal target. The wavelength, λ, of X-rays is typically on the order of angstroms since diffraction can only be observed when λ and the interatomic distances are within the same magnitude range. The λ is strongly dependent on the metal source and usually transition metals such as Cu,

Cr, Fe, Co and Mo, etc are being used. The specimen being studied can be in either powder or single crystalline form.

A high voltage (typically around 40 kV) is applied to accelerate the electrons against the metal target, these electrons decelerate gradually by making multiple collisions with electrons from the metal atoms. This is known as white radiation, which is the most intense at short wavelengths and gradually decreases in intensity at longer wavelengths. This form of radiation is dependent on the amount of voltage applied, with higher voltage resulting in a more intense "hump" at lower wavelengths (**Figure 2.1, left**).

When the electrons reach a threshold potential, some of the metal electrons can be removed from their atomic orbitals. A vacancy is created at the innermost shell (K) where electrons from the next higher shell (L) or the one above that (M) can descend to fill the K shell. This results in a decrease in potential energy and appears in the form of radiation that can be identified by characteristic $K_{\alpha 1}$, $K_{\alpha 2}$ ($L \rightarrow K$) and K_{β} ($M \rightarrow K$) intensity peaks. The $K_{\alpha 1}$ and $K_{\alpha 2}$ correspond to $2p_{3/2} \rightarrow 1s$ and $2p_{1/2} \rightarrow 1s$, respectively. The intensity ratio of the $K_{\alpha 1}$:$K_{\alpha 2}$ doublet is approximately 2:1 and the intensity of the K_{β} peak is much lower than that of the $K_{\alpha 1,2}$ peaks (**Figure 2.1, right**). Generally, as the atomic number (Z) of a metal target increases, the characteristic peaks shift to lower wavelengths due to an energy increase.

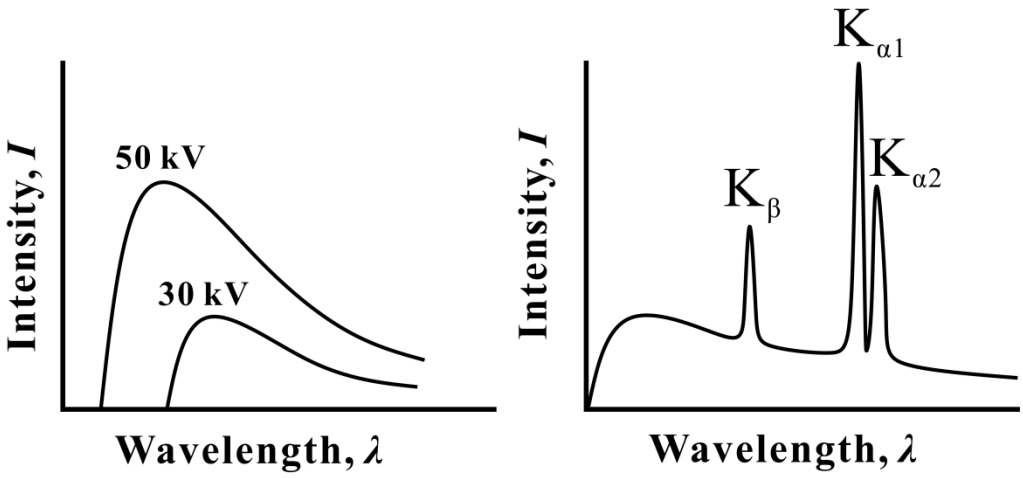

Figure 2.1 (left) Intensity as a function of wavelength with varied applied voltages. (right) The characteristic X-ray spectra of a typical element consisting of K_α and K_β radiations.

2.3 Interplanar distance and miller indices

A crystal structure can be characterized by a set of periodically arranged atoms and a lattice that contains arrays of atoms exhibiting long range order in three dimensions. The smallest repeated volume of the lattice is known as an unit cell. It can be represented by the unit cell vectors, which are three independent vectors in the $\vec{a}$, $\vec{b}$ and $\vec{c}$ directions. The angles connecting these vectors are denoted by α, β and γ. A unit cell may be categorized by one of the seven Bravais lattice systems, which are triclinic, monoclinic, orthorhombic, tetragonal, hexagonal, trigonal and cubic. These systems are categorized based on unit cell vector and angle conditions.

Within crystals, there are sets of crystallographic planes that intersect all lattice points. Each set of planes are equally spaced, parallel to one another and are represented by integer (*h*,*k*,*l*) indices known as Miller indices. The *h*, *k* and *l* values correspond to the number of times a unit cell is cut in the *a*, *b* and *c* directions, respectively. The distance

between each set of planes is known as the interplanar distance, d_{hkl}. Assuming that α = β = γ = 90°, the interplanar distance, lattice parameters and Miller indices are related by Eq. 2.3.1.

$$\frac{1}{d_{hkl}} = \sqrt{\frac{h^2}{a^2} + \frac{k^2}{b^2} + \frac{l^2}{c^2}} \tag{2.3.1}$$

2.4 Bragg's Law

The principles of X-ray diffraction can be explained using the Bragg's Law (**Figure 2.2**), where λ is the wavelength of X-rays, d_{hkl} is the interplanar spacing and θ is the incident beam angle also known as the Bragg angle. If the atoms lie on lattice planes where a set of incident X-rays hit the plane at the Bragg angle, the reflected rays will diffract off the plane with the same angle across all directions assuming that the scattering is elastic. If two parallel waves propagate in-phase, this is known as constructive interference and the amplitudes are doubled. Conversely, if the two parallel waves are completely out-of-phase, the resultant wave has no amplitude and this is known as destructive interference. A diffracted beam with maximum intensity will only occur when the diffracted X-rays are in phase. Therefore, this law states that the X-rays scattered from a crystalline solid must have constructive interference in order to produce a diffracted beam. The mathematical equation (Eq. 2.4.1) representing this law is known as the Bragg's Law.

$$n\lambda = 2dsin\theta \tag{2.4.1}$$

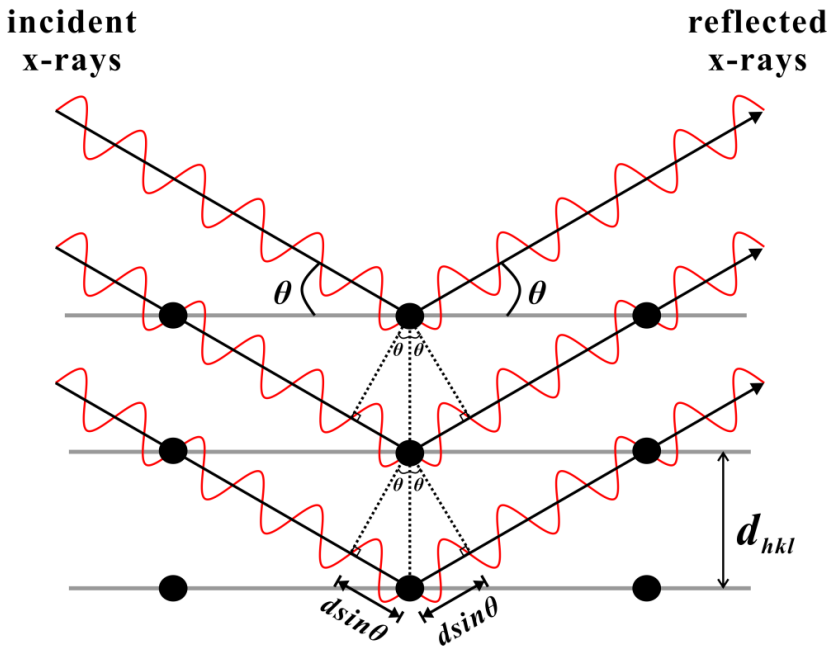

Figure 2.2 A visual representation of the Bragg's law. The black dots correspond to atoms that sit on crystallographic planes with interplanar distance, d_{hkl}.

2.5 Reciprocal lattice and Ewald's sphere

The detector used in X-ray experiments can measure the intensities of the diffracted beams and these beams can be mapped onto a reciprocal lattice in the reciprocal space. An asterisk (*) symbol is added behind each vector to indicate that it is a reciprocal vector. The relationships between the lattice in the direct and reciprocal space can be expressed mathematically by Eq. 2.5.1, 2.5.2 and 2.5.3.

$$a = \frac{b^* \text{ x } c^*}{V^*}, b = \frac{c^* \text{ x } a^*}{V^*}, c = \frac{a^* \text{ x } b^*}{V^*} \tag{2.5.1}$$

$$a^* = \frac{b \text{ x } c}{V}, b^* = \frac{c \text{ x } a}{V}, c^* = \frac{a \text{ x } b}{V} \tag{2.5.2}$$

$$\vec{a} \cdot \vec{a}^* = 1, \ \vec{b} \cdot b^* = 1, \ \vec{c} \cdot c^* = 1 \tag{2.5.3}$$

Based on the above two equations, it can be shown that the interplanar d_{hkl} spacing in the real (d_{hkl}) and reciprocal space (d_{hkl}^{*}) is inversely related (Eq. 2.5.4).

$$d_{hkl}^{*} = \frac{1}{d_{hkl}} \tag{2.5.4}$$

The main differences between the real unit cell and the reciprocal unit cell are that atoms are situated in the unit cell and these atoms may be found anywhere in the unit cell as long as the symmetry requirements are satisfied, whereas in the reciprocal unit cell, there are only diffracted lattice peaks denoted by the Miller indices.

The concepts of reciprocal lattice and Ewald's sphere can be used to visually understand diffraction from the reciprocal space in three-dimensions. Ewald imagined that the radius of the sphere is equal to the incident vector $\vec{k}_0$ or an inverse of the X-ray wavelength, $1/\lambda$. According to Bragg's law, the angle between k_0 and the reflected vector k_1 must equal to 2θ. Hence, by using the cosine law in trigonometry, it can be seen that the distance between the origin and each individual lattice point must equal to d_{hkl}^{*} or $1/d_{hkl}$. Only the lattice points with the reciprocal lattice vectors $\vec{d}_{hkl}^{*}$ that coincide with the surface of the Ewald's sphere will diffract (**Figure 2.3**). Since the radius of the Ewald's sphere equals to $1/\lambda$, diffraction data collected with higher energy radiation (smaller λ) will allow for a larger sphere coverage and higher resolution data.

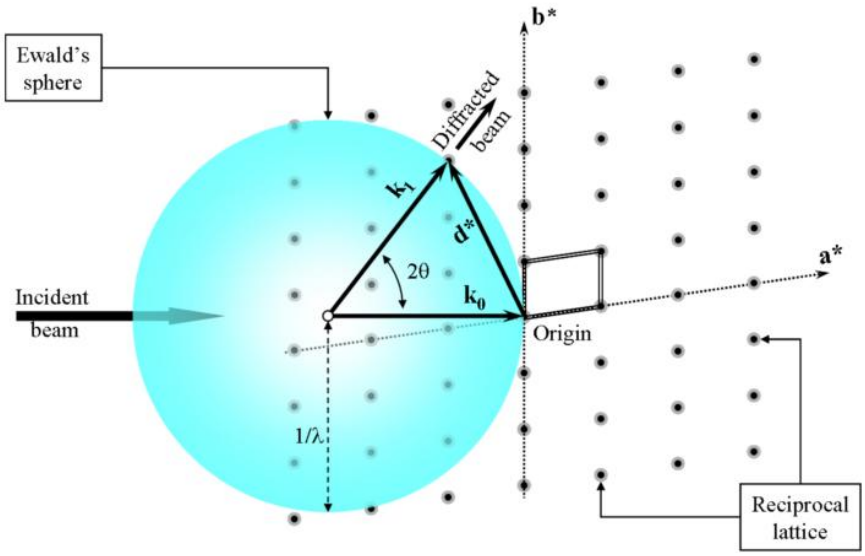

Figure 2.3 Visual representation of the relationship between the Ewald's sphere and the reciprocal lattice.

The image is reproduced from Pecharsky & Zavalij [12].

2.6 Structure Factor

In an unit cell that consists solely of one atom, the diffracted intensity will depend on the scattering ability of the atom (number of electrons in the element). However, when the unit cell contains multiple atoms, the combined intensities are proportional to the structure factor, $|F_{hkl}|^2$ (Eq. 2.6.1), the square value of the structure amplitude, F_{hkl} (Eq. 2.6.2). F_{hkl} is a function of the total number of atoms, n, and the atomic scattering factor, $f_{j,2\theta}$, for the j^{th} atom, and the exponent function is the scalar production between the Miller indices (h,k,l) and the (x,y,z) position of the j^{th} atom in the unit cell. The atomic scattering factor, $f_{j,2\theta}$, is a function that is strongly dependent on the thermal vibration and scattering

power of the atom at particular θ and λ. The high thermal motion causes the atomic displacement parameter or temperature factor to increase, which reduces the scattering power of the atom. As a result, the diffracted intensity decrease significantly as a function of sinθ/λ.

$$I \propto |F_{hkl}|^2 \tag{2.6.1}$$

$$F_{hkl} = \sum_{j=1}^{n} f_j e^{2\pi i(hx_j + ky_j + lz_j)} \tag{2.6.2}$$

Using Euler's rule, Eq. 2.6.2 can be expanded into the sum of cosines and sines, which represent the real and imaginary components, respectively (Eq. 2.6.3).

$$F_{hkl} = \sum_{j=1}^{n} f_j \cos\left[2\pi\left(hx_j + ky_j + lz_j\right)\right] + i\sum_{j=1}^{n} f_j \sin\left[2\pi\left(hx_j + ky_j + lz_j\right)\right] \tag{2.6.3}$$

If the real (*x*-axis) and the imaginary (*y*-axis) components of the structure amplitude is illustrated graphically, the angle between the structure amplitude and the real component is known as a phase angle, α. In a centrosymmetric structure, for every atom with coordinate position (*x*,*y*,*z*), there is an equivalent atom at position (-*x*,-*y*,-*z*). In the reciprocal lattice, the two centrosymmetric lattice points (*h*,*k*,*l*) and (-*h*,-*k*,-*l*), known as a Friedel pair, are equivalent. Therefore, Eq. 2.6.4 holds true. This translates to the existence of the phase angle α only in the real component where α is either in phase (α = 0°) or out of phase (α = 180°). In a non-centrosymmetric structure, Eq. 2.6.4 no longer holds, so the scattering factor will contain contributions from the imaginary component.

$$\cos(\alpha) = \cos(-\alpha), \sin(-\alpha) = -\sin(\alpha) \tag{2.6.4}$$

During an X-ray diffraction experiment, the incident X-rays penetrate the material of interest where the intensities of the diffracted peaks are recorded by the instrument detector and mapped as lattice points in three-dimensions in the reciprocal space. The phase angle, including its sign, is not measured directly in the experiment, so any of its information have to be determined afterwards. More information in regards to solving the phase angle will be discussed later.

2.7 Fourier Transform

The structure of a material is determined by scattering X-rays from the sample of interest, mapping the lattice peaks in the reciprocal space and transforming the collected intensities from reciprocal space to atoms in real space to solve the structure. The latter is known as a Fourier transformation. It can be represented by a mathematical expression (Eq. 2.7.1), which relates the atoms and the lattice peaks in the direct and reciprocal spaces, respectively.

$$\rho_{xyz} = \frac{1}{V} \sum_{h=-\infty}^{h=+\infty} \sum_{k=-\infty}^{k=+\infty} \sum_{l=-\infty}^{l=+\infty} F_{hkl}\, exp[-2\pi i(hx + ky + lz)] \qquad (2.7.1)$$

In Eq. 2.7.1, ρ_{xyz} is the electron density, V is the volume of unit cell in real space and $\vec{F}_{hkl}$ is the structure amplitude.

After determining the phase angle, α, for every $|\vec{F}^{obs}{}_{hkl}|$, a Fourier map can be constructed. The Fourier map contains electron density distributions of atoms in an unit cell.

2.8 Powder X-ray diffraction

2.8.1 Origin of the powder diffraction pattern and Ewald's sphere

Powder X-ray diffraction in a polycrystalline sample involves many crystallites that are randomly oriented. Cones of diffraction with different intensities and diameters that touch the surface of the Ewald's sphere are produced. The apex of all the cones touch the center of the Ewald's sphere and the rings that form at the base of the cones where an area detector is placed perpendicularly to the incident wave vector $\vec{k}_0$ is known as Debye rings. Each Debye ring is a 2-D representation of the intensities at particular (*h*, *k*, *l*). However, the instrument used for this thesis integrates the intensities of all the diffracted cones into a 1-D representation X-ray powder pattern with varying 2θ. It works by integrating the scattered intensities at the circumference of the equatorial plane of the Ewald's sphere (**Figure 2.4**).

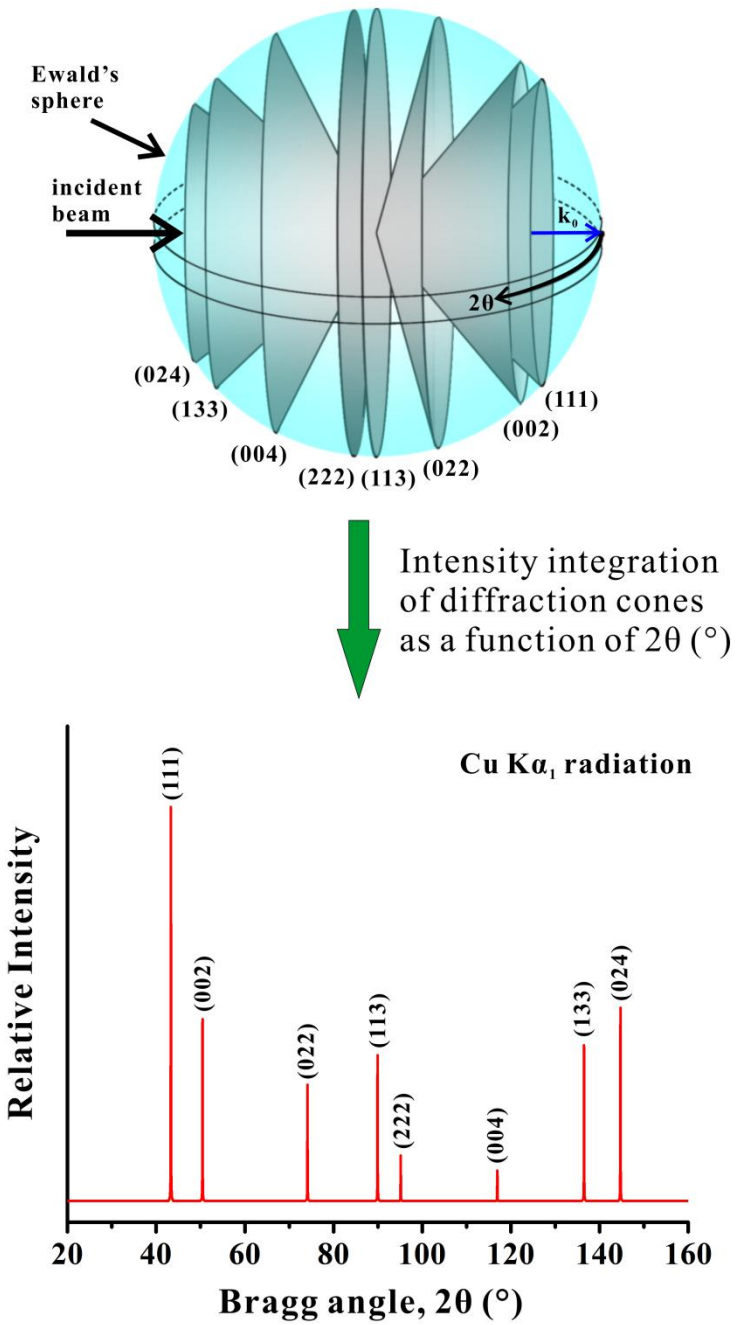

Figure 2.4 Cones of diffraction with corresponding Miller indices intersecting Ewald's sphere.

This image is reproduced from Pecharsky & Zavalij [12].

2.8.2 Sample preparation and experimental set-up

Preliminary phase identification and quantification can be done using X-ray powder diffraction. Small amounts of sample is grinded finely with a motar and pestle before depositing it evenly on a vaseline coated silicon disk. This preparation method allows the powder to be mounted quickly. Each sample is then placed in a sample holder and collected on a PANalytical X'Pert Pro diffractometer with a linear X'Celerator detector and monochromated Cu $K\alpha$ ($K_{\alpha 1}$ = 1.540598 Å) radiation at room temperature. To increase sample grain randomness and reduce preferred orientation, the sample holder is spinned about the normal to the sample surface for the entire measurement. For the samples containing high Gd and Fe contents, the resolution of the data are often poor due to the fluorescence associated with the Cu source. Hence, a Co $K\alpha$ ($K\alpha_{1+2}$ = 1.789010 Å) radiation is used instead. The diffracted beams collected at various 2θ are then read by the detector.

2.8.3 Rietveld refinement

A Rietveld refinement uses a least-squares minimization technique that refines a theoretical profile against a measured profile. The software used for this thesis is the FullProf Suite that can allow refinement of multiple phases [13]. The Rietveld refinement allows for a full profile analysis, which takes all the instrumental and experimental parameters into consideration. No internal standard is required for this type of analysis. However, structural information of all the present phases have to be identified prior to the refinement. In addition to fitting the background and structural profiles, the characterization of the peak shape must not be ignored. The peak shape function used for

the refinement is the normalized Pseudo-Voigt, which is a linear combination of Lorentzian and Gaussian peak function at the Full Width at Half Maximum (FWHM). This function is directly related to the half-width parameters *U, V* and *W* that characterize the instrumental resolution of the profile.

The goal of the refinement is to try to overlap the intensities of the experimental model with a calculated profile. The outcome of the refinement is given in the form of Profile (R_p, Eq. 2.8.1), Weighted Profile (R_{wp}, Eq. 2.8.2) and Expected Weighted Profile (R_{exp}, Eq. 2.8.3) agreement factors . The y_i is the intensity of the profile, w_i is the weight of the observed intensity, n is the number of data points and p is the number of refined parameters. The reduced Chi square, χ^2 (Eq. 2.8.4) should be minimized to obtain a good refinement.

$$R_p = 100 \frac{\sum_i |y_i(obs) - y_i(cal)|}{\sum_i y_i} \tag{2.8.1}$$

$$R_{wp} = 100 \left[\frac{\sum_i w_i |y_i(obs) - y_i(cal)|^2}{\sum_i w_i [y_i(cal)]^2} \right]^{1/2} \tag{2.8.2}$$

$$R_{exp} = 100 \left[\frac{n-p}{\sum_i w_i [y_i(cal)]^2} \right]^{1/2} \tag{2.8.3}$$

$$\chi^2 = \left[\frac{R_{wp}}{R_{exp}} \right]^2 \tag{2.8.4}$$

2.9 Single crystal X-ray diffraction

2.9.1 Experimental set-up and measurements

For single crystal X-ray diffraction experiments, a crystal with size dimensions of 0.1 - 0.5 mm, is mounted on a glass capillary using epoxy glue and collected on a STOE IPDS II diffractometer with an image plate detector and a Mo $K\alpha$ radiation in the whole reciprocal sphere [14]. This type of area detector allows the X-ray photons to be captured by phosphors which are first stored as an image and then scanned by a laser. The combination of multiple frames allow the construction of diffraction peaks in the reciprocal sphere.

Once the collection of intensities of a crystal in reciprocal space has finished, a reciprocal lattice can be extracted and by crystallographic relationships, the unit cell can be determined. The structural refinement can be done using the SHELX-97 software [15]. This program enables solving and refining of a crystal structure.

The two approaches that are generally used to solve structures are the Patterson and Direct method techniques. The Patterson technique assumes electron density to exist only at positions where there are atoms. It requires building interatomic vectors between atoms and mapping them to a common point, usually the origin of a unit cell. This method favors the determination of the positions of heavy atoms since heavy atoms scatter X-rays better. The Direct Method approach determines the phase angle by using a triplet of reflections.

Similar to the powder refinement, a single crystal refinement uses the least-squares method, which tries to minimize the difference between the observed and calculated intensities. There are certain parameters that are required for the refinement, which are the weighing scheme that corrects for intensity differences between different reflections, the atomic coordinates, the correct number and type of elements, the atomic occupancies, elements mixing in the appropriate site, the anisotropic temperature parameters and the extinction coefficient for out-of-phase reflection.

Chapter 3: $Gd_4Ge_{3-x}Pn_x$ (*Pn* = P, Sb, Bi, *x* = 0.5 - 3): stabilizing the non-existing Gd_4Ge_3 binary through valence electron concentration. Electronic and magnetic properties of $Gd_4Ge_{3-x}Pn_x$

This chapter contains the manuscript "$Gd_4Ge_{3-x}Pn_x$ (*Pn* = P, Sb, Bi, *x* = 0.5 - 3): Stabilizing the Nonexisting Gd_4Ge_3 Binary through Valence Electron Concentration. Electronic and Magnetic Properties of $Gd_4Ge_{3-x}Pn_x$" by Yan Yin Janice Cheung, Volodymyr Svitlyk and Yurij Mozharivskyj. Reproduced with permission from Inorganic Chemistry, in press. Unpublished work copyright 2012 American Chemical Society (*Inorg. Chem.*, DOI: 10.1021/ic300817j).

3.1 Abstract

The $Gd_4Ge_{3-x}Pn_x$ (*Pn* = P, Sb, Bi; *x* = 0.5 - 3) phases have been prepared and characterized using X-ray diffraction, wavelength dispersive spectroscopy and magnetization measurements. All $Gd_4Ge_{3-x}Pn_x$ phases adopt a cubic anti-Th_3P_4 structure and no deficiency on the Gd or *p*-element site could be detected. Only one P-containing phase with the $Gd_4Ge_{2.51(5)}P_{0.49(5)}$ composition could be obtained, as larger substitution levels did not yield the phase. Existence of $Gd_4Ge_{2.51(5)}P_{0.49(5)}$ and $Gd_4Ge_{2.49(3)}Bi_{0.51(3)}$ suggests that the hypothetical Gd_4Ge_3 binary can be easily stabilized by a small increase in the valence electron count, and that the size of the *p*-element is not a key factor. Electronic structure calculations reveal that large substitution levels with electron-richer

Sb and Bi are possible for charge-balanced $(Gd^{3+})_4(Ge^{4-})_3$ as extra electrons occupy the bonding Gd-Gd and Gd-Ge states. This analysis also supports stability of Gd_4Sb_3 and Gd_4Bi_3. All $Gd_4Ge_{3-x}Pn_x$ phases order ferromagnetically with relatively high Curie temperatures of 234 K to 356 K. The variation in the Curie temperatures of the $Gd_4Ge_{3-x}Sb_x$ and $Gd_4Ge_{3-x}Bi_x$ series can be explained through the changes in the numbers of conduction electrons associated with the Ge/Sb(Bi) substitution.

3.2 Introduction

The rare-earth binary and pseudo-binary phases of group 14 and 15 elements, as well as their derivatives, gained a lot of attention [16–21] since the discovery of giant magnetocaloric effect (GMCE) in pseudobinary $Gd_5Si_{4-x}Ge_x$ phases [7,22–24]. One of the important outcomes of such research fury is the possibility of tuning the structural and magnetic properties of the RE_5X_4 phases (*RE* is a rare earth, *X* is a *p*-element) through valence electron concentration [9–11,19,25,26]. For example, a decrease in the valence electron count in Gd_5Ge_4 through the Ga substitution leads to the formation of the interslab dimers and temperature-induced structural transitions concomitant with a giant magnetocaloric effect in $Gd_5Ge_{4-x}Ga_x$ [11,26]. For the most part, the research in this area appears to focus primarily on the RE_5X_4 phases with little attention given to other binary phases or their derivatives. While such preoccupation with one type of materials is fully understood, the rare-earth and group 14 and 15 elements offer a variety of other binary phases with different magnetic properties [27]. However, the structure and properties of such phases appear to be less systematically studied, and in general the factors governing their stability are not as well understood.

If we were to limit our attention to the rare-earth rich side of the binary diagrams, we could see an interesting trend regarding existence of the RE_5X_3 (Mn_5Si_3 structure), RE_4X_3 (anti-Th_3P_4 structure) and RE_5X_4 (Sm_5Ge_4, Gd_5Si_4, or Zr_5Si_4 structures) phases (*RE* is a rare earth, *X* is Si, Ge, Sn, Sb, Bi). With the exception of Ce_3Si_2, $(La/Ce/Pr)_4Ge_3$, La_3Sb_2 and few other binaries, the general trend is that RE_5X_3 and RE_5X_4 phases exist for tetralides and RE_5X_3 and RE_4X_3 ones for pnictides. Thus, while the RE_5X_3 phases are stable both for tetralides and pnictides, the RE_5X_4 and RE_4X_3 ones exist either with tetralides or pnictides, respectively. The size factor does not appear to play a role, as exchanging Sb for size-similar Sn yields RE_4Sb_3 instead of RE_5Sn_4 for most of the rare-earth elements. Then we may assume that a valence electron concentration (VEC) is likely to dictate the stability of the RE_5X_4 and RE_4X_3 phases. If this is the case, can we stabilize the RE_4X_3 phases for tetralides through an increase in the VEC and what are the magnetic properties of such phases? As there are 17 rare-earth elements and different combinations of group 14 and 15 elements, the play field is obviously rich. Chizhov *et al.* were the first to test this hypothesis by exploring the $Ce_4(P_{1-x}Si_x)_{3-z}$ series through the substitution on the non-metal site [28]. Indeed, the anti-Th_3P_4 structure could be stabilized for the Ce pseudobinary through the P substitution and an associated increase in the VEC. The authors estimated that an excess of 1.4 - 3.1 e^- per f.u. is required for this structure to exist.

In our study, we explored this idea further and focused on the Gd-containing phases. In this paper, we report on successful stabilization of hypothetical Gd_4Ge_3 via a VEC increase achieved through substitution of Ge with electron-richer pnictogens, P, Sb

and Bi. To emphasize stabilization of "Gd_4Ge_3", we use the $Gd_4Ge_{3-x}Pn_x$ formula instead of $Gd_4Pn_{3-x}Ge_x$, as relatively small substitution levels of x = 0.5 in $Gd_4Ge_{3-x}Pn_x$ yield the anti-Th_3P_4 structure. We also present magnetic properties of the newly discovered $Gd_4Ge_{3-x}Pn_x$ phases and discuss their changes with respect to the size and valence electron concentration.

3.3 Experimental

3.3.1. Synthesis and X-ray analysis

Synthesis of the $Gd_4Ge_{3-x}P_x$ (x = 0.5, 1, 1.5) samples was a three-step process. First, equimolar amounts of Gd (99.99 wt%, distilled grade, Metall Rare Earth Limited, China) and Ge (99.9999%, Alfa Aesar) pieces were arc-melted. The binary was then grinded into powder in an Ar filled drybox and mixed with P (99.999 wt%, Puratronic, Alfa Aesar) powder to produce 1:1 molar ratio of the GdGe:P precursor. The resultant powder was pressed, sealed in an evacuated silica tube and heated as described in [29]. The product was checked by powder X-ray diffraction before combining it with the elemental Gd and Ge powders to yield the desired $Gd_4Ge_{3-x}P_x$ compositions. Powders with the total mass of ~ 1 g were pressed and arc-melted at least 3 times to achieve homogeneity. No significant losses were observed. A part of the ingot from each sample was wrapped in a separated Ta foil, sealed in an evacuated silica tube and annealed at 1173 K for 2 weeks. The ampoules were then quenched in cold water.

Samples with the $Gd_4Ge_{3-x}Sb_x$ and $Gd_4Ge_{3-x}Bi_x$ (x = 0.5 - 3) compositions were prepared with a x = 0.5 increment by arc-melting ~1 g of stoichiometric elemental Gd, Ge

and Sb (99.999 wt%, CERAC Inc.) or Bi (99.998wt%, Alfa Aesar) pieces and then by re-melting them at least 3 times to ensure homogeneity. Excess of Sb or Bi (1-10 wt%, larger excess for the Sb- and Bi-richer samples) was loaded to compensate for their losses during the arc-melting, which resulted in less than 3 wt% total losses for all the samples. The cast samples were wrapped in individual Ta foils, sealed in silica ampoules and annealed at 1273 K for at least one month to improve crystallinity and homogeneity. The ampoules were then quenched in cold water.

Room-temperature phase analyses of the polycrystalline samples were performed on a PANalytical X'Pert Pro diffractometer with a linear X'Celerator detector using a Co K_α radiation in the 2θ range from 20 to 90°. The lattice parameters were refined using the FullProf software [13]. All the samples adopt the cubic anti-Th_3P_4-type structure with space group *I*-43*d*. The Gd and *Pn* atoms sit on the 16*c* (*x*, *x*, *x*) and 12*a* (0, 0.25, 0.375) sites, respectively. The refined powder pattern for the Gd_4Bi_3 sample is shown in **Supporting Information, Figure S3.1**. The lattice parameter of 9.38756(2) Å and atomic coordinate x = 0.0721(1) for the Gd atoms were extracted. These values agree well with literature ones [21,30,31]. Single crystals extracted from the $Gd_4Ge_{2.5}P_{0.5}$, $Gd_4Ge_{3-x}Sb_x$ (x = 1, 1.5, 2, 2.5, 3) and $Gd_4Ge_{3-x}Bi_x$ (x = 0.5, 1, 1.5, 2) samples were analyzed on a STOE IPDS II diffractometer with the MoK_α radiation [14]. No crystals suitable for the X-ray analysis could be picked up from the $Gd_4Ge_{3-x}Bi_x$ samples with x = 2.5 and 3. The structures were solved and refined using the *SHELXS* and *SHELXL* software packages, respectively [15]. All the crystals adopt the cubic anti-Th_3P_4 type structure with the *I*-43*d* space group. The Gd and Ge/*Pn* atoms occupy the 16*c* and 12*a* sites, respectively.

Refinement of the Ge/*Pn* occupancies proceeded well due to the significant differences in the atomic scattering factors between Ge and P, Sb, or Bi. The crystallographic data and refinement details for the $Gd_4Ge_{2.5}P_{0.5}$, $Gd_4Ge_{2.5}Bi_{0.5}$ and Gd_4Ge_2Sb single crystals are summarized in **Table 3.1** and **Table 3.2**, and those for other crystals are provided in the **Supporting Information, Tables S3.1 - S3.4**. Further details of the crystal structure investigated are available from the Fachinformationszentrum Karlsruhe, 76344 Eggenstein-Leopoldshafen, Germany, on quoting the depository number CSD–424230 for $Gd_4Ge_{2.51}P_{0.49}$, 424231 for $Gd_4Ge_{2.49}Bi_{0.51}$, 424232 for $Gd_4Ge_{1.97}Sb_{1.03}$ and 424233-39 for the ones listed in **Supporting Information Tables S4.1 and S4.2**.

Table 3.1 Crystallographic data and refinement results for the $Gd_4Ge_{2.51(5)}P_{0.49(5)}$, $Gd_4Ge_{2.49(3)}Bi_{0.51(3)}$ and $Gd_4Ge_{1.97(4)}Sb_{1.03(4)}$ single crystals.

Loaded composition	$Gd_4Ge_{2.5}P_{0.5}$	$Gd_4Ge_{2.5}Bi_{0.5}$	Gd_4Ge_2Sb
Refined composition	$Gd_4Ge_{2.51(5)}P_{0.49(5)}$	$Gd_4Ge_{2.49(3)}Bi_{0.51(3)}$	$Gd_4Ge_{1.97(4)}Sb_{1.03(4)}$
Space group	*I*-43*d*	*I*-43*d*	*I*-43*d*
Lattice parameters *a*, Å	8.8348(6)	8.9799(9)	9.0111(5)
Volume, Å^3	689.59(8)	724.1(1)	731.70(7)
Crystal size, mm^3	0.028 x 0.047 x 0.047	0.013 x 0.054 x 0.113	0.016 x 0.045 x 0.103
2θ range for data collection, °	11.3 – 58.16	11.12 – 58.40	11.08 – 58.18
Index ranges	$-12 \le h \le 9$, $-12 \le k \le 12$, $-12 \le l \le 12$	$-12 \le h \le 12$, $-10 \le k \le 12$, $-12 \le l \le 11$	$-11 \le h \le 12$, $-10 \le k \le 12$, $-12 \le l \le 12$

Reflections collected	3312	3723	3804
Independent reflections	161 [R(int) = 0.0454]	169 [R(int) = 0.1559]	176 [R(int) = 0.0540]
Completeness to max 2θ (%)	100.0	99.0	100.0
Data/restraints/ parameters	161 / 0 / 8	169 / 0 / 9	172 / 0 / 9
Goodness-of-fit on F^2	1.110	1.142	1.255
Final R indices [I > 2σ(I)]	R_1 = 0.0224, wR_2 = 0.0468	R_1 = 0.0281, wR_2 = 0.0458	R_1 = 0.0161, wR_2 = 0.0212
R indices (all data)	R_1 = 0.0272, wR_2 = 0.0483	R_1 = 0.0435, wR_2 = 0.0481	R_1 = 0.0221, wR_2 = 0.0218
Extinction coefficient	0.0008(2)	0.00027(17)	0.00006(4)
Largest diff. peak and hole (e/Å $^{-3}$)	0.800 and -0.801	1.526 and -1.244	0.574 and -0.668

Table 3.2 Atomic and isotropic temperature parameters (U, Å ^{2}) for the $Gd_4Ge_{2.51(5)}P_{0.49(5)}$, $Gd_4Ge_{2.49(3)}Bi_{0.51(3)}$ and $Gd_4Ge_{1.97(4)}Sb_{1.03(4)}$ single crystals

Atom	**Site**	**Occupancy**	***x/a***	***y/b***	***z/c***	***U***
			$Gd_4Ge_{2.51(5)}P_{0.49(5)}$			
Gd	16*c*	1	0.0660(1)	0.0660(1)	0.0660(1)	0.012(1)
Ge/P	12*a*	0.84(2)/0.16 (2)	0	¼	3/8	0.012(1)
			$Gd_4Ge_{2.49(3)}Bi_{0.51(3)}$			

Gd	16*c*	1	0.0667(1)	0.0667(1)	0.0667(1)	0.020(1)
Ge/Bi	12*a*	0.831/0.169(9)	0	¼	3/8	0.016(1)
			$Gd_4Ge_{1.97(4)}Sb_{1.03(4)}$			
Gd	16*c*	1	0.0680(1)	0.0680(1)	0.0680(1)	0.015(1)
Ge/Sb	12*a*	0.66/0.34(1)	0	¼	3/8	0.010(1)

The lattice parameters *vs*. the refined *Pn* amounts obtained from the single crystal X-ray diffraction are plotted in **Figure 3.1**. For the $Gd_4Ge_{2.5}Bi_{0.5}$ and Gd_4Bi_3 samples, the lattice parameters derived from the powder data were plotted and the loading composition of $Gd_4Ge_{2.5}Bi_{0.5}$ was used in the graph. For the Bi series, no standard deviation in the composition was included for $Gd_4Ge_{0.5}Bi_{2.5}$ because the Ge/Bi occupancy could not be reliably determined from the Rietveld refinement.

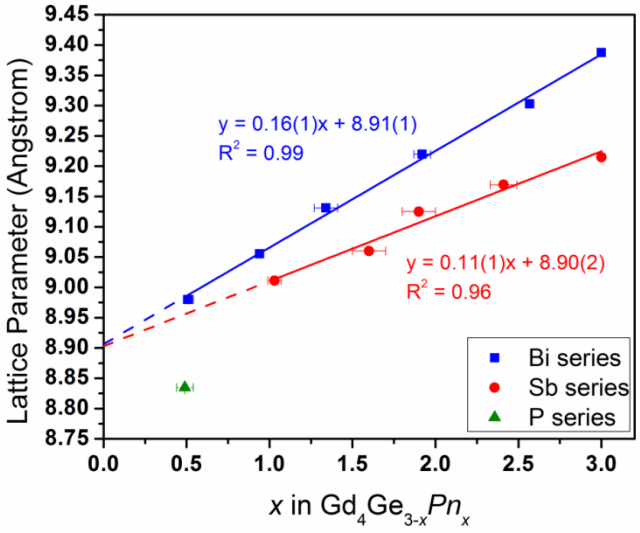

Figure 3.1 Lattice parameters vs. *Pn* amount in $Gd_4Ge_{3-x}Pn_x$ (*Pn* = P, Sb, Bi; x = 0.5 - 3). The symbols with the error bars represent compositions obtained from the single crystal refinements. For x = 0.5 and 1 in the Bi series, the error bars are too small to be observed.

3.3.2 Quantitative elemental analysis

Elemental compositions of the $Gd_4Ge_{3-x}Sb_x$ (x = 1 - 2.5) and $Gd_4Ge_{3-x}Bi_x$ (x = 0.5 - 2.5) samples were examined through the wavelength dispersive spectroscopy (WDS) on a JEOL 8900 electron probe micro-analyzer (EPMA). Due to the overlap between the Gd Lα and Ge Lα lines, only the *Pn* (*Pn* = Sb, Bi) compositions could be accurately determined. The Ge compositions were estimated assuming that Ge and *Pn* atoms fully occupied the 12*a* sites and the Gd atoms fully occupied the 16*c* site. To verify validity of the EPMA results, additional elemental analysis on the $Gd_4Ge_{3-x}Sb_x$ (x = 1 - 2.5) series was performed using a Resonetics M-50-Lr 193 nm Excimer laser abalation system coupled to an Agilent 7700x quadrupole ICP-MS with a 32 microns spot size. Pure

Gd_5Ge_4 and Gd_4Sb_3 binaries were used as internal standards. The results are listed in **Table 3.3**.

Table 3.3 Compositions based on the EPMA, LA-ICP-MS and the X-ray single crystal analyses.

For the EPMA results, the Ge compositions are estimated using the *Pn* concentrations.

***Pn* = Sb**			
Loading	**EPMA**	**LA-ICP-MS**	**X-ray**
$Gd_4Ge_{2.5}Pn_{0.5}$	N/A	N/A	N/A
Gd_4Ge_2Pn	$Gd_4Ge_{1.9(1)}Sb_{1.1(1)}$	$Gd_{4.0(2)}Ge_{2.04(5)}Sb_{1.00(2)}$	$Gd_4Ge_{1.97(4)}Sb_{1.03(4)}$
$Gd_4Ge_{1.5}Pn_{1.5}$	$Gd_4Ge_{1.6(2)}Sb_{1.4(2)}$	$Gd_{4.0(2)}Ge_{1.49(3)}Sb_{1.47(3)}$	$Gd_4Ge_{1.4(1)}Sb_{1.6(1)}$
Gd_4GePn_2	$Gd_4Ge_{0.93(6)}Sb_{2.07(6)}$	$Gd_{4.0(2)}Ge_{1.01(2)}Sb_{2.02(4)}$	$Gd_4Ge_{1.1(1)}Sb_{1.9(1)}$
$Gd_4Ge_{0.5}Pn_{2.5}$	$Gd_4Ge_{0.59(4)}Sb_{2.41(4)}$	$Gd_{4.0(2)}Ge_{0.48(1)}Sb_{2.58(5)}$	$Gd_4Ge_{0.59(8)}Sb_{2.41(8)}$

***Pn* = Bi**		
Loading	**EPMA**	**X-ray**
$Gd_4Ge_{2.5}Pn_{0.5}$	$Gd_4Ge_{2.46(8)}Bi_{0.54(8)}$	$Gd_4Ge_{2.49(3)}Bi_{0.51(3)}$
Gd_4Ge_2Pn	$Gd_4Ge_{1.95(2)}Bi_{1.05(2)}$	$Gd_4Ge_{2.07(2)}Bi_{0.93(2)}$
$Gd_4Ge_{1.5}Pn_{1.5}$	$Gd_4Ge_{1.48(4)}Bi_{1.52(4)}$	$Gd_4Ge_{1.66(7)}Bi_{1.34(7)}$
Gd_4GePn_2	$Gd_4Ge_{1.1(1)}Bi_{1.9(1)}$	$Gd_4Ge_{1.08(5)}Bi_{1.92(5)}$
$Gd_4Ge_{0.5}Pn_{2.5}$	$Gd_4Ge_{0.88(4)}Bi_{2.12(4)}$	N/A

3.3.3 Band structure calculations

Tight-binding, linear-muffin-tin-orbital (TB-LMTO) electronic structure calculations were performed with the Stuttgart program [32] for the Gd_4Sb_3, Gd_4Bi_3, hypothetical "Gd_4Ge_3" and Gd_5Ge_4 binary phases using the atomic sphere approximation (ASA) [33]. As mentioned, the former three binaries adopt the cubic anti-Th_3P_4-type structure. The atomic coordinates for Gd range from x = 0.0660 - 0.0721 and the

Ge/Sb/Bi atoms are fixed on the 12*a* (0, 0.25, 0.375) site, respectively. The lattice parameters and atomic coordinates for the Gd_4Sb_3 and Gd_4Bi_3 structures were extracted from the single crystal and powder X-ray refinements, respectively. For "Gd_4Ge_3", the lattice parameter a = 8.89 Å was extrapolated from the single crystal X-ray data of $Gd_4Ge_{3-x}Pn_x$ (*Pn* = P, Sb, Bi) (**Figure 3.1**). The atomic coordinates for Gd (0.0660, 0.0660, 0.0660), were estimated based on the single crystal refinement data of $Gd_4Ge_{3-x}Pn_x$ (*Pn* = P, Bi; x = 0.5). For orthorhombic Gd_5Ge_4 (*Pnma*), the lattice parameters and atomic coordinates were taken from Yao, J. *et al.* [34]. Local density approximation (LDA) [35] was used to treat exchange and correlation interactions. Space-filling empty spheres were introduced into the Wigner-Seitz (WS) cell to achieve convergence during the calculation. The radii for the WS cell were generated automatically and the radii used for $Gd_4(Ge/Sb/Bi)_3$ were: Gd = 3.35 - 3.42 Å, Ge = 2.94 Å, Sb = 3.21 Å and Bi = 3.30 Å. The basis set included 6*s* and 5*d* orbitals for Gd, n*s* and n*p* orbitals for Ge/Sb/Bi (n = 4, 5 and 6). Two empty spheres (E) with WS radii of 1.43 - 2.11 Å were included in each binary for the calculation. The orbitals were treated using the Löwdin downfolding technique [32,33]. The first Brillouin zone for the reciprocal space integration included 512 irreducible *k* points. The Gd 4*f* orbitals were treated as core ones that do not participate in bonding. The orbital interactions were analyzed via partial density of states (PDOS) and the crystal orbital Hamilton population (COHP) calculations using the tetrahedron method [36]. For the COHP calculations, the maximum distance considered between two Gd atoms was 4.21 Å.

3.3.4 Magnetic measurements

Magnetic measurements were performed for polycrystalline $Gd_4Ge_{3-x}Pn_x$ samples (*Pn* = P, *x* = 0.5; *Pn* = Sb, *x* = 1, 1.5, 2, 2.5, 3; *Pn* = Bi, *x* = 0.5, 1, 1.5, 2, 2.5, 3) with a 100 Oe external field in a field-cooled (FC) mode from 5 to 400 K with 2 to 5 K increments on a Quantum Design Superconducting Quantum Interference Device (SQUID) instrument. The magnetization (M) vs. temperature (T) data are shown in **Figure 3.2**.

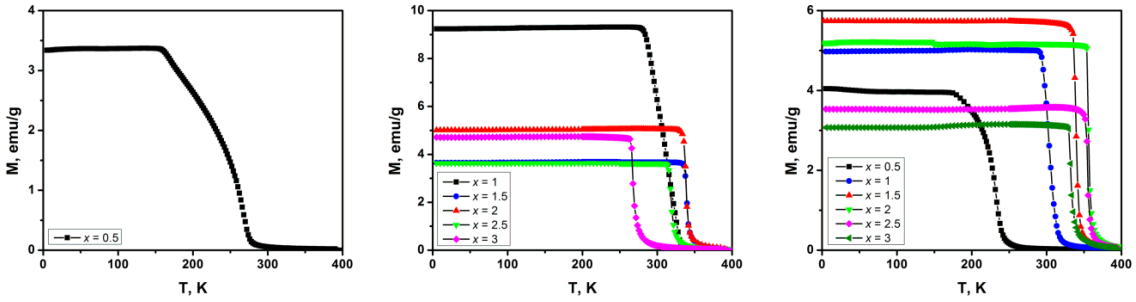

Figure 3.2 Magnetization vs. temperature plots for $Gd_4Ge_{2.5}P_{0.5}$ (left), $Gd_4Ge_{3-x}Sb_x$ (*x* = 1 - 3) (center) and $Gd_4Ge_{3-x}Bi_x$ (*x* = 0.5 - 3) (right).

3.4 Results and Discussion

3.4.1 Composition and stability of $Gd_4Ge_{3-x}Pn_x$.

From the powder X-ray analysis, the pre-reacted GdGe:P precursor was confirmed to contain the GdP binary and elemental Ge. The formation of the stable GdP binary prior to arc-melting the $Gd_4Ge_{3-x}P_x$ (*x* = 0.5 - 1.5) samples is essential for minimizing P losses and allowing the formation of desired phases. The cubic anti-Th_3P_4 phase was present in all cast samples but its amount decreased for larger P amounts and after annealing (**Supporting Information Table S3.5**). Interestingly, annealing the *x* = 0.5 sample at 900°C increased the amount of the $Gd_4Ge_{3-x}P_x$ phase and led to the decomposition of

Gd_5Ge_4 found in the cast sample. But this had a minimal effect on the presence of the Gd_5Ge_3 impurity. This observation suggests that P stabilizes the "Gd_4Ge_3" and not Gd_5Ge_4 phase. The P amount does not appear to extend beyond $x = 0.49(5)$ (based on the single crystal results) since annealing of the $x = 1$ and 1.5 samples either reduced the amount of the desired phase or eliminated it completely. One may question whether P is really present in the $Gd_4Ge_{3-x}P_x$ phase. First of all, the pure Gd_4Ge_3 phase does not exist. Secondly, the lattice parameter (8.8348(6) Å) of $Gd_4Ge_{2.51}P_{0.49}$ is smaller than those extrapolated from the $Gd_4Ge_{3-x}Sb_x$ and $Gd_4Ge_{3-x}Bi_x$ series for the hypothetical Gd_4Ge_3 binary (8.90(2) and 8.91(1) Å, **Figure 3.1**). Therefore, $Gd_4Ge_{2.51}P_{0.49}$ exists and it is stabilized through the P substitution.

As for the $Gd_4Ge_{3-x}Sb_x$ ($x = 0.5$ - 3) series, the anti-Th_3P_4 structure was observed in the cast and annealed samples with $1 \leq x \leq 3$. Based on the refinement results, the $x = 0.5$ sample contained exclusively the Gd_5Ge_3 and Gd_5Ge_4 phases and further annealing promoted formation of the GdGe and Sb impurities. In the $Gd_4Ge_{3-x}Bi_x$ ($x = 0.5$ - 3) series, the anti-Th_3P_4 structure was observed in all cast and annealed samples. Based on the single crystal refinements and powder analysis, the homogeneity regions for $Gd_4Ge_{3-x}Sb_x$ extend from $x = 1.03(4)$ till 3 and for $Gd_4Ge_{3-x}Bi_x$ from $x = 0.51(3)$ till 3. Using the lattice parameters for $Gd_4Ge_{3-x}Sb_x$ and $Gd_4Ge_{3-x}Bi_x$, one can extrapolate the lattice parameters for hypothetical Gd_4Ge_3, which are 8.90(2) and 8.91(1) Å, respectively. It is worth mentioning that a small substitution level of Bi ($x = 0.51(3)$), similar to the P substitution, is sufficient to stabilize the anti-Th_3P_4 structure. Formation of the Sb-and Bi-rich $Gd_4Ge_{3-x}Pn_x$ phases is not surprising, as the Gd_4Sb_3 and Gd_4Bi_3 binaries are stable, so these mixed

phases can be seen as Ge-substituted binaries. However, for small Sb and Bi amounts such as $0.5 \leq x \leq 1$, the composition resemblance to Gd_4Sb_3 and Gd_4Bi_3 is lost. In fact, the Ge-rich $Gd_4Ge_{3-x}Sb_x$ and $Gd_4Ge_{3-x}Bi_x$ should be better treated as derivatives of hypothetical "Gd_4Ge_3". This argument applies even better to $Gd_4Ge_{2.51}P_{0.49}$, as Gd_4P_3 and P-rich $Gd_4Ge_{3-x}P_x$ phases do not exist and thus any P present can be seen as substitution for Ge in "Gd_4Ge_3".

One issue that we have to address is possible deficiencies on the 12*a* site in $Gd_4Ge_{3-x}Pn_x$. The studies on $Ce_4(P_{1-x}Si_x)_{3-z}$ indicated that the 12*a* site may be deficient up to $z = 0.34(3)$ but no correlation with either the P or Si amount could be established [28]. In our case, only the Sb/Bi concentration could be reliably established form the EPMA analysis, so the Ge amount was calculated assuming a full occupancy of the 12*a* site (**Table 3.3**). While the EPMA compositions can be used only as a guide, they suggest that the Sb/Bi amounts are within three standard deviations from the loading ones except for the $Gd_4Ge_{0.5}Bi_{2.5}$ sample. The additional LA-ICP-MS analysis conducted on the $Gd_4Ge_{3-x}Sb_x$ series confirmed that there are no deficiencies present in the system. These EPMA and LA-ICP-MS results are supported by the X-ray single crystal ones, which also yielded compositions close to the loading ones (**Table 3.3**) and did not indicate deficiencies on the 12*a* site. Based on the above analyses, we suggest that the 12*a* site is fully populated and if the deficiencies are present, they are likely to be small.

The anti-Th_3P_4 crystal structure consists of two distinct atomic positions. The Gd atom sits in a distorted octahedral environment surrounded by six Ge/*Pn* atoms and each *p*-element is surrounded by eight Gd neighbours. The atomic distances between the Gd

and corresponding *Pn* (*Pn* = Sb, Bi, Ge) element are listed in **Table 3.4**. Since no experimental data is available for Gd_4Ge_3, no standard deviations are given for the calculated distances. As there are no short Ge/*Pn*-Ge/*Pn* bonds in the structure, we can treat the Ge/*Pn* atoms as anions that draw electrons from the Gd atoms. Following the Zintl-Klemm formalism for valence compounds [37–39], we can write an electronic formula for $Gd_4Ge_{3-x}Pn_x$ as $(Gd^{3+})_4(Ge^{4-})_{3-x}(Pn^{3-})_x(xe^-)$. Thus, an introduction of *Pn* provides an excess of electrons and appears to stabilize the structure, considering that Gd_4Ge_3 does not exist. On the other hand, the atomic size is unlikely to be a factor, as the same structure is observed for $Gd_4Ge_{2.5}P_{0.5}$ and $Gd_4Ge_{2.5}Bi_{0.5}$, while the atomic sizes of P (r_{cov} = 1.10 Å) and Bi (r_{cov} = 1.53 Å) differ significantly from each other and from that of Ge (r_{cov} = 1.22 Å) [40]. Importance of extra electrons for the stability of the anti-Th_3P_4 structure is also supported by the anion deficiency in $La_4Ge_{2.67}$ [41] and existence of $Ce_4(P_{1-x}Si_x)_{3-z}$ [28].

Table 3.4 Experimental distances for Gd_4Sb_3, Gd_4Bi_3 and calculated ones for Gd_4Ge_3.

Atom 1	**Atom 2**	**C.N.**	**Distances**		
			Sb	Bi	Ge
Gd	*Pn*	3x	3.0807(4)	3.1381(9)	2.9174
	Pn	3x	3.3042(4)	3.3664(9)	3.2505
	Gd	3x	3.5374(6)	3.6040(3)	3.4756
	Gd	2x	3.9902(5)	4.065(1)	3.8495
	Gd	6x	4.4109(6)	4.493(1)	4.1920

Pn	Gd	4x	3.0807(4)	3.1381(9)	2.9174
	Gd	4x	3.3042(4)	3.3664(9)	3.2505
	Pn	8x	4.3099(2)	4.3906(1)	4.1579

3.4.2 Electronic structure

Using the Zintl-Klemm formalism, we can predict that the hypothetical Gd_4Ge_3 phase should be charge balanced, $(Gd^{3+})_4(Ge^{4-})_3$, and that the valence band, consisting of the Ge states, should be occupied, while the conduction band, made up of the Gd states, should be empty. The Fermi level should reside in a gap (or pseudogap) between the bands. This simple reasoning is supported by the TB-LMTO-ASA calculations. The density of states (DOS) and crystal orbital Hamilton population (COHP) for hypothetical Gd_4Ge_3 are presented in **Figure 3.3, center**. Indeed, the conduction band is dominated by Ge states, while the valence bands by Gd states, and the two are separated by a pseudogap, which corresponds to 24 e^-/f.u. or the Gd_4Ge_3 composition. However, some additional features became also apparent. First, the valence band has a substantial contribution from the Gd states, indicative of the significant hybridization between the Gd and Ge orbitals. Second, there are strong bonding Gd-Gd and Gd-Ge interactions in the conduction band (Ge-Ge interactions are negligible as $d_{Ge\text{-}Ge} > 4$ Å). These observations suggest that the ionic picture employed for the electron count is too simplistic and that Gd-Gd interactions cannot be ignored. The fact that the interactions above the Fermi level are strongly bonding explains why a *Pn* substitution is possible for hypothetical Gd_4Ge_3 and why electron-rich Gd_4Sb_3 and Gd_4Bi_3 are stable. The electronic structures of Gd_4Sb_3 and

Gd_4Bi_3 are quite similar and only that of Gd_4Sb_3 is given in **Figure 3.3, left**. (For Gd_4Bi_3, please refer to **Figure S3.2** in the **Supporting Information**.) There is a strong resemblance between the electronic structures of Gd_4Sb_3 and Gd_4Ge_3, but due to the higher electron count the Fermi level for Gd_4Sb_3 resides up in the conduction band.

Finally, we want to address potential reasons of why Gd_4Ge_3 does not exist, but the compositionally-close Gd_5Ge_4 phase does. We will limit our analysis to the bonding in the two phases. The electronic structure of Gd_5Ge_4 is shown in **Figure 3.3, right**. When compared to "Gd_4Ge_3", Gd_5Ge_4 displays stronger bonding Gd-Gd and Gd-Ge interactions around the Fermi level. While such interactions are also bonding in the vicinity of the Fermi level for "Gd_4Ge_3", they have no contribution at the Fermi level itself due to the presence of a pseudogap. Therefore, we may speculate that optimization of the Gd-Gd and Gd-Ge interactions is likely a key factor dictating stability of Gd_5Ge_4. We may also argue that a VEC increase above $31e^-$/f.u. is not favorable for Gd_5Ge_4, as there are interslab Ge-Ge (Ge_2) dimers in this phase and interactions within them are antibonding around the Fermi level [11]. Likely, destabilization of these dimers is the reason why Gd_5Sb_4 and Gd_5Bi_4 with $35e^-$/f.u. do not exist.

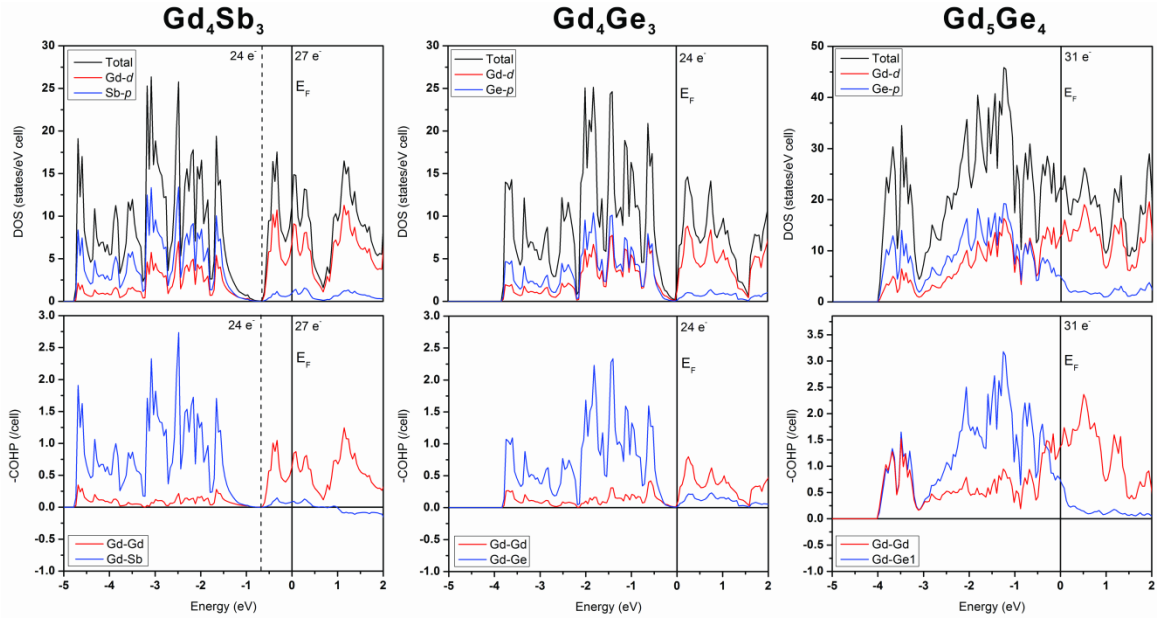

Figure 3.3 Density of States (DOS) and Crystal Orbital Hamilton Population (COHP) for Gd_4Sb_3 (left), Gd_4Ge_3 (center) and Gd_5Ge_4 (right).

3.4.3 Magnetic properties of $Gd_4Ge_{3-x}Pn_x$

All the $Gd_4Ge_{3-x}Pn_x$ (*Pn* = P, Sb, Bi) samples are ferromagnetic with transitions temperatures (T_C) ranging from 234 K to 356 K. (**Table 3.5**) The effective magnetic moments (μ_B) and Weiss temperatures could not be calculated because of the small number of data points in the paramagnetic regimes. The anti-ferromagnetic impurities, Gd_5Ge_3 (T_N = 76 K) [42] and GdP (T_N = 16 K) [43], were not observed on the magnetization curve of $Gd_4Ge_{2.5}P_{0.5}$, which is due to their low magnetic contributions to the total magnetization. For the samples with x = 0.5, presence of a heavier element resulted in a lower ordering temperature: T_C dropped from 270 K for $Gd_4Ge_{2.5}P_{0.5}$ to 234 K for $Gd_4Ge_{2.5}Bi_{0.5}$. This corresponds well with the results obtained by Hulliger *et al.* for the La series, in which the T_C values decrease as bigger anions are introduced: T_C (La_4As_3)

> T_C (La_4Sb_3) > T_C (La_4Bi_3) [44]. However, these results contradict the ones from the $Gd_4Sb_{3-x}Bi_x$ series, where the T_C values increase upon the Bi substitution [21]. Currently, we do not understand this trend for the $Gd_4Ge_{2.5}P_{0.5}$ and $Gd_4Ge_{2.5}Bi_{0.5}$ samples.

Table 3.5 Curie temperatures (T_C, K) of $Gd_4Ge_{3-x}Pn_x$ (*Pn* = P, Sb, Bi; x = 0.5 - 3)

x	$Gd_4Ge_{3-x}P_x$	$Gd_4Ge_{3-x}Sb_x$	$Gd_4Ge_{3-x}Bi_x$
0.5	270	N/A	234
1	N/A	316	302
1.5	N/A	340	340
2	N/A	340	356
2.5	N/A	320	356
3	N/A	268	334

Curie temperature as a function of the *Pn* concentration for the $Gd_4Ge_{3-x}Sb_x$ and $Gd_4Ge_{3-x}Bi_x$ series is plotted in **Figure 3.4**. The T_C values display an interesting parabolic behavior which to our knowledge was not observed for the RE_4Pn_3 phases before. According to the Ruderman-Kittel-Kasuya-Yosida (*RKKY*) theory [45–47], such peculiar tendency may result from changes in the valence electron concentration and variations in the Gd-Gd distances, both of which are controlled by substitution levels of the *p*-element. Most likely, a rise in the T_C values for small x values can be attributed to an increase in the number of conduction electrons (higher density of states) as the Fermi level moves from the pseudogap in "Gd_4Ge_3" into the conduction band in $Gd_4Ge_{3-x}Pn_x$ (see band structure of Gd_4Sb_3 in **Figure 3.3**). Also, the atomic sizes may play a role in this concentration region, as an increase in the T_C values for $Gd_4Ge_{3-x}Bi_x$ is steeper than that

for $Gd_4Ge_{3-x}Sb_x$. As x increases further, the Fermi level reaches the maximum in the DOS for both series (at ca. –0.33 and –0.29 eV for Gd_4Sb_3 and Gd_4Bi_3), which corresponds to ca. 25.5 e^-/f.u. or the $Gd_4Ge_{1.5}Pn_{1.5}$ composition (*Pn* = Sb, Bi). This agrees reasonably well with the high T_C values observed for $Gd_4Ge_{1.5}Sb_{1.5}$ and Gd_4GeSb_2. However, the maximum Curie temperatures for the Bi series is shifted to higher x = 2 and 2.5, which may be due to the inadequacy of the rigid band model used for these arguments or due to the fact that experimental and calculated DOSs are somewhat different. As x increases further, the DOS diminishes and this explains lower T_C values for the Sb- and Bi-rich phases. Again, the size of the *p*-element appears to be important as the $Gd_4Ge_{3-x}Bi_x$ series have a smaller decline in the T_C values.

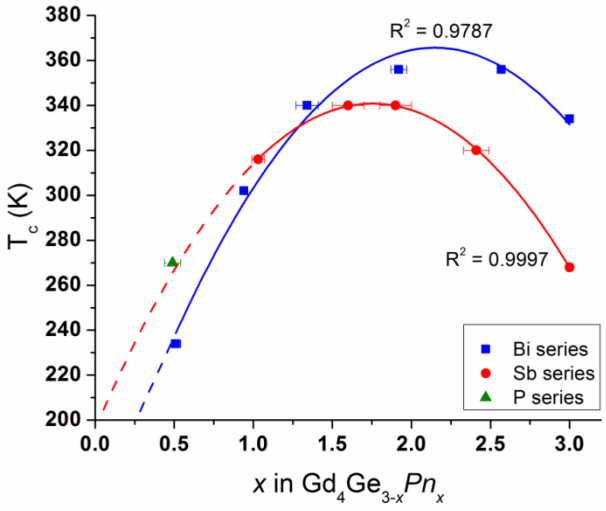

Figure 3.4 Curie temperatures (T_C) as a function of the *Pn* amount for $Gd_4Ge_{3-x}Pn_x$ (*Pn*: P, Sb, Bi; x = 0 - 3).

The symbols with the error bars represent compositions obtained from the single crystal refinements. For x = 0.5 and 1 in the Bi series, the error bars are too small to be observed.

3.5 Conclusions

While the "Gd_4Ge_3" binary does not exist, it can be easily stabilized by an increase in the valence electron count (VEC) achieved through the substitution of electron-richer P, Sb or Bi for Ge. Even a relatively small increase of 0.5 e^- in the VEC is sufficient to stabilize the $Gd_4Ge_{2.5}P_{0.5}$ and $Gd_4Ge_{2.5}Bi_{0.5}$ pseudobinary phases with the anti-Th_3P_4 structure. Larger substitution levels up to the end members are possible for the $Gd_4Ge_{3-x}Sb_x$ and $Gd_4Sb_{3-x}Bi_x$ series. Electronic structure analysis reveals that extra electrons in excess of 24 e^-/f.u., corresponding to the charge-balanced $(Gd^{3+})_4(Ge^{4-})_3$ formula, populate the bonding Gd-Gd and Gd-Ge interactions and thus stabilize the anti-Th_3P_4 structure. A likely reason for the non-existence of pure "Gd_4Ge_3" is presence of the compositionally-close Gd_5Ge_4 phase with strong Gd-Gd and Gd-Ge interactions around the Fermi level.

All $Gd_4Ge_{3-x}Pn_x$ (*Pn* = P, Sb, Bi; x = 0.5 - 3) phases order ferromagnetically with relatively high Curie temperatures (T_C = 234 - 356 K). A parabolic behavior in the T_C values for the $Gd_4Ge_{3-x}Sb_x$ and $Gd_4Sb_{3-x}Bi_x$ series is mostly due to the changes in the numbers of conduction electrons, associated with the Ge/Sb(Bi) substitution.

3.6 Supporting Information

Table S3.1. Crystallographic data and refinement results for the $Gd_4Ge_{3-x}Sb_x$ (x = 1.5, 2, 2.5 and 3) single crystals

Loaded composition	**Refined composition**	**Space group**	**Lattice parameters *a*, Å**	**Volume, Å^3**	**Crystal size, mm^3**	**2*θ* range for data collection, °**
$Gd_4Ge_{1.5}Sb_{1.5}$	$Gd_4Ge_{1.4(1)}Sb_{1.6(1)}$	*I*-43*d*	9.060(1)	743.6(1)	0.017 x 0.040 x 0.058	11.02 - 58.26
Gd_4GeSb_2	$Gd_4Ge_{1.1(1)}Sb_{1.9(1)}$	*I*-43*d*	9.1250(8)	759.8(1)	0.036 x 0.046 x 0.064	10.94 - 57.80
$Gd_4Ge_{0.5}Sb_{2.5}$	$Gd_4Ge_{0.59(8)}Sb_{2.41(8)}$	*I*-43*d*	9.1694(7)	770.9(1)	0.018 x 0.024 x 0.046	10.90 - 58.30
Gd_4Sb_3	Gd_4Sb_3	*I*-43*d*	9.2149(6)	782.48(9)	0.033 x 0.059 x 0.080	10.84 - 58.00

Index ranges	**Reflections collected**	**Independent reflections**	**Completeness to max 2θ (%)**	**Data/restraints /parameters**	**Goodness-of-fit on F^2**	**Final R indices [I > 2σ(I)]**	**R indices (all data)**
$-12 \leq h \leq 12$, $-12 \leq k \leq 12$, $-12 \leq l \leq 12$	3369	176 [R(int) = 0.2089]	100	176 / 0 / 9	1.109	R_1 = 0.0424, wR_2 = 0.0859	R_1 = 0.0530, wR_2 = 0.0887
$-11 \leq h \leq 12$, $-12 \leq k \leq 12$, $-12 \leq l \leq 10$	3505	176 [R(int) = 0.1143]	100	176 / 0 / 8	1.081	R_1 = 0.0454, wR_2 = 0.0722	R_1 = 0.0574, wR_2 = 0.0751
$-12 \leq h \leq 12$, $-12 \leq k \leq 12$, $-12 \leq l \leq 9$	3745	179 [R(int) = 0.0906]	100	179 / 0 / 9	1.007	R_1 = 0.0331, wR_2 = 0.0257	R_1 = 0.0414, wR_2 = 0.0265
$-9 \leq h \leq 12$, $-12 \leq k \leq 12$, $-12 \leq l \leq 12$	3545	180 [R(int) = 0.0585]	100	180 / 0 / 8	1.290	R_1 = 0.0168, wR_2 = 0.0243	R_1 = 0.0208, wR_2 = 0.0246

Extinction coefficient	Largest diff. peak and hole
0.0003(3)	1.620 and -1.108
0.0000(2)	1.803 and -1.484
0.00012(3)	1.620 and -1.153
0.00024(6)	0.882 and -0.822

Table S3.2. Atomic and isotropic temperature parameters (U, Å ^{2}) from the single crystal X-ray diffraction data of the $Gd_4Ge_{3-x}Sb_x$ (x = 1.5, 2, 2.5 and 3) series

Atom	Site	Occupancy	*x/a*	*y/b*	*z/c*	*U*
			$Gd_4Ge_{1.4(1)}Sb_{1.6(1)}$			
Gd1	16*c*	1	0.0689(1)	0.0689(1)	0.0689(1)	0.024(1)
Ge1/Sb1	12*a*	0.48/0.52(4)	0	¼	3/8	0.020(1)
			$Gd_4Ge_{1.1(1)}Sb_{1.9(1)}$			
Gd1	16*c*	1	0.0702(1)	0.0702(1)	0.0702(1)	0.016(1)
Ge1/Sb1	12*a*	0.38/0.62(4)	0	¼	3/8	0.011(1)
			$Gd_4Ge_{0.59(8)}Sb_{2.41(8)}$			
Gd1	16*c*	1	0.0710(1)	0.0710(1)	0.0710(1)	0.011(1)
Ge1/Sb1	12*a*	0.80/0.20(3)	0	¼	3/8	0.009(1)
			Gd_4Sb_3			
Gd1	16*c*	1	0.0721(1)	0.0721(1)	0.0721(1)	0.010(1)
Sb1	12*a*	1	0	¼	3/8	0.009(1)

Table S3.3. Crystallographic data and refinement results for the $Gd_4Ge_{3-x}Bi_x$ (x = 1, 1.5 and 2) single crystals

Loaded composition	**Refined composition**	**Space group**	**Lattice parameters *a*, Å**	**Volume, Å^3**	**Crystal size, mm^3**	**2*θ* range for data collection, °**
Gd_4Ge_2Bi	$Gd_4Ge_{2.07(2)}Bi_{0.93(2)}$	*I*-43*d*	9.0554(8)	742.6(1)	0.030 x 0.058 x 0.070	11.04 - 58.28
$Gd_4Ge_{1.5}Bi_{1.5}$	$Gd_4Ge_{1.66(7)}Bi_{1.34(7)}$	*I*-43*d*	9.1313(9)	761.4(1)	0.042 x 0.045 x 0.050	10.94 - 57.76
Gd_4GeBi_2	$Gd_4Ge_{1.08(5)}Bi_{1.92(5)}$	*I*-43*d*	9.2200(8)	783.8(1)	0.017 x 0.051 x 0.106	10.84 - 57.96

Index ranges	**Reflections collected**	**Independent reflections**	**Completeness to max 2θ (%)**	**Data/restraints /parameters**	**Goodness-of-fit on F^2**	**Final R indices [I > 2σ(I)]**	**R indices (all data)**
$-12 \leq h \leq 12$, $-12 \leq k \leq 12$, $-12 \leq l \leq 10$	3364	176 [R(int) = 0.0864]	100	176 / 0 / 9	1.058	R_1 = 0.0293, wR_2 = 0.0271	R_1 = 0.0385, wR_2 = 0.0281
$-12 \leq h \leq 12$, $-10 \leq k \leq 12$, $-12 \leq l \leq 12$	4021	176 [R(int) = 0.1925]	100	176 / 0 / 9	1.129	R_1 = 0.0529, wR_2 = 0.0687	R_1 = 0.0674, wR_2 = 0.0711
$-11 \leq h \leq 12$, $-12 \leq k \leq 12$, $-12 \leq l \leq 12$	3692	180 [R(int) = 0.1218]	100	180 / 0 / 9	1.012	R_1 = 0.0282, wR_2 = 0.0455	R_1 = 0.0343, wR_2 = 0.0462

Extinction coefficient	0.00035(6)	0.00010(14)	0.00027(9)
Largest diff. peak and hole	1.156 and -1.017	2.037 and -1.604	0.901 and -0.908

Table S3.4. Atomic and isotropic temperature parameters (U, Å^2) from the single crystal X-ray diffraction data of the $Gd_4Ge_{3-x}Bi_x$ (x = 1, 1.5 and 2) series

Atom	Site	Occupancy	*x/a*	*y/b*	*z/c*	*U*
			$Gd_4Ge_{2.07(2)}Bi_{0.93(2)}$			
Gd1	16*c*	1	0.0677(1)	0.0677(1)	0.0677(1)	0.018(1)
Ge1/Bi1	12*a*	0.690/0.310(8)	0	¼	3/8	0.009(1)
			$Gd_4Ge_{1.66(7)}Bi_{1.34(7)}$			
Gd1	16*c*	1	0.0688(2)	0.0688(2)	0.0688(2)	0.021(1)
Ge1/Bi1	12*a*	0.55/0.45(2)	0	¼	3/8	0.010(1)
			$Gd_4Ge_{1.08(5)}Bi_{1.92(5)}$			
Gd1	16*c*	1	0.0702(1)	0.0702(1)	0.0702(1)	0.020(1)
Ge1/Bi1	12*a*	0.36/0.64(2)	0	¼	3/8	0.010(1)

Table S3.5. X-ray powder refinement details of $Gd_4Ge_{3-x}P_x$ (x = 0.5, 1, 1.5) cast (left) and annealed (right) samples

Sample	Phases (~%)	
	Cast	**Annealed**
$Gd_4Ge_{2.5}P_{0.5}$	Gd_4Ge_3 (41)	Gd_4Ge_3 (70)
	Gd_5Ge_3 (34)	Gd_5Ge_3 (27)
	Gd_5Ge_4 (25)	GdP (3)
Gd_4Ge_2P	Gd_5Ge_3 (48)	Gd_5Ge_3 (58)
	Gd_4Ge_3 (40)	Gd_4Ge_3 (23)

	GdP (12)	GdP (19)
$Gd_4Ge_{1.5}P_{1.5}$	Gd_5Ge_3 (54) GdP (31) Gd_4Ge_3 (15)	Gd_5Ge_3 (62) GdP (38)

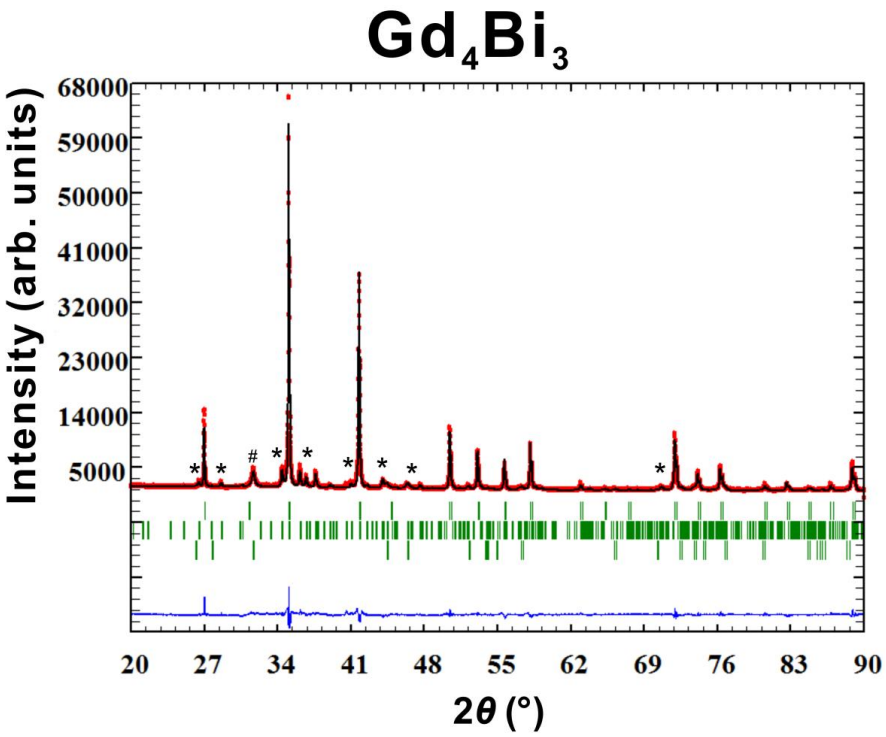

Figure S3.1. Experimental X-ray powder diffraction pattern (red) of Gd_4Bi_3 using Co K_α radiation collected in the 2θ range 20 to 90° with a 0.0084 step size. The Bragg's peaks (green) are positioned as follows- Gd_4Bi_3 (*I*-43*d*) (top), Gd_5Bi_3 (*Pnma*) (center), Bi (*R*-3*m*) (bottom). The calculated pattern (black) and the difference between the experimental and simulated powder patterns (blue) are also shown. The peaks denoted * and # indicate Gd_5Bi_3 and Bi impurities, respectively.

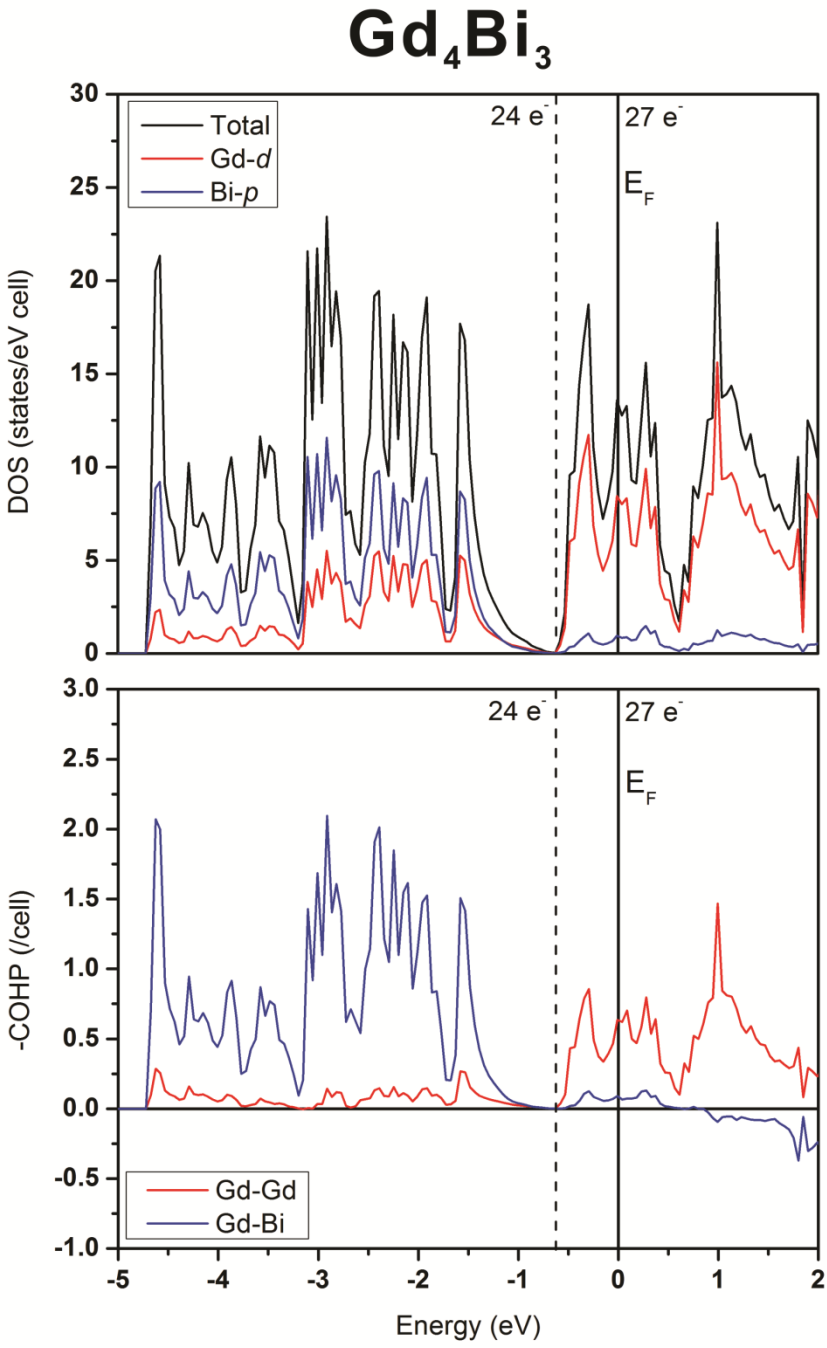

Figure S3.2. Density of States (DOS) and Crystal Orbital Hamilton Population (COHP) for Gd_4Bi_3.

Chapter 4: Structural and magnetic properties of $Gd_5Ge_{4-x}P_x$ (x = 0.25 - 0.63)

4.1 Abstract

The $Gd_5Ge_{4-x}P_x$ (x = 0.25–0.63) phases were synthesized and found to adopt the Sm_5Ge_4-type structure with broken interslab (Ge,P)–(Ge,P) dimers. According to the single crystal X-ray diffraction, substitution of the P for Ge atoms occurs only on the interslab site. Electronic band structure calculations performed with the TB-LMTO-ASA method confirmed the experimental site preference for the P atoms. Magnetization measurements indicated that all the $Gd_5Ge_{4-x}P_x$ samples are ferromagnetic with Curie temperatures ranging from 64 to 101 K. The ferromagnetic coupling in the samples increases with the P amount, and this is related to an increase in the valence electron concentration. A Griffiths-type phase is observed in the paramagnetic regions for all samples and its stability is discussed.

4.2 Introduction

The RE_5T_4 (RE = rare-earth element, T = p-element) family of phases have been studied extensively since the discovery of the giant magnetocaloric effect (GMCE) in $Gd_5Si_2Ge_2$ [7,48]. One of the most investigated system is the $Gd_5Ge_{4-x}Si_x$ (x = 0 - 4) one, which exhibits a variety of interesting magnetic properties such as magnetostriction, magnetoelastic effect and giant magnetoresistance [49–54]. The structural features of the

$Gd_5Ge_{4-x}Si_x$ phases are also intriguing; the three structures, identified in the system, are composed of two-dimensional $_\infty^2[Gd_5(Si,Ge)_4]$ slabs stacked in the ABAB... fashion along the *b* direction [55], however the bonding between the slabs is different. At low x ($0 \leq x \leq 1.2$), the orthorhombic Sm_5Ge_4-type structure (*Pnma*) with broken interslab *T*-*T* dimers is observed. In the intermediate region ($1.6 \leq x \leq 2.01$), the monoclinic $Gd_5Si_2Ge_2$-type ($P2_1/a$) structure, in which one half of the interslab *T*-*T* dimers, exists, and at high x ($2.3 \leq x \leq 4$), the orthorhombic Gd_5Si_4-type one (*Pnma*) with all interslab *T*-*T* dimers intact forms [8,56–58].

It has been observed, that the structural and magnetic properties of the $Gd_5Ge_{4-x}Si_x$ and RE_5T_4 phases, in general, can be altered through temperature [55], pressure [59], magnetic field [24,49,50] and chemical substitutions [58,60]. For example, the Gd_5Ge_4 phase, the end member of the pseudobinary $Gd_5Ge_{4-x}Si_x$ system, exhibits unique magnetic and structural transitions under the applied magnetic field in the low-temperature region. Upon cooling in a zero magnetic field and atmospheric pressure, this compound undergoes a second-order anti-ferromagnetic (AFM) transition with T_N = 128 K. However, below T_N, a magnetic field (H_{app} ~ 18 kOe at 4 K) [61] or hydrostatic pressure (exceeding 100 bar) [59] induces a first-order AFM-FM transition, accompanied by a Sm_5Ge_4-to-Gd_5Si_4 structural transition (and hence the GMCE) [24,50]. In addition to the GMCE, Gd_5Ge_4 also displays the Griffiths-like behaviour [62–64], magnetic glass state [65], training effects [66] and magnetic deflagation [67], etc.

Recent studies, employing heterovalent substitutions for Si, Ge or *RE*, have explored the effect of the valence electron concentration (VEC) on the structure and

properties of RE_5T_4 phases [9–11,19,25,26,29,34,68–74]. Research on the $Gd_5Ge_{4-x}Ga_x$ [11,26] and $Gd_5Si_{4-x}P_x$ [9,29] systems demonstrated that the interslab *T*-*T* distances and, thus, structures and magnetic properties of the RE_5T_4 phases can be tuned by adjusting the VEC. In the $Gd_5Ge_{4-x}Sb_x$ system [70,71], a small amount of electron-richer Sb leads to a first-order ferromagnetic ordering but without reformation of the interslab *T*-*T* dimers. Also, new phases with different structures have been discovered in the process; e.g. research on the $RE_5Ge_{4-x}In_x$ system, which looked both at the size and VEC effects, resulted in the discovery of the novel $RE_{11}Ge_8In_2$ phases [75]. In this study, we explore the $Gd_5Ge_{4-x}P_x$ system, where the P atoms are smaller (r_{cov}(P) = 1.10 Å vs. r_{cov}(Ge) = 1.22 Å) [40] but more electronegative than the Ge ones (χ(P) = 2.19 vs. χ(Ge) = 2.01) [76]. Depending on the dominance of the size or VEC effect, the broken interslab *T*-*T* dimers can be either reformed or elongated further. Here, we report on the structural and magnetic properties of the $Gd_5Ge_{4-x}P_x$ ($0 \leq x \leq 2.5$) system.

4.3 Experimental

4.3.1 Synthesis and X-ray structure analysis

Equimolar Gd (99.99 wt.%, distilled grade, Metall Rare Earth Limited, China) and Ge (99.9999 wt.%, Alfa Aesar) chunks were arc-melted under an Ar atmosphere for at least 5 times to ensure homogeneity. Next, the GdGe alloy was grounded into fine powder in an Ar-filled glovebox and combined with red P (99.999 wt.%, Puratronic, Alfa Aesar) powder in the equimolar portion. The powders were mixed thoroughly before pressing into pellets, which were then sealed in an evacuated silica tube and heated in the

following manner: to 400℃ at 50℃/h followed by a 12 h dwell, then to 800℃ at 50℃/h, followed by a 48 h dwell and quenched in cold water [29].

Phase analyses were performed using powder X-ray diffraction on a PANalytical X'Pert Pro diffractometer with a linear X'Celerator detector and CoK_α radiation at room temperature at each synthetic step. The P was found to substitute for Ge to form binary GdP and elemental Ge. The precursor powder was combined with the stoichiometric amounts of Gd fillings and Ge powder to make ~1 g of $Gd_5Ge_{4-x}P_x$ (x = 0.25–1.75) with x = 0.25 increments. In total, 7 samples were prepared. The powders were pressed into pellets and arc-melted for at least 3 times under an Ar atmosphere. Parts of the cast alloys from each sample were sealed in evacuated silica tubes and annealed at 800℃ for 2 weeks. The tubes were then quenched in cold water.

Single crystals were extracted from the samples with the loading compositions of x = 0.25 (annealed), 0.5 (cast), 0.75 (cast and annealed) and 1 (cast) on a STOE IPDSII diffractometer with a Mo K_α radiation in a full reciprocal sphere [14]. The program STRUCTURE TIDY [77] was used to standardize all the atomic positions. All the crystals adopt the orthorhombic Sm_5Ge_4–type structure with the *Pnma* space group. There are a total of 6 atomic positions: Gd1(4*c*), Gd2(8*d*), Gd3(8*d*), *T*1(8*d*), *T*2(4*c*) and *T*3(4*c*) (**Figure 4.1**). The refined compositions are x = 0.26(1) (loaded x = 0.25, annealed sample), 0.50(2) (loaded x = 0.5, cast), 0.63(2) (loaded x = 0.75, cast), 0.52(4) (loaded x = 0.75, annealed) and 0.58(3) (loaded x = 1.0, cast). The crystallographic data and refinement details for the single crystals with the refined x = 0.26(1), 0.50(2) and 0.63(2) are summarized in **Table 4.1** and **Table 4.2**. The refinements for the crystals with the refined

compositions x = 0.52(4) and 0.58(3) can be found in the **Supporting Information Table S4.1 and S4.2**. Further details of the crystal structures are available from the Fachinformationszentrum Karlsruhe, 76344 Eggenstein-Leopoldshafen, Germany, on quoting the depository number CSD–424758 for $Gd_5Ge_{3.74}P_{0.26}$, 424778 for $Gd_5Ge_{3.50}P_{0.50}$, 424788 for $Gd_5Ge_{3.37}P_{0.63}$ and 424779-80 for $Gd_5Ge_{3.48}P_{0.52}$ and $Gd_5Ge_{3.42}P_{0.58}$.

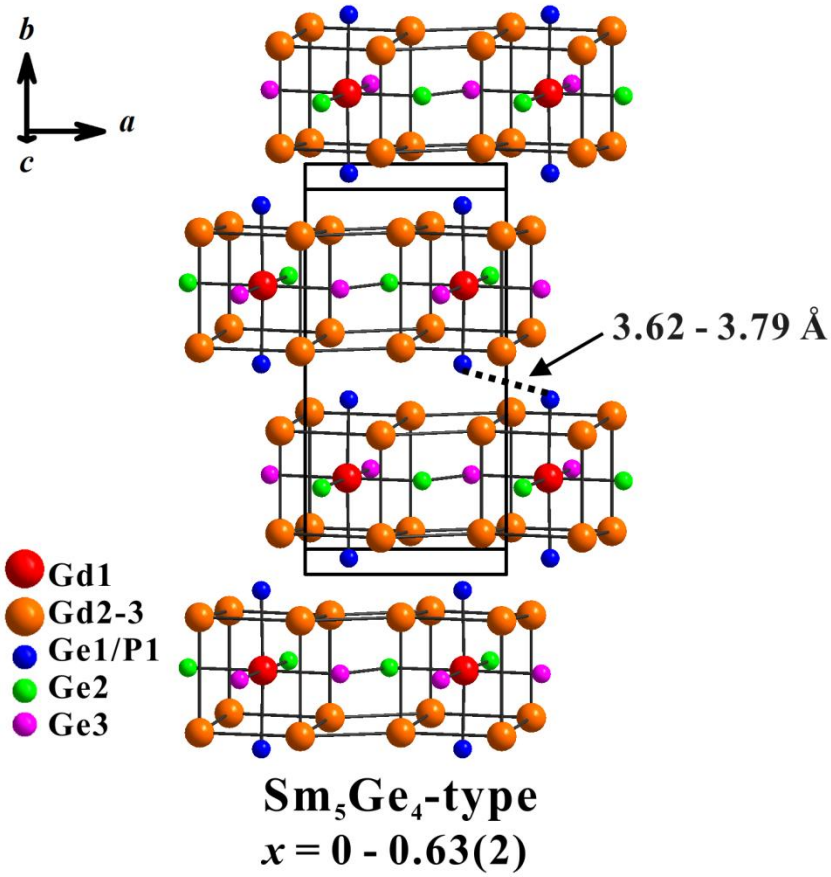

Figure 4.1 The crystal structure of Sm_5Ge_4-type $Gd_5Ge_{4-x}P_x$.

There are a total of 6 atomic positions, which belong to Gd1(4*c*), Gd2(8*d*), Gd3(8*d*), Ge1(8*d*), Ge2(4*c*) and Ge3(4*c*). The P atoms substitute for Ge on the interslab *T*1 (8*d*) site (indicated in blue).

Table 4.1 Crystallographic and refinement data for the $Gd_5Ge_{4-x}P_x$ (x = 0.25, 0.5, 0.75) single crystals.

Sample	**$Gd_5Ge_{3.75}P_{0.25}$ (annealed)**	**$Gd_5Ge_{3.50}P_{0.50}$ (cast)**	**$Gd_5Ge_{3.25}P_{0.75}$ (cast)**
Refined composition	$Gd_5Ge_{3.74(1)}P_{0.26(1)}$	$Gd_5Ge_{3.50(2)}P_{0.50(2)}$	$Gd_5Ge_{3.37(2)}P_{0.63(2)}$
Space group	*Pnma*	*Pnma*	*Pnma*
Lattice parameters *a*, Å	7.6936(3)/ 14.7517(8)/ 7.7493(4)	7.6807(5)/ 14.7036(8)/ 7.7469(4)	7.6813(7)/ 14.677(1)/ 7.7362(5)
Volume, Å ^{3}	879.50(7)	874.89(9)	872.1(1)
Crystal size, mm^3	0.051 x 0.085 x 0.115	0.045 x 0.092 x 0.124	0.040 x 0.048 x 0.069
2θ range for data collection, °	5.52 - 58.32	5.54 - 58.3	5.56 - 58.36
Index ranges	$-9 \le h \le 10$, $-20 \le k \le 19$, $-10 \le l \le 10$	$-10 \le h \le 10$, $-20 \le k \le 20$, $-9 \le l \le 10$	$-10 \le h \le 10$, $-19 \le k \le 20$, $-10 \le l \le 10$
Reflections collected	11291	8701	8268
Independent reflections	1232 [R(int) = 0.0542]	1222 [R(int) = 0.0786]	1219 [R(int) = 0.0801]
Completeness to max 2θ (%)	99.8	99.8	99.5
Data/restraints/ parameters	1232 / 0 / 48	1222 / 0 / 48	1219 / 0 / 48
Goodness-of-fit on F^2	1.070	1.065	0.865
Final R indices [I > 2σ(I)]	R_1 = 0.0247, wR_2 = 0.0317	R_1 = 0.0342, wR_2 = 0.0634	R_1 = 0.0300, wR_2 = 0.0333
R indices (all data)	R_1 = 0.0394, wR_2 = 0.0333	R_1 = 0.0502, wR_2 = 0.0670	R_1 = 0.0710, wR_2 = 0.0386
Extinction coefficient	0.00030(3)	0.00057(7)	0.00004(2)
Largest diff. peak and hole (e/Å $^{-3}$)	1.157 and -1.524	1.688 and -2.205	1.509 and -1.614

Table 4.2 Atomic and isotropic temperature parameters (U, Å ^{2}) from single crystal refinements for $Gd_5Ge_{3.74(1)}P_{0.26(1)}$, $Gd_5Ge_{3.50(2)}P_{0.50(2)}$ and $Gd_5Ge_{3.37(2)}P_{0.63(2)}$.

Atom	Site	Occupancy	*x/a*	*y/b*	*z/c*	*U*
			$Gd_5Ge_{3.74(1)}P_{0.26(1)}$			
Gd1	4*c*	1	0.2154(1)	¼	0.0008(1)	0.009(1)
Gd2	8*d*	1	0.0314(1)	0.1021(1)	0.6761(1)	0.011(1)
Gd3	8*d*	1	0.3829(1)	0.1157(1)	0.3385(1)	0.010(1)
Ge1/P1	8*d*	0.871/0.129(6)	0.2224(1)	0.0446(1)	0.0299(1)	0.010(1)
Ge2	4*c*	1	0.0878(1)	¼	0.3846(1)	0.010(1)
Ge3	4*c*	1	0.3334(1)	¼	0.6337(1)	0.010(1)
			$Gd_5Ge_{3.50(2)}P_{0.50(2)}$			
Gd1	4*c*	1	0.2203(1)	¼	0.0004(1)	0.013(1)
Gd2	8*d*	1	0.0384(1)	0.1037(1)	0.6743(1)	0.015(1)
Gd3	8*d*	1	0.3887(1)	0.1147(1)	0.3379(1)	0.014(1)
Ge1/P1	8*d*	0.748/0.252(9)	0.2269(2)	0.0450(1)	0.0263(1)	0.014(1)
Ge2	4*c*	1	0.0929(2)	¼	0.3821(2)	0.014(1)
Ge3	4*c*	1	0.3401 (2)	¼	0.6330(2)	0.014(1)
			$Gd_5Ge_{3.37(2)}P_{0.63(2)}$			
Gd1	4*c*	1	0.2231(1)	¼	0.0002(1)	0.011(1)
Gd2	8*d*	1	0.0426(1)	0.1045(1)	0.6730(1)	0.013(1)
Gd3	8*d*	1	0.3921(1)	0.1141(1)	0.3377(1)	0.012(1)
Ge1/P1	8*d*	0.683/0.317(8)	0.2296(2)	0.0453(1)	0.0237(2)	0.013(1)
Ge2	4*c*	1	0.0958(2)	¼	0.3804(2)	0.013(1)
Ge3	4*c*	1	0.3440(2)	¼	0.6325(2)	0.012(1)

4.3.2 Electronic structure calculations

To elucidate the atomic site preference of P atoms and rationalize structural stability, we performed tight-binding linear-muffin-tin-orbital (TB-LMTO) electronic structure calculations on Gd_5Ge_3P using the ASA method [32,33]. The lattice parameters of Gd_5Ge_3P were extrapolated from the single crystal data and they are a = 7.6845, b = 14.6262 and c = 7.7192 Å. The atomic coordinates were adopted from the $Gd_5Ge_{3.37(2)}P_{0.63(2)}$ single crystal refinement. The symmetry was reduced from *Pnma* to $Pn2_1/a$, which resulted in 9 atomic positions, with the Gd2, Gd3 and *T*1 8*d* sites from the former structure being split into two 4*a* sites. Three structural models were set up, with P fully occupying either the interslab *T*1, intraslab *T*2 or *T*3 site, respectively. Empty Wigner-Seitz (WS) atomic spheres were employed in the calculation using the automatic sphere generation. The basis set included the Gd: 6*s*, 6*p* and 5*d*; Ge: 4*s*, 4*p* and 4*d*; P: 3*s* and 3*p*; empty spheres. The Gd 6*p* and Ge 4*d* orbitals were treated by the Löwdin downfolding technique [32,33]. The Gd 4*f* electrons were treated as core electrons that do not participate in bonding. The WS radii of the atomic spheres were 2.96 - 3.54 Å for Gd and 2.63 - 3.04 Å for Ge and P. A total of 256 (8 x 4 x 8) irreducible *k*-points were used in the first Brillouin zone for reciprocal space integration using the tetrahedron method [36].

4.3.3 Magnetic measurements

Magnetic measurements were done on the $Gd_5Ge_{4-x}P_x$ (x = 0 - 1) samples using a Quantum Design SQUID magnetometer in a field cooled (FC) mode from 5 to at least

300 K with 2 K steps. All samples are ferromagnetic with Curie temperatures (T_C) ranging from 64 to 101 K (**Table 4.3**). The Weiss temperatures (θ) and magnetic moments (μ_B) were extracted from the paramagnetic region data above the Griffiths-phase region. Field-dependent magnetization measurements ($0 \leq H \leq 50$ kOe) were done on the $Gd_5Ge_{3.75}P_{0.25}$, $Gd_5Ge_{3.5}P_{0.5}$ and $Gd_5Ge_{3.25}P_{0.75}$ annealed samples at 5 K to gain further insights into their magnetic structures.

Table 4.3 Magnetic ordering temperatures, calculated Weiss temperatures (θ) and effective magnetic moment (μ_{eff}) extracted from the paramagnetic data above T_G for the $Gd_5Ge_{4-x}P_x$ (x = 0.25 - 0.75) samples.

Composition	Treatment	T_c (K)	θ (K)	μ_{eff} (μ_B)
x = 0.25	Cast	65	73	8.17
	Annealed	64	1	10.36
x = 0.5	Cast	87	85	8.60
	Annealed	79	36	8.92
x = 0.75	Cast	101	82	8.40
	Annealed	99	64	8.50

4.4 Discussion

4.4.1 Homogeneity Region and Structural Properties of $Gd_5Ge_{4-x}P_x$

X-ray phase analysis of the $Gd_5Ge_{4-x}P_x$ (x = 0–1.75) samples revealed that the orthorhombic Sm_5Ge_4-type phase was present in all the samples. While small amounts of the Gd_5Ge_3 and GdP impurities were detected in the x = 0.75 (annealed) and x = 1 (cast

and annealed) samples, their amount increased dramatically for $x > 1$. Samples with higher P concentrations, $1.5 \leq x \leq 1.75$, contained anti-Th_3P_4-type $Gd_4(Ge,P)_3$ as a major phase in addition to the impurities mentioned above (X-ray powder pattern of the $x = 1.75$ sample is shown in the **Supporting Information Figure S4.1**). Single crystal diffraction was used to gain further insights into the P substitution. Single crystals from the cast samples with the loading $x = 0.75$ and 1 had the refined P amounts of $x = 0.63(2)$ and $x = 0.58(3)$, respectively. Upon annealing, the $x = 0.75$ sample had the refined P amount of $x = 0.52(4)$. Thus, it appears that the P substitution does not exceed $x = 0.63(2)$ and this substitution level is reached in the cast sample with the loading $x = 0.75$. The identical Curie temperatures of 99 K for the cast samples with $x = 0.75$ and 1 further support the conclusion that the P substitution is maximized in the cast sample with $x = 0.75$ and does not increase for larger x values. It is likely, that the substitution level of $x = 0.63(2)$ can be obtained for loading P amounts lower than $x = 0.75$, but this has to be verified. In our discussions, only the refined samples with $x = 0.26(1)$ (loaded $x = 0.25$), $x = 0.50(2)$ (loaded $x = 0.50$) and $x = 0.63(2)$ (loaded $x = 0.75$) as well as on the pristine Gd_5Ge_4, will be discussed.

The $Gd_5Ge_{4-x}P_x$ phases adopt the Sm_5Ge_4-type structure with the interslab *T*-*T* dimers broken. At all substitution levels, smaller P enters the interslab *T*1 (8*d*) site and no P was detected on the intraslab *T*2 (4*c*) and *T*3 (4*c*) sites. Such preference for the *T*1 site is interesting, as smaller *T* atoms typically occupy the tighter *T*2 and *T*3 intraslab sites. E.g. in the $Gd_5Si_{4-x}T_x$ (*T* = Ge, Sn, Sb, Bi) systems with larger *T* atoms, the smaller Si atoms occupy predominantly the *T*2 and *T*3 intraslab sites [10,25,55,78]. Most likely,

such atomic distribution is electronically driven and it will be analyzed in the next chapter. As expected, due to the smaller P atomic size, the P substitution results in the unit cell volume reduction (see **Table 4.1**) and smaller average Gd-*T* and Gd-Gd bonds (3.092(3), 3.823(2) Å for Gd_5Ge_4 and 3.080(6), 3.759(4) Å for $Gd_5Ge_{3.37(2)}P_{0.63(2)}$ respectively). However, the *T*1-*T*1 and *T*2-*T*3 bonds become longer: *d*(*T*1-*T*1) increases from 3.6195(8) to 3.787(2) Å, and *d*(*T*2-*T*3) from 2.686(1) to 2.727(2) Å for $x = 0$ [34] and 0.63(2), respectively. Again, such elongation of the *T*1-*T*1 and *T*2-*T*3 bonds goes against the size arguments and, thus, must be electronic in origin, as discussed below.

4.4.2 Electronic band structure calculations of Gd_5Ge_3P

First, we will address preferential site occupancy in the $Gd_5Ge_{4-x}P_x$ phases. While an equal mixing of P/Ge on the *T* sites would maximize the entropy contribution to the Gibbs free energy, the electronic factors (enthalpy contribution) are likely to drive the P/Ge separation and minimize the total energy of the system. Distribution of different atoms over two or more independent sites is known as a "coloring problem" and it may be predicted by considering the bonding arrangement around the atoms and comparing their electronegativity [79]. In the Sm_5Ge_4-type structure, the interslab *T*1 atoms are terminal, i.e. they do not form homonuclear bonds with other *T* atoms. In contrast, the *T*2 and *T*3 atoms always form dimers, and some of the antibonding states (σ_p* and π*) within those dimers will be occupied as evidenced from the electronic formula $(Gd^{3+})_5(T1^{4-})_2(T2{-}T3)^{6-}[(1+x)e^-]$ (x is the amount of P). Since the P atoms are more electronegative than Ge (χ(P) = 2.19 *vs.* χ(Ge) = 2.01) [76], placing them into either *T*2 or *T*3 site would increase

populations of the antibonding states, thus, weaken the dimer bonding and decrease the bond energy.

This simple reasoning is supported by the electronic structure calculations on the three models of the hypothetical Gd_5Si_3P. **Figure 4.2** shows the DOS and COHP plots for Model 1 (P on the *T*1 site) and 2 (P on the *T*2 site), and those for Model 3 (P on the *T*3 site) can be found in the **Supporting Information, Figure S4.2**. We will focus on the *p* states of P and Ge, which comprise the valence band and stretch from -5 eV up in Model 1 and from -5.5 eV up in Model 2. Clearly, more of the antibonding states within the P2-Ge3 dimers should be occupied in Model 2 and this is supported by the COHP plots. On a more quantitative level, Model 2 has the total electronic energy that is 2.74 eV higher than for Model 1. The electronic structure of Model 3 is similar to that of Model 2 but its total electronic energy is 2.07 eV more than that of Model 1.

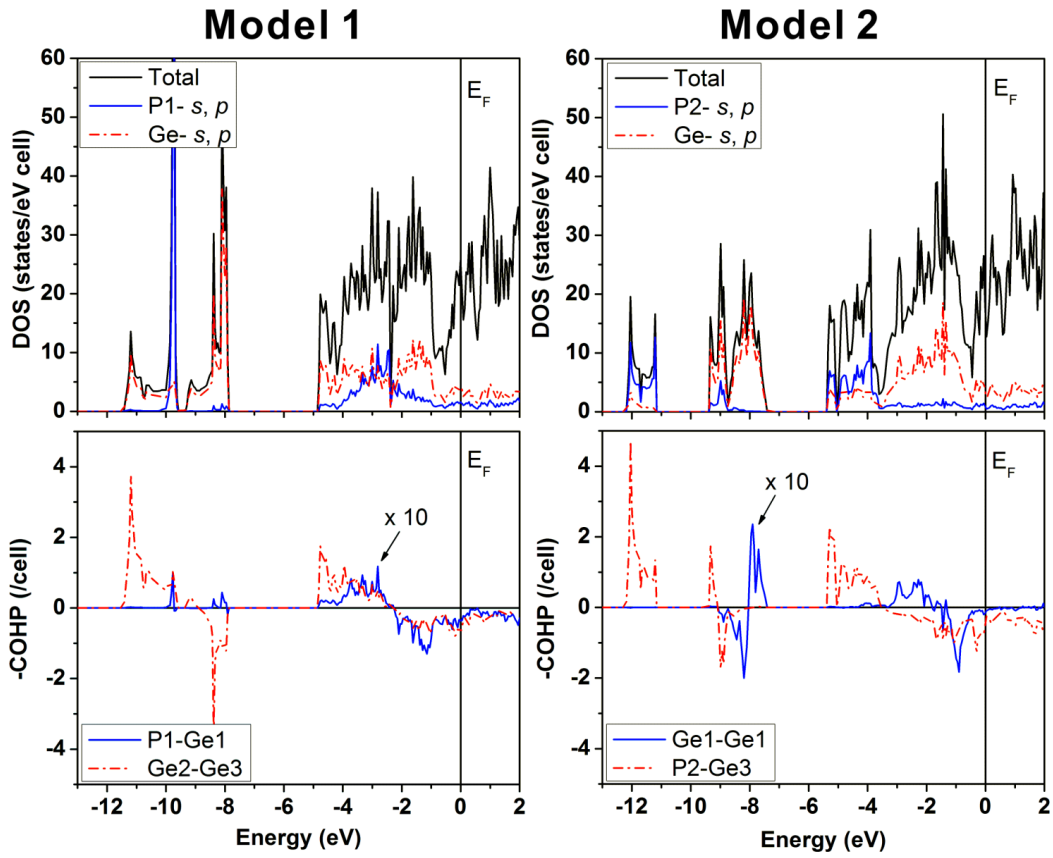

Figure 4.2 (Top) Total and projected densities of states (DOS). (Bottom) Crystal orbital Hamilton population (COHP) plots for the interslab *T*1-*T*1 (solid blue line) and intraslab *T*2-*T*3 (dashed red line) interactions in Gd_5Ge_3P.

In Model 1, the P atoms occupy half of the interslab *T*1 site. In Model 2, the P atoms occupy the intraslab *T*2 site fully.

Next, we will address the elongation of the *T*1-*T*1 and *T*2-*T*3 bonds. In our analysis, we will consider only Model 1, which is experimentally realized. According to the Zintl-Klemm approach [39], the electronic formulas of Gd_5Ge_4 and Gd_5Ge_3P can be written as $(Gd^{3+})_5(Ge1^{4-})_2(Ge2\text{-}Ge3)^{6-}(1e^-)$ and $(Gd^{3+})_5(Ge1^{4-})(P1^{3-})(Ge2\text{-}Ge3)^{6-}(2e^-)$, respectively. In Gd_5Ge_3P, one extra conduction electron will occupy more of the Ge2-Ge3 antibonding states (**Figure 4.2**), which will result in longer Ge2-Ge3 bonds. Although the

Ge1-P1 interactions are relatively weak, an additional electron will further weaken this bond and, thus, will lead to its stretching. So far, we are comparing Gd_5Ge_3P to Gd_5Ge_4, but similar arguments can be applied to the intermediate P amounts and be used to explain the stretching of the *T*1-*T*1 and *T*2-*T*3 bonds as the P amount increases.

4.4.3 Magnetic properties of $Gd_5Ge_{4-x}P_x$

All P-containing samples order ferromagnetically with Curie temperatures (T_C) ranging from 64 to 101 K (**Table 4.3**). According to the X-ray powder diffraction, the x = 0.75 sample contain the GdP and Gd_5Ge_3 impurities that order antiferromagnetically with T_N = 16 K [43] and T_N = 87 K [80], respectively. However, magnetic features of the GdP and Gd_5Ge_3 could not be observed, which is likely due to their low magnetic response (**Figure 4.3**). In addition to the original ferromagnetic transitions, the cast and annealed $Gd_5Ge_{3.75}P_{0.25}$ samples exhibit an additional transition slightly below their Curie temperatures. While the nature of this transition could not be reliably established from our data, it appears to be a spin reorientation. The cast $Gd_5Ge_{3.5}P_{0.5}$ sample has an additional ferromagnetic-like transition at ~152 K. Most likely, it belongs to a magnetic impurity since this impurity could not be detected on the X-ray powder diffraction pattern. Moreover, this transition disappears upon annealing. Since the transition temperatures of the x = 0.75 and x = 1 samples were similar and their refined P amounts were within 3 standard deviations, only the magnetic behaviour of the former is discussed. Magnetization data for the x = 1 sample can be found in **Supporting Information Figure S4.3 and S4.4**.

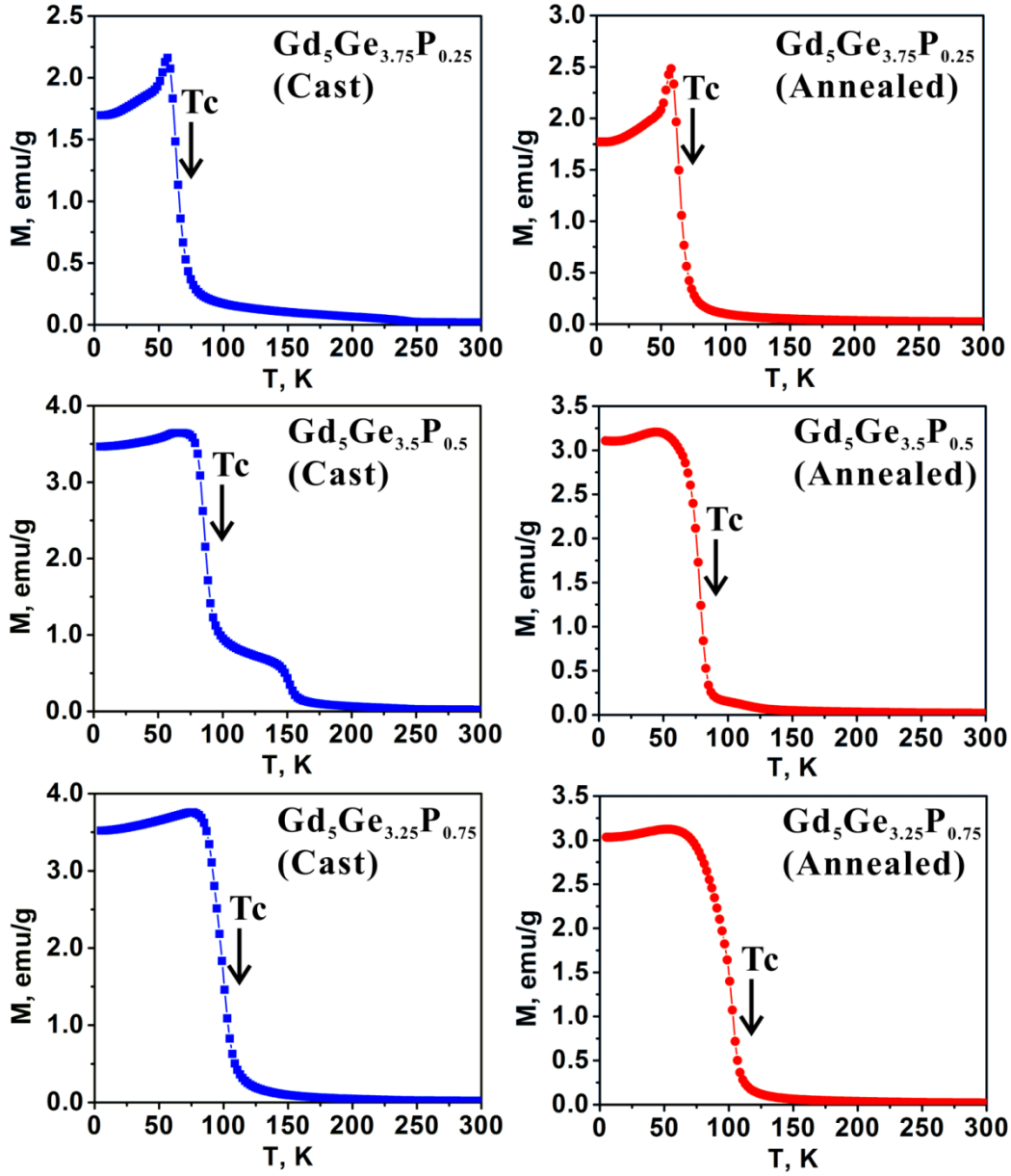

Figure 4.3 Magnetization of the cast (blue squares) and annealed (red circles) $Gd_5Ge_{4-x}P_x$ (x = 0.25, 0.5, 0.75) samples in the FC mode with a 100 Oe applied field. The Curie temperatures are denoted by T_c.

The Weiss temperatures (θ) and effective magnetic moments (μ_{eff}) of $Gd_5Ge_{4-x}P_x$ calculated from the paramagnetic region with $T > T_G$ are given in **Table 4.3** (T_G is defined

below and is shown in **Figure 4.5**). The positive θ values confirm that the dominant interactions are ferromagnetic in nature. Except for the annealed $Gd_5Ge_{3.75}P_{0.25}$ sample, the effective magnetic moments are close to each other. The calculated μ_{eff}/Gd values are higher than that expected for a free Gd^{3+} ion (7.94 μ_B). Larger Gd moments result from the polarization of the Gd 5*d* conduction electrons and this is often observed in the Gd-containing intermetallic phases [10,72,74,81,82].

The nature of magnetic interactions was further studied by performing field dependent measurements on the annealed $Gd_5Ge_{3.75}P_{0.25}$, $Gd_5Ge_{3.5}P_{0.5}$ and $Gd_5Ge_{3.25}P_{0.75}$ samples at 5 K (**Figure 4.4**). Relatively steep increases in magnetization and presence of a small hysteresis support the argument that the primary interactions are ferromagnetic in all these samples. However, a non-saturating behaviour and smaller than expected magnetic Gd moments in $Gd_5Ge_{3.75}P_{0.25}$ and $Gd_5Ge_{3.5}P_{0.5}$ suggest that the magnetic state is not fully ferromagnetic. Similar behaviour were observed in the $Gd_5Ge_{4-x}Si_x$ compounds with low Si content [83,84]. The saturation moment of 7.26 μ_B/Gd in $Gd_5Ge_{3.25}P_{0.75}$ is slightly larger than the theoretical value of 7 μ_B, which can be due to the 5*d* electron polarization.

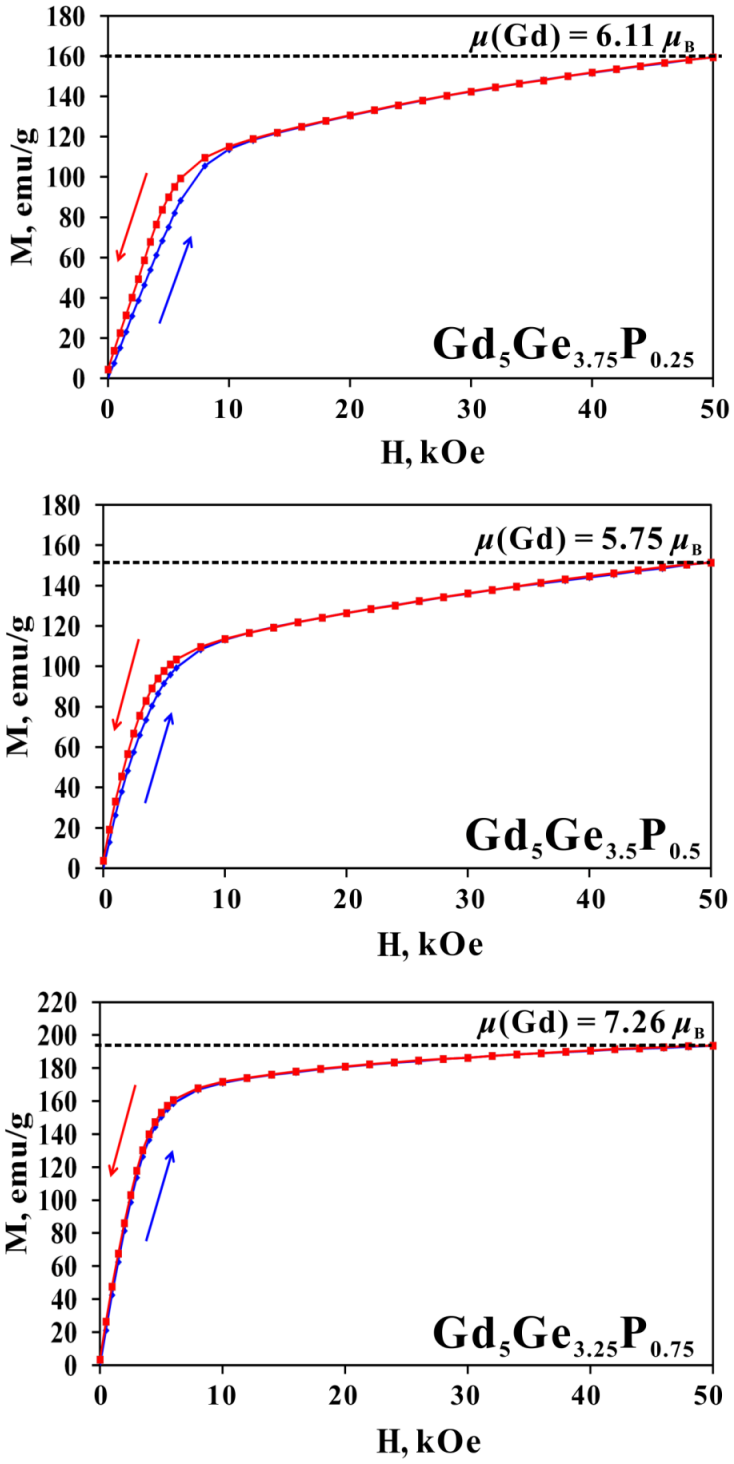

Figure 4.4 Field dependent magnetization measurements at 5 K for $Gd_5Ge_{3.75}P_{0.25}$, $Gd_5Ge_{3.5}P_{0.5}$ and $Gd_5Ge_{3.25}P_{0.75}$.

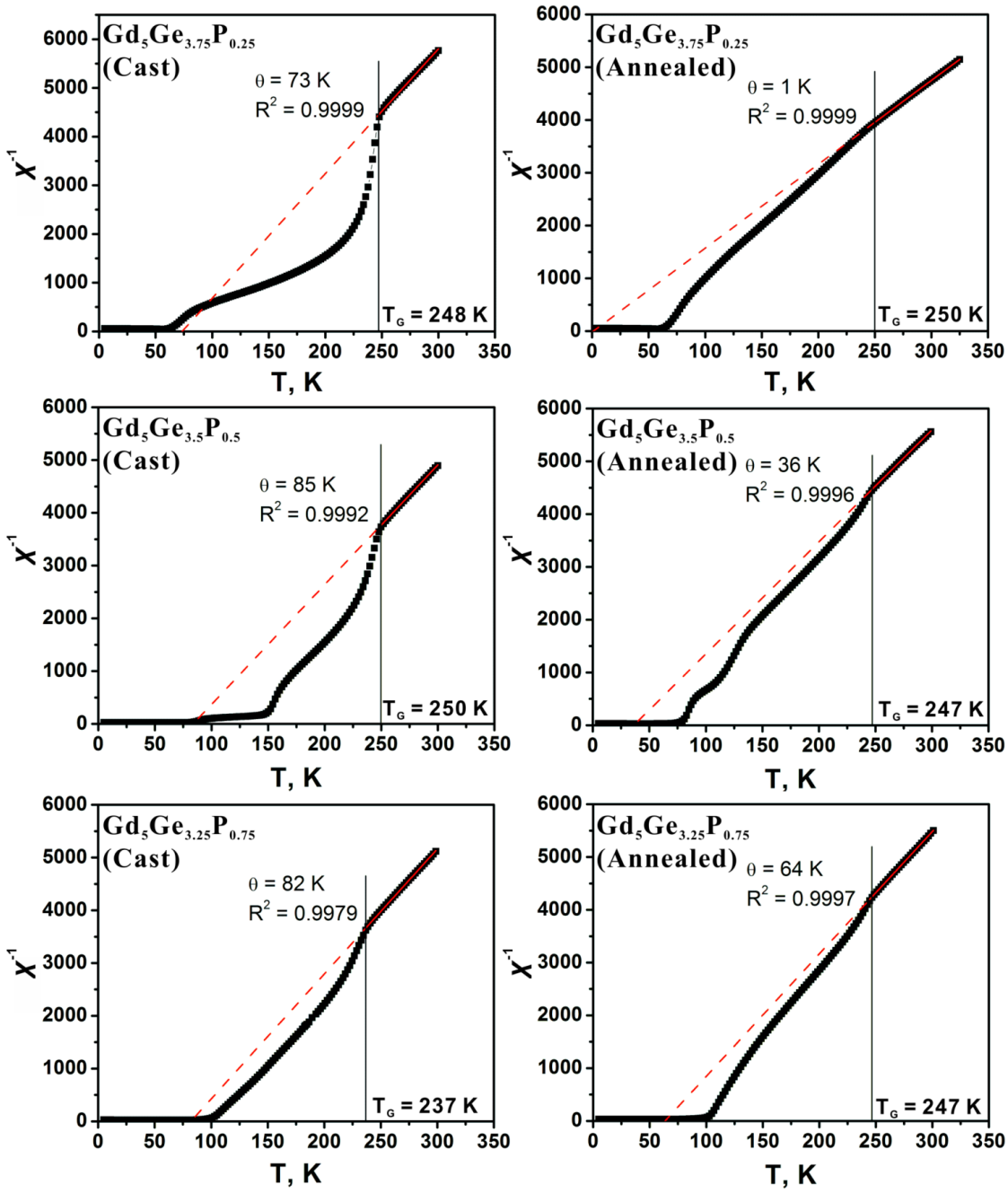

Figure 4.5 Inverse susceptibility vs. temperature for $Gd_5Ge_{4-x}P_x$ (x = 0.25, 0.5, 0.75) cast and annealed samples.

Dashed lines indicate extrapolations of the linear fits. The vertical lines indicate the T_G temperatures of the Griffiths-like phases.

One of the most intriguing features of the Gd_5Ge_4 and $Gd_5Ge_{4-x}P_x$ phases is a change in the magnetic ordering from the AFM to FM upon a relatively small P substitution of $x = 0.25$, while the structure remains the same. To understand the reasons for such a change, we will briefly discuss the magnetic structure of Gd_5Ge_4 first. The crystal structure of Gd_5Ge_4 consists of two-dimensional $_{\infty}^{2}[Gd_5Ge_4]$ slabs stacked along the *b* direction. Below the Neel temperature, the magnetic moments align ferromagnetically within each slab but couple antiferromagnetically with the neighbouring ones [85,86]. Such ordering results from the presence of two types of magnetic interactions. One is the ferromagnetic interactions between the Gd atoms within the slabs [86]. These intraslab interactions can be seen as the indirect Ruderman-Kittel-Kasuya-Yosida (*RKKY*) ones, and the Gd 4*f*–Gd 4*f* exchange coupling occurs via spin-polarized conduction electrons. Another type of interaction is between the Gd atoms from neighbouring slabs. These interslab couplings are viewed as superexchange interactions via the Gd–*T*–*T*–Gd pathways and are strongly dependent on the interslab *T*–*T* distances [87]. In the $Gd_5Ge_{4-x}Si_x$ system, the Gd–*T*–*T*–Gd coupling is ferromagnetic only when either the interslab *T*–*T* dimers are intact or reformed during the concomitant magnetostructural transition [87]. E.g. under the applied field of 18 kOe (at 4 K) [61], Gd_5Ge_4 undergoes a first-order structural transition (interslab *T*–*T* dimers are reformed) and orders ferromagnetically [24]. In the case of $Gd_5Ge_{4-x}P_x$, the *T*–*T* dimers always remain broken; therefore the nature of the ferromagnetic intralayer interactions is likely to be different. Moreover, the Curie temperatures of $Gd_5Ge_{4-x}P_x$ increase almost linearly with the VEC, which is indicative of the *RKKY* interactions.

Similar to Gd_5Ge_4, we believe that the individual $_{\infty}^{2}[Gd_5T_4]$ slabs in $Gd_5Ge_{4-x}P_x$ order ferromagnetically. Some indirect proof for this comes from the presence of short-range ferromagnetic interactions within the Griffiths phase (see below). The coupling between the slabs proceeds via the Gd–Gd *RKKY*-type interactions and thus, will depend on the Gd–Gd distances and number of conduction electrons, which is a function of the P amount. The relative changes in the Gd–Gd distances are rather small: e.g., the average interslab Gd–Gd distances decrease from 3.456 Å for $x = 0$, to 3.413 Å for $x = 0.26(1)$, 3.373 Å for $x = 0.50(2)$ and 3.350 Å for $x = 0.63(2)$. While such changes may influence the nature and temperature of the magnetic ordering, their effect is likely to be small. Additionally, if the Gd–Gd distances were a determining factor in the *RKKY* interactions, the $Gd_5Si_{4-x}Sb_x$ phases with the same Sm_5Ge_4 structure should show a decrease in the Curie temperatures (T_C), however they exhibit a similar increase in T_Cs, and this trend was attributed to the VEC changes [10]. We believe that an increase in the number of conduction electrons, represented by $(1+x)e^-$, promotes stronger ferromagnetic coupling between the slabs and raises the Curie temperatures in $Gd_5Ge_{4-x}P_x$. Also, a small VEC increase of $x = 0.25$ is sufficient enough to change the nature of the interslab coupling from antiferromagnetic in Gd_5Ge_4 to ferromagnetic in $Gd_5Ge_{3.75}P_{0.25}$.

The χ^{-1} vs. T plots reveal that the Curie-Weiss law is satisfied only at high temperatures, well above the Curie temperatures (**Figure 4.5**). The temperature, at which the paramagnetic state becomes fully disordered and above which the Curie-Weiss law is obeyed, is defined as T_G. In the $T_C < T < T_G$ region, the χ^{-1} vs. T data exhibit a non-linear behaviour, which attributed to the presence of a Griffiths-type phase [62]. A Griffiths

phase contains short-range FM clusters but is magnetically disordered on the macroscopic level. Interestingly, annealing of the $Gd_5Ge_{4-x}P_x$ samples decreases the amount of a Griffiths phase. Griffiths phases have been observed in the $Tb_5Si_2Ge_2$ [88], Dy_5Si_3Ge [89], Gd_5Ge_4 [63,64] and the pseudo-binary $Gd_5Ge_{4-x}Si_x$ ($0 \leq x \leq 2$) compounds [90]. A response from a Griffiths phase is extremely sensitive to the magnetic field and it can only be observed in fields not exceeding ~ 500 Oe [63]. At high fields, the weak ferromagnetic interactions are masked by the paramagnetic component, as previously suggested by Deisenhofer *et al.* and Magen *et al*. [88,91].

It is believed that the competition between intra- and interslab magnetic couplings is likely to be the main cause for the appearance of this phase [88,90]. Based on our results and review of the literature data, we can add that within the RE_5T_4 phases, a Griffiths phase occurs only when the interslab *T*–*T* dimers are broken. It appears that the ferromagnetic coupling within the $_\infty^2[RE_5T_4]$ slabs is relatively strong and this leads to a short-range ordering within the slabs. However, this ordering does not propagate in three dimensions as the superexchange *RE*–*T*–*T*–*RE* pathways between the slabs are disrupted and other exchange interactions are weaken. Only when these *RE*–*T*–*T*–*RE* pathways become available through the *T*–*T* dimer formation or when other exchange interactions become viable, that the ferromagnetic ordering sets in. It also appears that the presence of some sort of a structural disorder is required for a Griffiths phase to develop. Reducing such disorder through annealing results in the decrease of a Griffiths phase. It is worth mentioning that the Griffiths phases develop around T_G ~ 250 K in the $Gd_5Ge_{4-x}P_x$ system. This temperature is close to those reported for the Gd_5Ge_4 and $Gd_5Ge_{4-x}Si_x$ (x = 0 – 2)

phases [63,64,90]. Since the T_G temperature of a Griffiths phase may be correlated to the strength of the Gd–Gd magnetic interactions within the slabs, we may assume that the strength of such interactions is similar in the $Gd_5Ge_{4-x}P_x$ and $Gd_5Ge_{4-x}Si_x$ systems.

4.5 Conclusions

The electron-richer $Gd_5Ge_{4-x}P_x$ (x = 0.25 – 0.63) phases have been successfully synthesized. All of them maintain the Sm_5Ge_4-type structure with broken interslab $T1$–$T1$ dimers similar to the parent Gd_5Ge_4 phase. Although smaller P atoms enter the interslab $T1$ sites, the interslab dimers not only remain broken, they stretch even further, as do the intraslab $T2$–$T3$ dimers. Such stretching of the $T1$–$T1$ and $T2$–$T3$ dimers results from the larger population of the antibonding states within the dimers and is promoted by larger valence electron concentration due to the P substitution.

An increase in valence electron concentration also strengthens the ferromagnetic interactions in $Gd_5Ge_{4-x}P_x$ as evidenced from the increased Curie temperatures. The layered nature of the $Gd_5Ge_{4-x}P_x$ structures and competition between the intra- and interslab Gd–Gd magnetic interactions result in the appearance of Griffiths-type phases in the paramagnetic regime. Presumably, local structural distortions are required for the development of short-range ferromagnetic interactions within the Griffiths phase. As the crystallinity of the samples is improved through the prolong heat treatment, the amount of the Griffiths phase is reduced.

4.6 Acknowledgements

This research is supported by the NSERC Discovery Grant.

4.7. Supporting Information

Table S4.1. Crystallographic and refinement data for the $Gd_5Ge_{3.48(4)}P_{0.52(4)}$ and $Gd_5Ge_{3.42(3)}P_{0.58(3)}$ single crystals.

Loaded composition	**$Gd_5Ge_{3.25}P_{0.75}$**	**Gd_5Ge_3P**
Refined composition	$Gd_5Ge_{3.48(4)}P_{0.52(4)}$	$Gd_5Ge_{3.42(3)}P_{0.58(3)}$
Space group	*Pnma*	*Pnma*
Lattice parameters *a*, Å	7.6784(7)/ 14.703(2)/ 7.7464(6)	7.690(1)/ 14.661(2)/ 7.738(2)
Volume, Å^3	874.6(1)	872.3(3)
Crystal size, mm^3	0.052 x 0.072 x 0.079	0.012 x 0.022 x 0.060
2θ range for data collection, °	5.54 – 58.46	5.56 – 58.44
Index ranges	$-8 \leq h \leq 10$, $-20 \leq k \leq 20$, $-10 \leq l \leq 8$	$-10 \leq h \leq 8$, $-20 \leq k \leq 20$, $-10 \leq l \leq 10$
Reflections collected	8366	8377
Independent reflections	1227 [R(int) = 0.0716]	1221 [R(int) = 0.1774]
Completeness to max 2θ (%)	99.5	99.3
Data/restraints/parameters	1227 / 0 / 48	1221 / 0 / 48
Goodness-of-fit on F^2	1.202	0.562
Final R indices [I > 2σ(I)]	R_1 = 0.0529, wR_2 = 0.1059	R_1 = 0.0354, wR_2 = 0.0397
R indices (all data)	R_1 = 0.0788, wR_2 = 0.1116	R_1 = 0.1497, wR_2 = 0.0564
Extinction coefficient	0.00044(8)	0.00005(2)
Largest diff. peak and hole (e/Å^{-3})	2.612 and -2.529	1.963 and -1.962

Table S4.2. Atomic and isotropic temperature parameters (U, Å^2) from single crystal refinements for $Gd_5Ge_{3.48(4)}P_{0.52(4)}$ and $Gd_5Ge_{3.42(3)}P_{0.58(3)}$.

Atom	**Site**	**Occupancy**	***x/a***	***y/b***	***z/c***	***U***
			$Gd_5Ge_{3.48(4)}P_{0.52(4)}$			
Gd1	4*c*	1	0.2214(2)	¼	0.0003(2)	0.015(1)
Gd2	8*d*	1	0.0397(1)	0.1038(1)	0.6739(1)	0.018(1)
Gd3	8*d*	1	0.3898(1)	0.1146(1)	0.3380(1)	0.016(1)

Ge1/P1	8*d*	0.74/0.26(2)	0.2273(3)	0.0452(2)	0.0253(3)	0.017(1)
Ge2	4*c*	1	0.0932(4)	¼	0.3815(4)	0.016(1)
Ge3	4*c*	1	0.3413(4)	¼	0.6330(4)	0.017(1)
			$Gd_5Ge_{3.42(3)}P_{0.58(3)}$			
Gd1	4*c*	1	0.2761(3)	¼	0.0002(2)	0.014(1)
Gd2	8*d*	1	0.0431(1)	0.6047(1)	0.1730(1)	0.018(1)
Gd3	8*d*	1	0.1076(1)	0.1141(1)	0.3378(1)	0.016(1)
Ge1/P1	8*d*	0.71/0.29(2)	0.2709(5)	0.0451(2)	0.0236(3)	0.019(1)
Ge2	4*c*	1	0.1566(5)	¼	0.6326(4)	0.018(1)
Ge3	4*c*	1	0.4043(6)	¼	0.3795(4)	0.019(1)

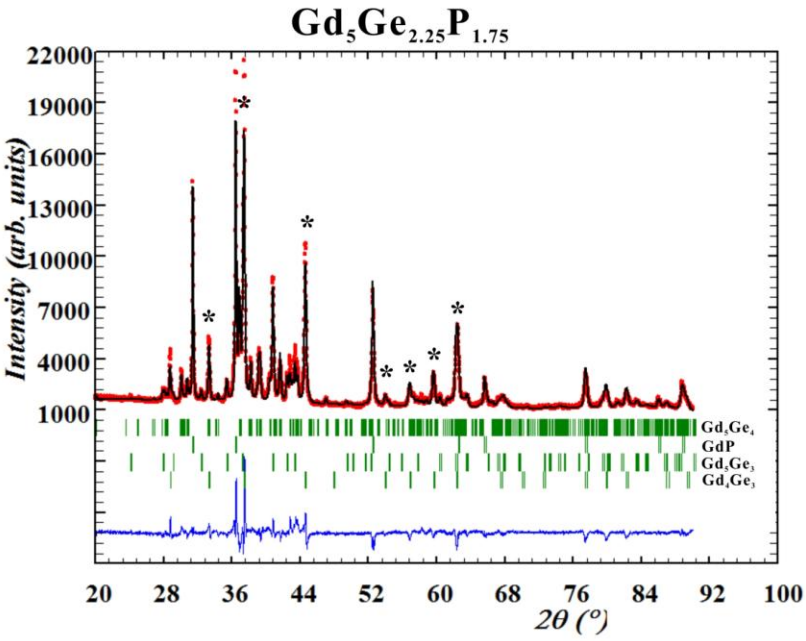

Figure S4.1. Experimental X-ray powder diffraction pattern (red) of $Gd_5Ge_{2.25}P_{1.75}$ using Co K_α radiation collected in the 2θ range 20 to 90° with a 0.0167 step size. The Bragg's peaks (green) are positioned as follows- Gd_5Ge_4 (*Pnma*) (first), GdP (*Fm*-3*m*) (second), Gd_5Ge_3 (*P*6$_3$/*mmc*) (third) and non-existent Gd_4Ge_3 (*I*-43*d*). The calculated pattern (black) and the difference between the experimental and simulated powder patterns (blue) are also shown. The peaks denoted * indicate the Gd_4Ge_3 impurity.

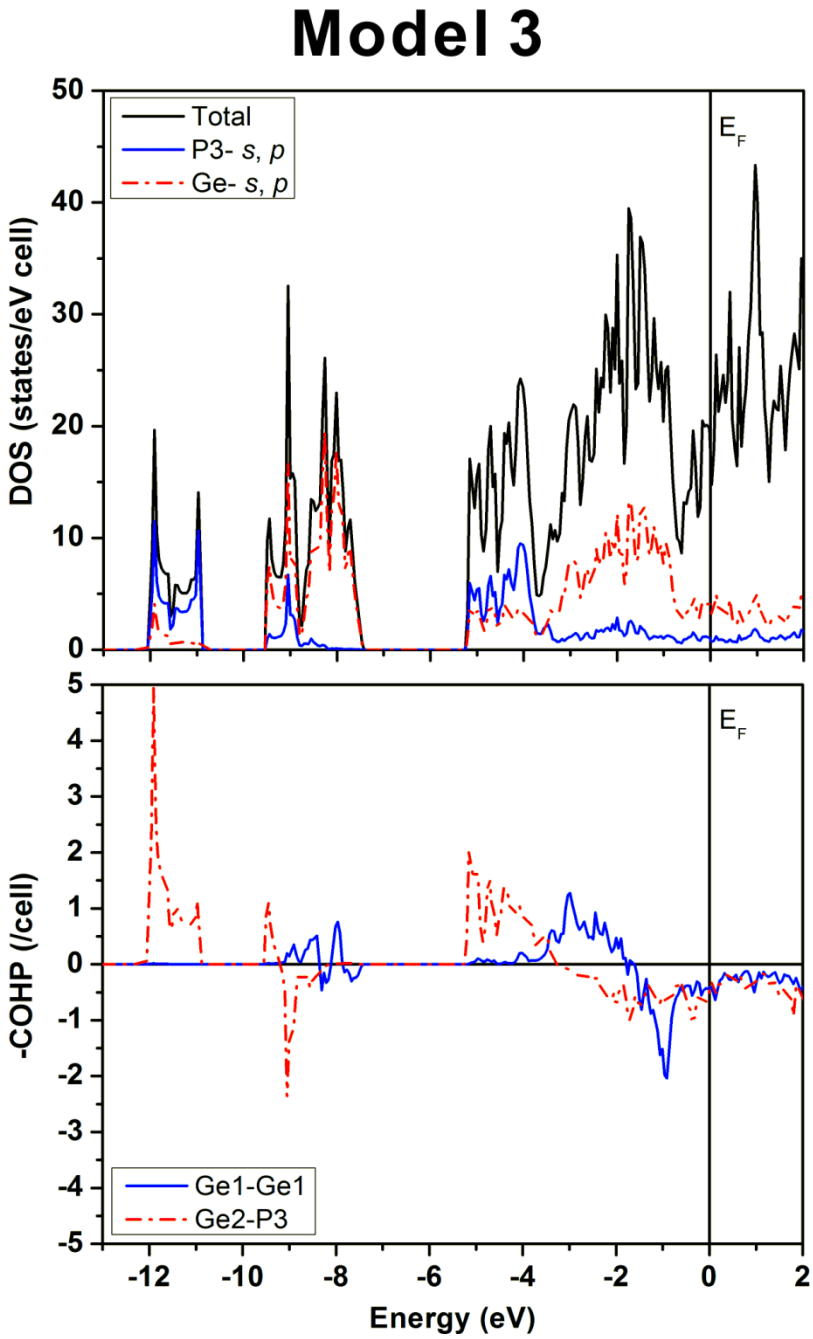

Figure S4.2. The total and projected densities of states (DOS) for the Ge and P atoms (upper) and the crystal orbital Hamilton population (COHP) plot (lower) for Gd_5Ge_3P. The P substitution occurs on the intraslab *T*3 site.

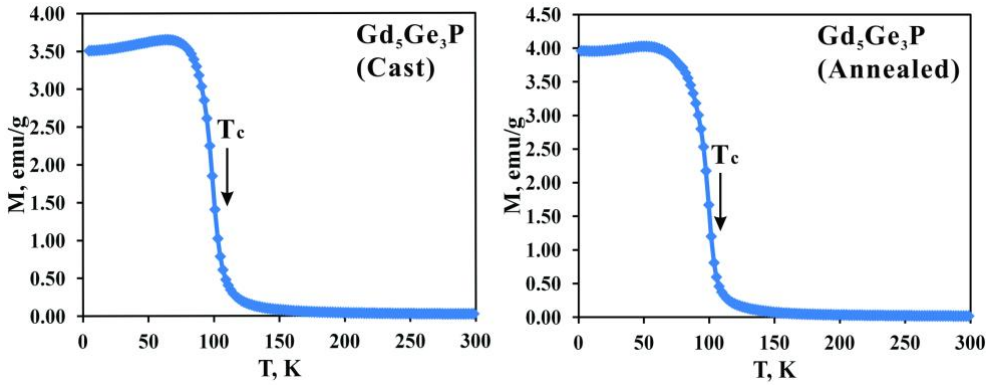

Figure S4.3. Magnetization vs. temperature plots of the Gd_5Ge_3P cast and annealed samples in the FC mode with 100 Oe applied field.

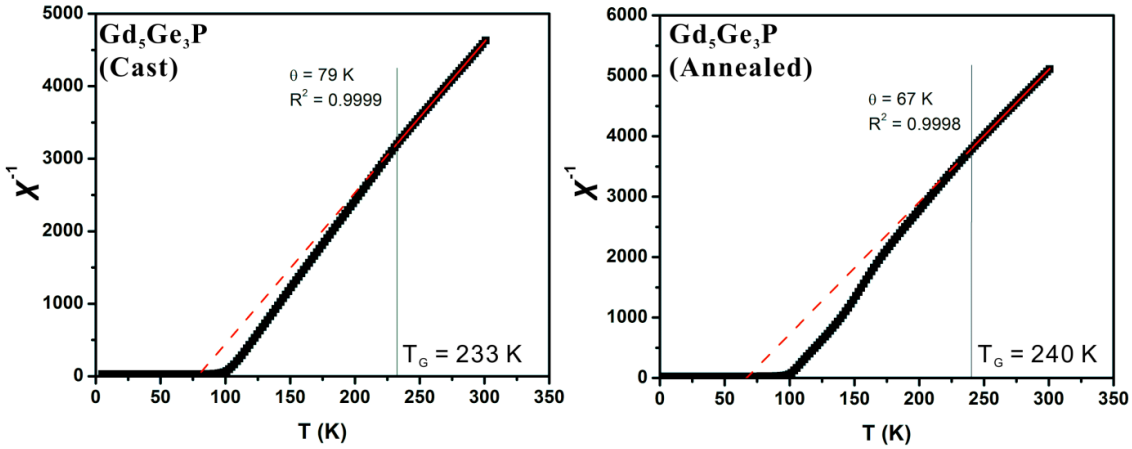

Figure S4.4. Inverse susceptibility vs. temperature plots for Gd_5Ge_3P cast and annealed samples. Dashed lines indicate extrapolations of the linear fittings.

Chapter 5: Tracking the Th_2Zn_{17}- and Th_2Ni_{17}-type phases in RE_2Fe_{17} (*RE* = Gd - Ho) by single crystal X-ray diffraction

5.1 Abstract

The RE_2Fe_{17} (*RE* = Gd – Ho) samples were synthesized by arc-melting and annealed in the temperature range from 850 to 1250℃. Formation and transformation of the rhombohedral 2-17*R* (*R*-3*m*) and hexagonal 2-17*H* ($P6_3/mmc$) structures were tracked using single crystal X-ray diffraction. Co-existence of both 2-17*R* and 2-17*H* is observed in the Gd – Ho -containing samples annealed at 1000℃. At lower and higher annealing temperatures, the co-existence becomes less apparent and one of the modifications dominates (2-17*R* for Gd-, Tb- and 2-17*H* for Dy-, Ho-). From the single crystal X-ray refinement, all the *RE* atoms are found to mix with the Fe dumbbells, which could originate from the *RE* deficiency in the samples.

5.2 Introduction

RE_2Fe_{17} (*RE* = rare earth metal) compounds have been studied extensively since the discovery of the $SmCo_5$ permanent magnet ($CaCu_5$-type structure, *P*6/*mmm* space group) [92]. In the $CaCu_5$-type MT_5 structures *M* atoms reside on the 1*a* (0, 0, 0) site and the transition metal atoms, *T*, on the 2*c* (1/3, 2/3, 0) and 3*g* (½ , 0, ½) sites [93]. The *M* atoms may be partially and randomly substituted with pairs of *T* atoms (also known as *T* dumbbells) on the 2*e* (0, 0, *z* and 0, 0, -*z*) site, while maintaining the same space group. The resulting structure is known as the $TbCu_7$-type one and it features an increased

amount of *T* [94]. When one third of the *M* atoms in the $CaCu_5$-type MT_5 structures are substituted by the *T*-*T* dumbbells in an ordered way, the 2-17 phases are obtained. Depending on the substitution pattern, the 2-17 compounds crystallize either with the rhombohedral or hexagonal symmetries. The rhombohedral Th_2Zn_{17}-type structure (2-17*R*, *R*-3*m*) forms when the *M*/*T* mixed planes are stacked in the ABCABC sequence and the hexagonal Th_2Ni_{17}-type (2-17*H*) structure ($P6_3/mmc$) forms when the mixed planes are stacked in the ABABAB sequence (**Figure 5.1**).

The light and heavy *RE* atoms tend to crystallize in the rhombohedral and hexagonal types, respectively. Either structure can be isolated in RE_2Fe_{17} with *RE* = Gd, Tb, Ce and Y [95,96]. In these phases, formation of a specific structure can be controlled by the annealing conditions and initial sample compositions. The rhombohedral phase forms at lower temperatures than the hexagonal, and therefore the 2-17*R* and 2-17*H* are also known as the low- and high- temperature phases, respectively. In most cases, both phases coexist within one sample and the sample composition can mainly depend on the synthetic techniques [96]. Pure 2-17*R* and 2-17*H* Gd_2Fe_{17} [97,98] and Tb_2Fe_{17} [99,100] have both been reported previously. For Tb_2Fe_{17}, Dariel *et al.* [99] reported that the sample composition played a significant role as arc-melted Tb- or Fe - rich samples could adopt 2-17*R* or 2-17*H* structures, respectively. Single crystal growth studies done by Chen *et al.* [100] reported that only the hexagonal phase could be isolated, no matter if the starting composition was stoichiometric, Tb- or Fe-rich. As for Dy- and Ho- containing 2-17, only the hexagonal phase was reported in the literature. However, by introducing an interstitial element, such as C and Ga into the Fe site, the structure could be transformed

from 2-17*H* at low concentrations to 2-17*R* at higher concentrations [101,102]. Therefore, there remains ambiguity in the formation of pure 2-17R in Dy_2Fe_{17} and Ho_2Fe_{17}.

Most experiments done previously employed single crystal growth or melt spinning syntheses, and the results were then analyzed by powder X-ray diffraction. In this work, we studied structure formations in the RE_2Fe_{17} (*RE* = Gd-Ho) samples synthesized by arc-melting and annealed under different conditions. The structural analysis was then done using single crystal X-ray diffraction technique. The presence of either 2-17*R* and/or 2-17*H* for the RE_2Fe_{17} (*RE* = Gd – Ho) compounds makes this class of materials interesting for single crystal X-ray diffraction studies.

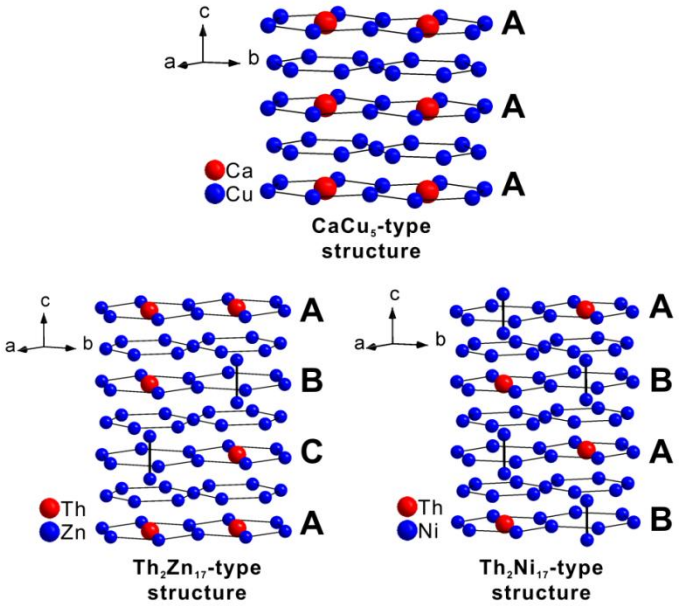

Figure 5.1 The parent $CaCu_5$-type structure (top), the Th_2Zn_{17} and the Th_2Ni_{17}-type structures with M/T planes stacked in the ABCABC sequences (bottom left) and ABABAB sequences (bottom right) respectively.

5.3 Experimental

5.3.1 Synthesis and X-ray analysis

Starting materials were pieces of Gd-Tm (99.9 wt.%, CERAC Inc.) and Fe (99.99 wt. %, Alfa Aesar). Stoichiometric RE_2Fe_{17} (*RE* = Gd - Tm) samples, each with a mass of one gram, were arc-melted under Ar atmosphere three times to achieve homogeneity. About half of the cast samples were then wrapped in Ta foil, sealed in evacuated silica tubes and annealed at 1000℃ for at least one week. The samples were then quenched in cold water. Powder X-ray phase analysis for the cast and annealed samples was done on a PANalytical diffractometer with the CoK_α radiation to avoid Fe fluorescence associated with the CuK_α radiation.

Single crystal X-ray diffraction was performed on the single crystals extracted from the RE_2Fe_{17} (*RE* = Gd - Tm) samples on a STOE IPDS II diffractometer with the Mo*Kα* radiation in the whole reciprocal sphere [14]. Crystal structures were solved and refined using *SHELXS* and *SHELXL* programs [15]. The refined crystal structures adopted either the hexagonal Th_2Ni_{17} ($P6_3/mmc$), rhombohedral Th_2Zn_{17} ($R\bar{3}m$), or contained both structure types. The lattice parameters of all samples obtained from single crystal X-ray diffraction are summarized in **Table 5.1**. Crystal data and structure refinements, atomic and isotropic temperature parameters of single crystals extracted from Gd_2Fe_{17} (2-17*R*) and Ho_2Fe_{17} (2-17*H*) annealed at 850℃ are presented in **Table 5.2** and **Table 5.3**.

Reciprocal space images were generated from the data collected for all the single crystals in order to track phase formations and transformations. Primarily, the analysis was performed on the (*h*0*l*) layer. Single crystals extracted from the RE_2Fe_{17} (*RE* = Gd,

Tb, Dy, Ho) samples exhibited triplets of diffraction peaks along the *c** direction, which is indicative of the Th_2Ni_{17} and Th_2Zn_{17} structures. These samples were further annealed at lower (850℃) and higher (1100℃, 1250℃) temperatures than the original one of 1000℃. A summary of the structure types present in the RE_2Fe_{17} (*RE* = Gd-Ho) phases is shown graphically in **Figure 5.2**.

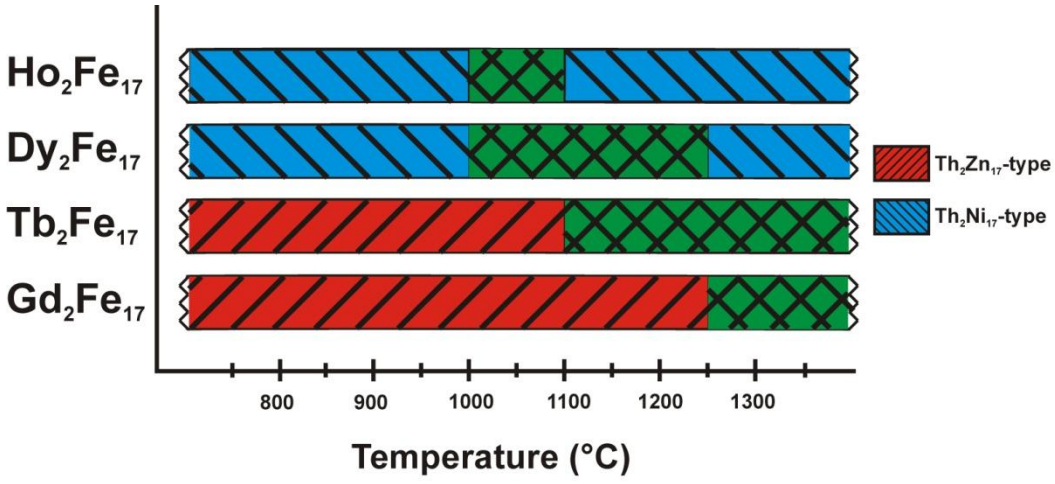

Figure 5.2 A graphical representation of the structural types present in the RE_2Fe_{17} (*RE* = Gd-Ho) phases.

Table 5.1 The lattice parameters (Å) from single crystal X-ray diffraction and the estimated amount of each phase.

Sample	Treatment	Structure (space group)	~ Amount of phase	Lattice parameters (Å)
Gd_2Fe_{17}	Cast	Th_2Zn_{17} (*R*-3*m*)	Equivalent	*a* = 8.528(1), *c* = 12.434(2)
		Th_2Ni_{17} ($P6_3/mmc$)	Equivalent	*a* = 8.516(1), *c* = 8.316(1)
	850℃, 1 week	Th_2Zn_{17} (*R*-3*m*)		*a* = 8.527(1), *c* = 12.410(1)
	1000℃, slow cooled [a]	Th_2Zn_{17} (*R*-3*m*)		*a* = 8.537(1), *c* = 12.424(1)
	1000℃, 11 days	Th_2Zn_{17} (*R*-3*m*)		*a* = 8.535(1), *c* = 12.450(2)
	1100℃, 2 hr	Th_2Zn_{17} (*R*-3*m*)	Major	*a* = 8.5198(7), *c* = 12.423(1)
		Th_2Ni_{17} ($P6_3/mmc$)	Minor	N/A
	1250℃, ind. furnace, 2 hr	Th_2Zn_{17} (*R*-3*m*)	Major	*a* = 8.5321(5), *c* = 12.4398(8)

		Th_2Ni_{17} ($P6_3/mmc$)	Minor	a = 8.524(1), c = 8.310(1)
Tb_2Fe_{17}	Cast	Th_2Ni_{17} ($P6_3/mmc$)	Major	a = 8.475(1), c = 8.284(2)
		Th_2Zn_{17} (R-3m)	Minor	a = 8.496(6), c = 12.440(8)
	850℃, 1 week	Th_2Zn_{17} (R-3m)		a = 8.491(1), c = 12.404(2)
	1000℃, 19 days	Th_2Zn_{17} (R-3m)		a = 8.506(1), c = 12.419(2)
	1100℃, 1 day	Th_2Zn_{17} (R-3m)	Major	a = 8.499(1), c = 12.385(2)
		Th_2Ni_{17} ($P6_3/mmc$)	Minor	a = 8.472(3), c = 8.307(3)
Dy_2Fe_{17}	Cast	Th_2Ni_{17} ($P6_3/mmc$)		a = 8.453(1), c = 8.284(1)
	1000℃, 19 days	Th_2Zn_{17} (R-3m)	Major	a = 8.490(1), c = 12.400(2)
		Th_2Ni_{17} ($P6_3/mmc$)	Minor	a = 8.480(1), c = 8.289(1)

	1250℃, ind. furnace, 4 hr	Th_2Ni_{17} (*P*6$_3$/*mmc*)		*a* = 8.453(1), *c* = 8.327(1)
	1100℃, 2 hr	Th_2Zn_{17} (*R*-3*m*)	Major	*a* = 8.476(1), *c* = 12.386(2)
		Th_2Ni_{17} (*P*6$_3$/*mmc*)	Minor	*a* = 8.482(3), *c* = 8.280(3)
Ho_2Fe_{17}	Cast	Th_2Ni_{17} (*P*6$_3$/*mmc*)		*a* = 8.4359(8), *c* = 8.2752(8)
	850℃, 1 month	Th_2Ni_{17} (*P*6$_3$/*mmc*)		*a* = 8.4374(9), *c* = 8.2785(8)
	1000℃, slow cooled [a]	Th_2Ni_{17} (*P*6$_3$/*mmc*)		*a* = 8.462(2), *c* = 8.279(2)
	1000℃, 1 month	Th_2Ni_{17} (*P*6$_3$/*mmc*)	Major	*a* = 8.4552(6), *c* = 8.2760(6)
		Th_2Zn_{17} (*R*-3*m*)	Minor	*a* = 8.4665(8), *c* = 12.3786(1)
	1100℃, 1 day	Th_2Ni_{17} (*P*6$_3$/*mmc*)		*a* = 8.4424(9), *c* = 8.2626(8)
	1250℃, ind. furnace, 4 hr	Th_2Ni_{17} (*P*6$_3$/*mmc*)		*a* = 8.434(2), *c* = 8.292(2)

[a] Annealed at 1000℃ for 24 hr, then cooled to room temperature with a rate of 10℃/hr.

Table 5.2 Single crystal data and structure refinement for Gd_2Fe_{17} and Ho_2Fe_{17}.

Loaded composition	Gd_2Fe_{17}	Ho_2Fe_{17}
Refined composition	$Gd_{1.967(7)}Fe_{17.07(8)}$	$Ho_{1.89(1)}Fe_{17.2(1)}$
Space group	*R*-3*m*	$P6_3/mmc$
Lattice parameters *a*/*c*, Å	8.527(1), 12.410(1)	8.4374(9), 8.2785(8)
Volume, Å ^{3}	781.49(11)	510.39(9)
Crystal size, mm^3	0.019 x 0.071 x 0.072	0.029 x 0.060 x 0.086
2θ range for data collection, °	6.42 - 58.36	5.58 - 58.36
Index ranges	$-10 \leq h \leq 11$, $-11 \leq k \leq 9$, $-16 \leq l \leq 16$	$-9 \leq h \leq 11$, $-11 \leq k \leq 11$, $-11 \leq l \leq 11$
Reflections collected	3045	6741
Independent reflections	283 [R_{int} = 0.0489]	296 [R_{int} = 0.1012]
Completeness to max 2θ (%)	100.0	100.0
Data/restraints/parameters	283 / 0 / 31	296 / 0 / 33
Goodness-of-fit on F^2	1.043	1.051
Final R indices [I > 2σ(I)]	R_1 = 0.0244, wR_2 = 0.0337	R_1 = 0.0365, wR_2 = 0.0248
R indices (all data)	R_1 = 0.0347, wR_2 = 0.0351	R_1 = 0.0758, wR_2 = 0.0282
Extinction coefficient	0.00008(4)	0.00073(9)
Largest diff. peak and hole (e/Å $^{-3}$)	1.449 and -1.504	0.851 and -0.711

Table 5.3 Atomic and isotropic temperature parameters (U, Å ^{2}) for $Gd_{1.967(7)}Fe_{17.07(8)}$ and $Ho_{1.89(1)}Fe_{17.2(1)}$ from single crystal diffraction data

Atom	Site	Occupancy	*x/a*	*y/b*	*z/c*	*U*
			$Gd_{1.967(7)}Fe_{17.07(8)}$			
Gd1	6*c*	0.875(2)	0	0	0.3406(1)	0.007(1)
Fe11	6*c*	0.125(2)	0	0	0.238(1)	0.007(1)
Fe12	6*c*	0.125(2)	0	0	0.431(1)	0.007(1)
Fe21	6*c*	0.783(2)	0	0	0.0963(2)	0.008(1)
Gd21	3*a*	0.108(1)	0	0	0	0.008(1)
Fe2	9*d*	1	½	0	½	0.007(1)
Fe3	18*h*	1	0.5006(1)	0.4994(1)	0.1599(1)	0.009(1)
Fe4	18*f*	0.777(6)	0.2930(3)	0	0	0.008(1)
Fe41	36*i*	0.112(3)	0.378(2)	0.043(1)	0.9995(7)	0.008(1)
			$Ho_{1.89(1)}Fe_{17.2(1)}$			
Ho1	2*c*	0.979(5)	1/3	2/3	¼	0.006(1)
Fe11	4*f*	0.021(5)	1/3	2/3	0.11(2)	0.006(1)
Ho2	2*b*	0.784(6)	0	0	¼	0.011(1)
Fe21	4*e*	0.216(6)	0	0	0.106(3)	0.011(1)
Ho3	2*d*	0.130(3)	1/3	2/3	¾	0.006(1)
Fe31	4*f*	0.870(3)	1/3	2/3	0.8931(4)	0.006(1)
Fe4	12*k*	1	0.1659(2)	0.3317(4)	0.0142(2)	0.009(1)
Fe5	6*g*	1	½	0	0	0.008(1)
Fe6	12*j*	0.861(7)	0.3698(4)	0.0399(4)	¼	0.009(1)
Fe61	12*j*	0.139(7)	0.285(3)	0.001(2)	¼	0.009(1)

5.3.2 Electron probe microanalysis (EPMA)

Electron probe microanalysis (EPMA) was performed on the RE_2Fe_{17} (*RE* = Gd, Tb, Dy, Ho) samples in order to determine the amounts of each element. The samples, their annealing conditions and established compositions are given in **Table 5.4**.

Table 5.4 Results obtained from EPMA.

Sample	Condition	Atomic *RE*	Atomic Fe
Gd_2Fe_{17}	cast	1.97(5)	17.03(5)
	1000℃, 11 days	1.99(5)	17.01(5)
	1250℃, 2 hr	2.04(5)	16.96(5)
	1000℃, slow cooled	1.98(5)	17.02(5)
Tb_2Fe_{17}	cast	2.04(9)	16.96(9)
	1000℃, 19 days	2.06(9)	16.94(9)
Dy_2Fe_{17}	cast	1.65(7)	17.35(7)
	1000℃, 19 days	1.78(7)	17.22(7)
Ho_2Fe_{17}	cast	1.71(7)	17.29(7)
	1000℃, slow cooled	1.74(7)	17.26(7)

5.4 Results and Discussion

5.4.1 Phase composition of the RE_2Fe_{17} (*RE* = Gd - Ho) samples

Phase analyses done by X-ray powder diffraction showed that the powder patterns of the RE_2Fe_{17} (*RE* = Gd, Tb, Dy, Ho) samples differ depending on the annealing temperature and conditions.

Analysis of the reciprocal *h*0*l* layers (*a***c** planes), generated from the single crystal X-ray diffraction data, permits relatively easy identification of the 2-17*R* and 2-17*H* structure, as the *c* (and *c**) lattice parameters of the 2-17*R* and 2-17*H* structures are

different. In the cases where both structure types are present in the samples, triplets of diffraction spots are observed along the c^* direction. These reciprocal layers were used to identify the two structures. The rhombohedrally-centered hexagonal setting was used for the 2-17*R* structure, although two settings for rhombohedral-centered lattices are possible - obverse and reverse with the following reflection conditions: $-h + k + l = 3n$ and $h - k + l = 3n$, respectively. These two settings represent two enantiomorphs, both of which were observed in the 2-17*R* phases studied here.

For some of the studied single crystals and depending on the annealing conditions, "triplets" of diffraction peaks could be observed along the c^* direction, in which only one out of the three could satisfy the reflection conditions for either the hexagonal or rhombohedral structures. The peak situated in the middle of the "triplet" belongs to the hexagonal structure. The other two belong to the obverse and reverse twins of the rhombohedral space group. The intensity ratio between the hexagonal and rhombohedral structures was nearly equal when the samples were annealed at 1000℃. An example of the ($h0l$) layer image extracted from the Tb_2Fe_{17} sample annealed at 1000℃ is shown (**Figure 5.3**).

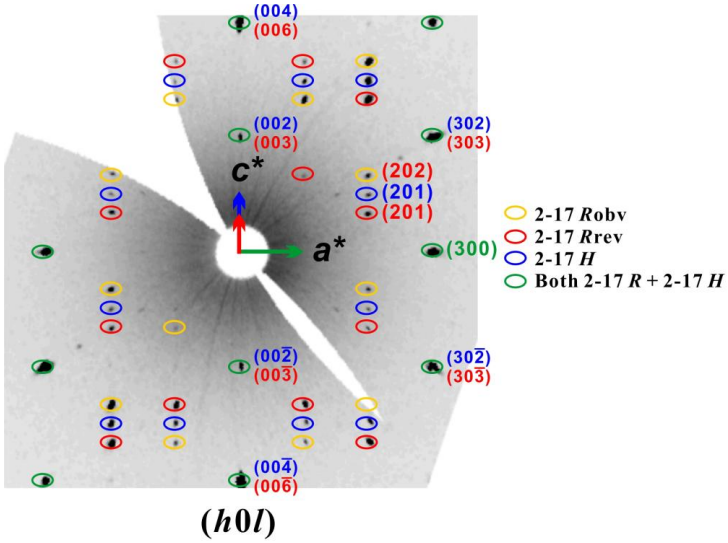

Figure 5.3 A (*h*0*l*) layer image generated from a single crystal extracted from the Tb_2Fe_{17} sample annealed at 1000℃.

The Gd_2Fe_{17} and Tb_2Fe_{17} compounds were known to crystallize in either 2-17*R* or 2-17*H*, depending on the annealing conditions. According to the binary phase diagram for Gd_2Fe_{17}, the low-temperature rhombohedral phase exists up to 1215℃, whereas the high-temperature hexagonal phase exists up to 1335℃ [103]. For Tb_2Fe_{17}, it was reported by Dariel *et al.* that the peritectic melting point exists at 1312℃, where the hexagonal structure could exist anywhere above 1050℃ [99]. Chen et al. reported that the compound melts congruently at 1316℃ [100]. The coexistence of both structural types have also been reported.

When the annealing temperature was decreased to 850℃, the Gd- and Tb- samples were rich in 2-17*R*, while the Dy- and Ho- samples were dominated by the 2-17*H* phases. At 1250℃, the co-existences of 2-17*R* and 2-17*H* continued to be present in the Gd- and

Tb- samples, although the formation of 2-17*R* is more favorable. In the Dy- and Ho- samples, the temperature region for the 2-17*R* and 2-17*H* coexistence was lower and narrower than the ones for Gd- and Tb- samples. At higher annealing temperatures, only the formation of 2-17*H* was observed across the Dy- and Ho- samples (**Figure 5.2**). Reciprocal (*h*0*l*) layer images of Gd_2Fe_{17} and Ho_2Fe_{17} samples annealed at 850℃ and 1250℃ are illustrated (**Figure 5.4**).

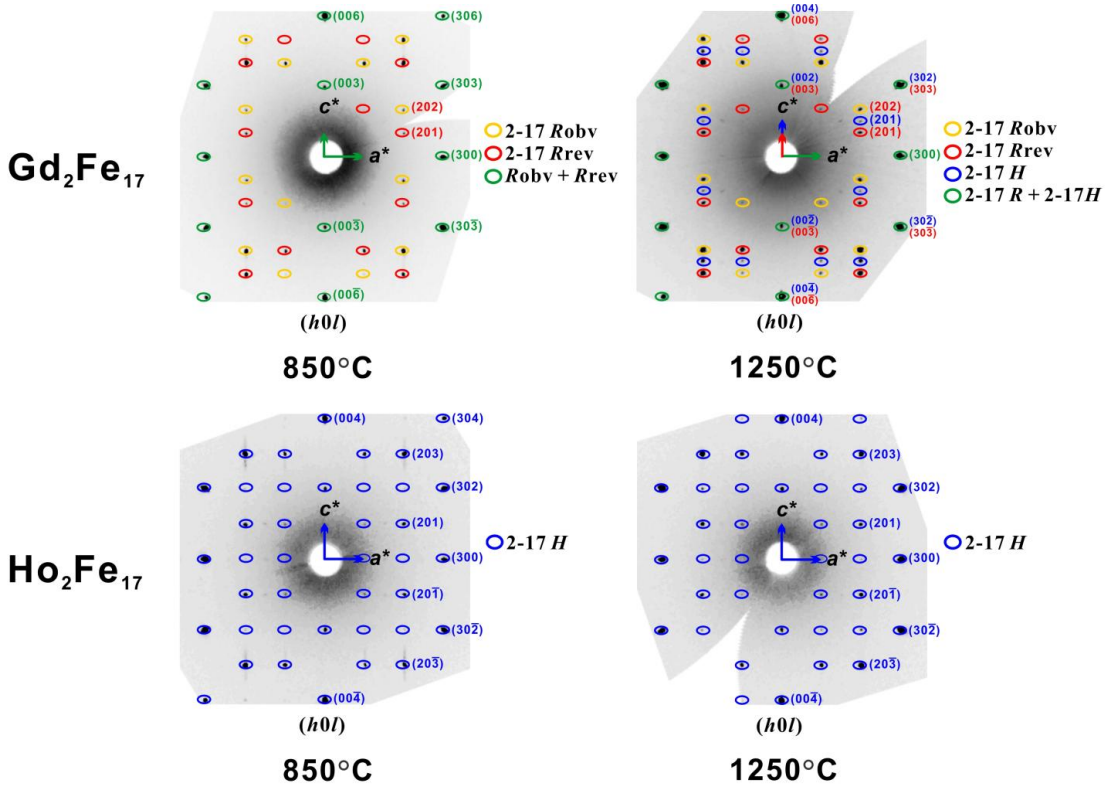

Figure 5.4 Several (*h*0*l*) layer images extracted from the Gd_2Fe_{17} and Ho_2Fe_{17} samples annealed at 850℃ and 1250℃.

5.4.2 Structural features and composition of the RE_2Fe_{17} (*RE* = Gd - Ho) phases

Based on the reciprocal space images, both the obverse and reverse components were observed in the rhombohedral *R* phase across all the single crystals. The R_{obv} phase could not be fully isolated without eliminating reflections from the R_{rev}, which resulted in a loss of at least half of the reflections for single crystal refinements. In addition, if the sample contained both 2-17*R* and 2-17*H* phases, it was difficult to determine the amount of each phase using single crystal X-ray diffraction due to the following reasons. 1) There were overlapped peaks belonging to both structure types. 2) The crystal could be twinned in more than one direction aside from the R_{obv} and R_{rev} twin; in the trigonal setting, it is common to have 120° rotational twins. 3) When both phases co-exist in the sample, it can be difficult to index the minor phase. Quantitative analysis of the X-ray powder patterns could not be performed conclusively since the samples were highly disordered, so most of the peaks, including the ones with high intensities overlapped. Furthermore, presence of preferred orientation further complicated the quantitative analysis of the powder data.

From the single crystal data all of the *RE* atom positions were found to mix with the Fe dumbbells along the *c* direction (**Table 5.3**). This was initially expected only for the Dy_2Fe_{17} and Ho_2Fe_{17} samples since the EPMA results showed that these samples were *RE* deficient. Previous literature work had also reported that by substituting extra Fe dumbbells onto the *RE* site, the 2-17*H* structure could be stabilized. However, there was Fe dumbbell substitutions on the *RE* site, as well as *RE* substitution on the Fe dumbbell site across all RE_2Fe_{17} samples studied in this present work. As a result, the structures have almost all atoms disordered across the sites, except for two Fe positions at the 9*d*

and 18*h* and 12*k* and 6*g* sites for 2-17*R* and 2-17*H*, respectively. A simplified crystallographic representation of the Gd_2Fe_{17} and Ho_2Fe_{17} single crystals is shown in **Figure 5.5**. The Fe atoms which do form dumbbell pairs have been removed from the picture for better visualization. Similar disordered structures have also been reported before in the Zr substituted Sm_2Fe_{17} [104].

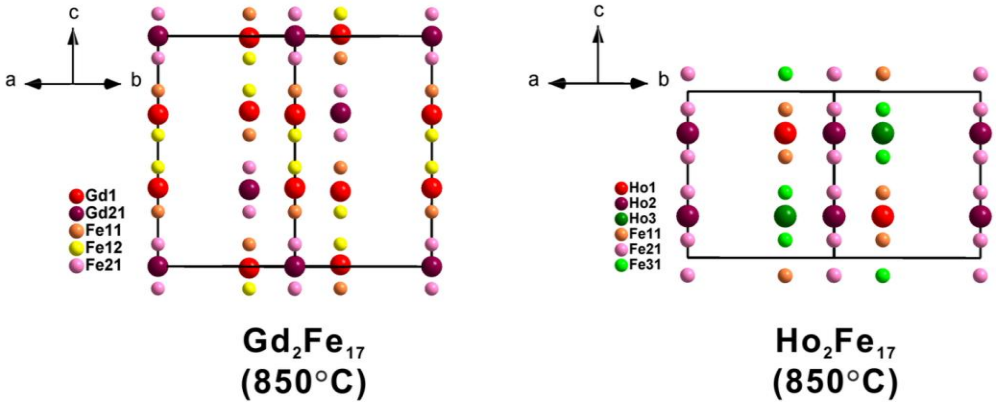

Figure 5.5 The visual crystallographic representation of Gd_2Fe_{17} and Ho_2Fe_{17} sample annealed at 850°C.

The Fe atoms which do not have mixed occupancies with the *RE* atoms are removed for better visualization.

Microprobe analysis showed a deficiency of *RE* in the Dy- and Ho- samples. In these samples, it was noted that the substitution decreased as the annealing temperature was lowered. The deficiency of *RE* in the cast samples may be a crucial factor as to why only the 2-17*R* is formed in Gd, despite the formation of either structural types reported. No pure 2-17*R* phase has been reported for Dy_2Fe_{17} and Ho_2Fe_{17} in literature. In the Tb

sample, both cast and annealed samples were Fe deficient. This explains why the 2-17*H* could not be obtained in this study as Dariel *et al.* reported that only 2-17*R* would be crystallized if the arc-melted sample is Tb-rich.[28]

5.5 Conclusions

The rhombohedral (*R*-3*m*) and hexagonal ($P6_3/mmc$) structural types of RE_2Fe_{17} (*RE* = Gd - Tm) were analyzed by single crystal X-ray diffraction. The presence of the two phases in the samples could be tracked by the analysis of reciprocal images generated for the (*h*0*l*) layers. The temperature range of 1000℃ seemed to be the homogeneity range for both 2-17*R* and 2-17*H* phases. The ratio between the two phases could be controlled by the annealing conditions, either decreasing or increasing the temperatures (in this case, 850℃ and 1250℃). Pure 2-17 phase was found to be difficult to obtain with the arc-melting technique. The single crystal refinements revealed the structures to be highly disordered and twinned. All the *RE* sites were partially occupied by Fe dumbbells.

Chapter 6: Physical and magnetic properties of $GdCo_4B$

6.1 Introduction

The $GdCo_4B$ compound, a member of the $CeCo_4B$-type structure (space group *P*6/*mmm*), can be derived from the $CaCu_5$-type structure by substituting the Co atoms on the 2*c* site located on every second Gd-Co layer with B atoms, thereby doubling the unit cell of the parent $GdCo_5$ structure in the *c* direction (**Figure 6.1**) [105]. Magnetic properties of the $R_{n+1}Co_{3n+5}B_{2n}$ (*R* = rare-earth elements or Y; *n* = 1, 2, 3 and ∞) series, which includes $GdCo_4B$ and the parent structure, have previously been studied by many due to the high magnetocrystalline anisotropy (MCA) behaviour that is crucial for permanent magnet applications [106–112]. The Gd-containing systems generate great fascination because the magnetic Gd ions have no orbital contribution, so they should theoretically not have any anisotropy contributions. However, when comparing to the non-magnetic Y-containing systems, experimental results from [113,114] observed discrepancies between the positive anisotropy contributions in the Gd (ferrimagnetic) and Y (ferromagnetic) systems in RCo_5 and RCo_4B. Nevertheless, the rare earth-transition metal interactions between the Gd localized 4*f* electrons and the Co 3*d* itinerant electrons result in interesting magnetic properties. Ido, H *et al.* reported spontaneous magnetostrictions in the *a* axis in the ferrimagnetic temperature region (T_C = 496 K) [115] . In this work, we present the studies of $GdCo_4B$ through single crystal and powder X-ray diffraction techniques. Bulk and lattice thermal expansions are measured by

dilatometer and synchrotron powder diffraction, respectively. Lastly, magnetization measurements will be outlined and discussed.

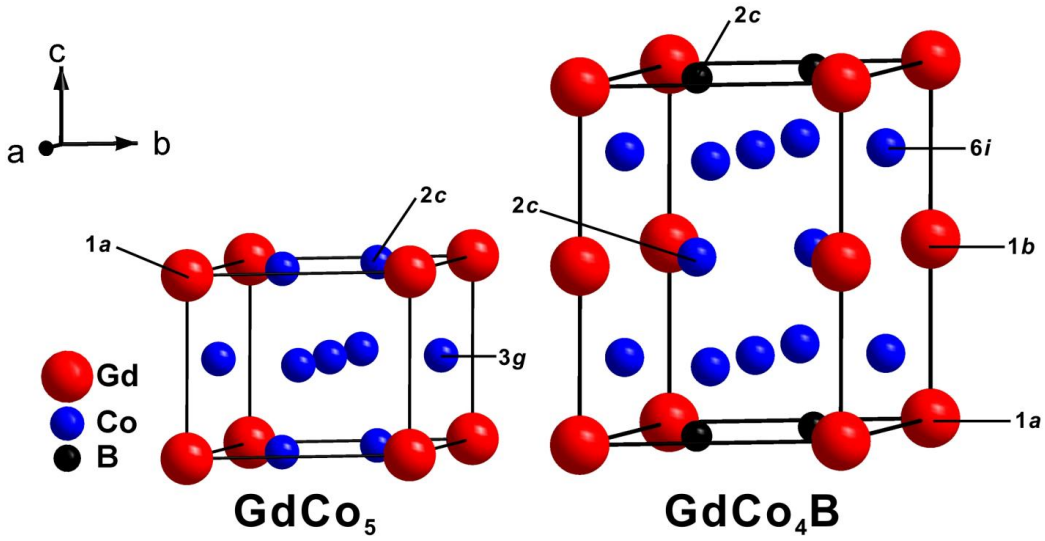

Figure 6.1 Crystal structures of the $GdCo_5$ (left) and $GdCo_4B$ (right) compounds.

The GdCo4B structure can be derived by substituting the Co atoms on the 2*c* site in the $GdCo_5$ structure with B atoms on alternating Gd-Co layers.

6.2 Experimental

The polycrystalline $GdCo_4B$ compound was prepared by arc-melting and the tri-arc Czochralski single crystal growth technique, as described in [116]. Stoichiometric amounts of Gd pieces (CERAC Inc., 99.9 wt %), Co shots (A.D. Mackay Inc., 99.8 wt %) and B metal lump (Atomergic Chemicals Corp., 99.9 wt %) were weighed to ~1 g and arc-melted four times under Ar atmosphere. The weight loss was less than 0.5 wt %.

Alternatively, the $GdCo_4B$ sample was grown using the tri-arc technique to an elongated rod-like shape crystal and dilatometer measurements were performed.

Dilatometer measurements were performed on a Linseis L75 Platinum Series horizontal push rod dilatometer in 15 seconds intervals to determine the linear thermal expansion (ΔL) of the $GdCo_4B$ sample situated in a sample holder connected to the push rod. The instrument was attached to a turbomolecular pump to ensure that the sample in the chamber was maintained under vacuum condition to prevent its oxidation. A solid piece of rod-like sample (at least 10 mm) was ramped from room temperature up to 673 K at 1 K/min, dwelled at 673 K for 60 minutes and then cooled back down to room temperature at 1 K/min. The data were plotted on a ΔL vs. temperature graph outlined in **Figure 6.2**.

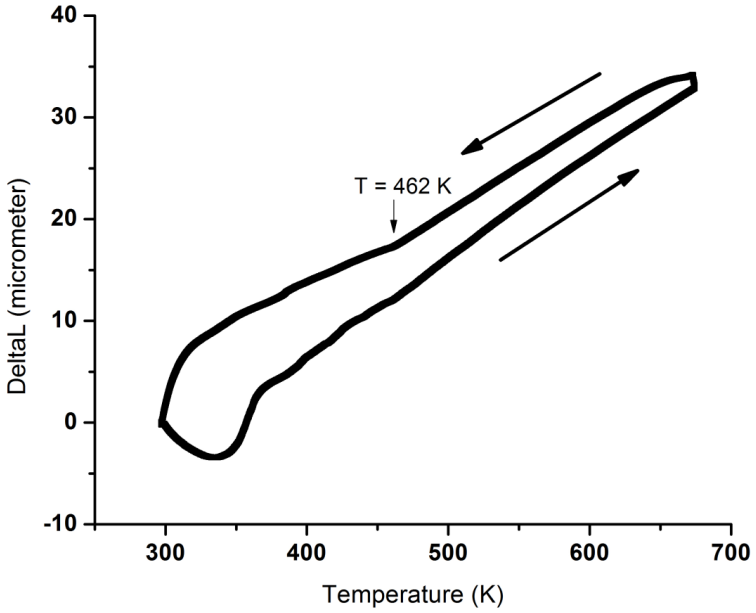

Figure 6.2 Linear thermal expansion data (ΔL) obtained from dilatometer measurement.

Powder X-ray phase analysis was performed on the PANalytical diffractometer with the Co *Kα* radiation. High temperature synchrotron powder diffraction data were collected on the tri-arc sample at the ESRF synchrotron, SNBL BM1A beamline with a MAR345 image-plate area detector with $\lambda = 0.6977(1)$ Å using a gas blower heater in the temperature ranges 290 - 500 K and 430 - 700 K with 1 K increments. The powder patterns were then refined using the FullProf software [13]. The refined lattice parameters (*a* and *c*) and unit cell volume of the $GdCo_4B$ phase were plotted as a function of temperature from 450 to 700 K (**Figure 6.3**).

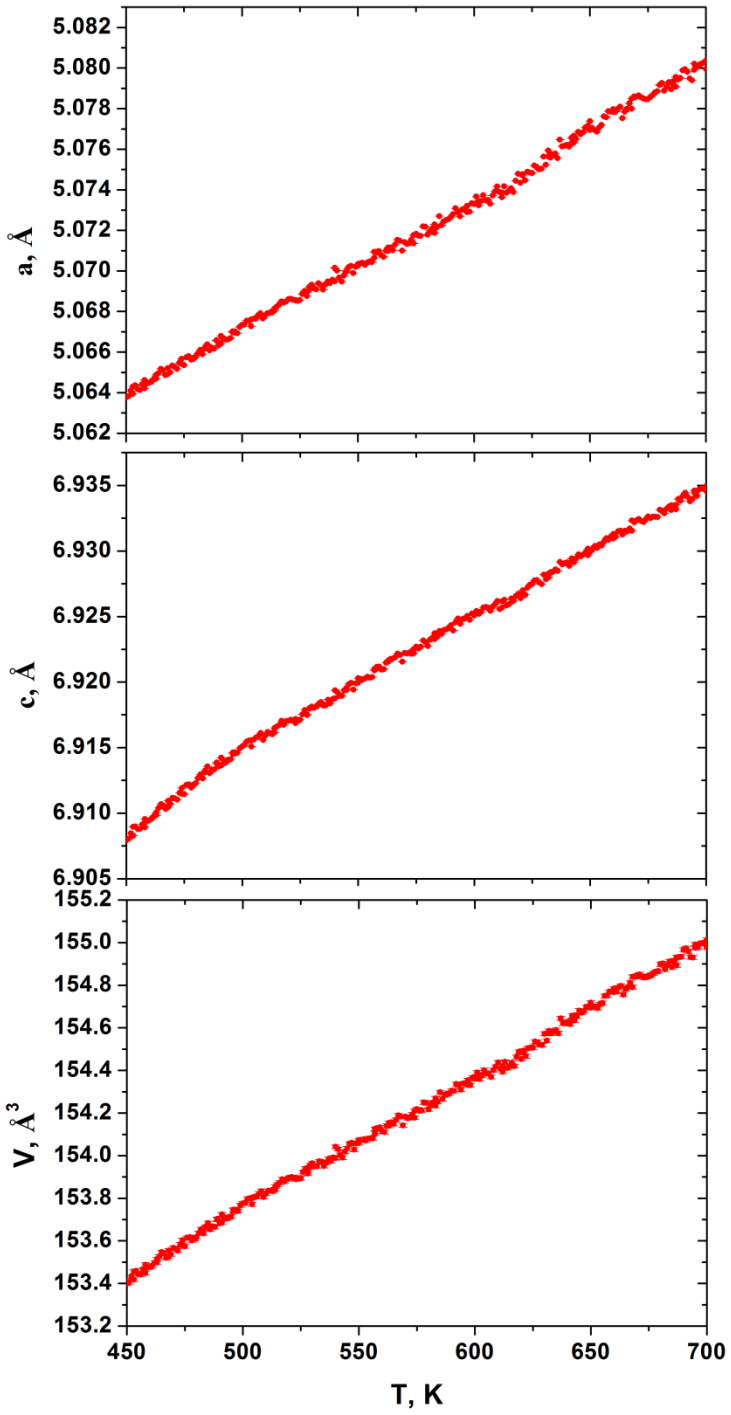

Figure 6.3 Refined lattice parameters *a* (top), *c* (middle) and unit cell volume (bottom) of the $GdCo_4B$ structure (with error bars) as a function of temperature ($450 \leq T \leq 700$ K).

Single crystal X-ray diffraction data for the $GdCo_4B$ cast and tri-arc samples were collected on a STOE IPDS II diffractometer using a Mo K_α radiation in the whole reciprocal sphere. The crystal structures were solved and refined using the *SHELXS* and *SHELXL* software package [15]. The atomic coordinates were standardized using the program STRUCTURE TIDY [77]. The refined structures crystallize in the hexagonal *P*6/*mmm* space group. Please refer to **Table 6.1** and **Table 6.2** for the crystal data and structural refinements. Further details of the crystal structures are available from the Fachinformationszentrum Karlsruhe, 76344 Eggenstein-Leopoldshafen, Germany, on quoting the depository number CSD–425077 and 425074 for the cast and tri-arc samples.

Table 6.1 Single crystal and refinement data obtained from the $GdCo_4B$ cast (left) and tri-arc (right) samples.

Loaded composition	$GdCo_4B$	$GdCo_4B$
Refined composition	$GdCo_4B$	$GdCo_4B$
Space group	*P*6/*mmm*	*P*6/*mmm*
Lattice parameters *a/c*, Å	5.0466(4) / 6.8749(6)	5.0472(7) / 6.879(1)
Volume, Å ^{3}	151.63(2)	151.76(4)
Crystal size, mm^3	0.0156 x 0.0498 x 0.0626	0.0235 x 0.0303 x 0.0588
2θ range for data collection, °	9.32 - 76.32	9.32 - 58.20
Index ranges	$-8 \le h \le 8$, $-8 \le k \le 8$, $-10 \le l \le 11$	$-6 \le h \le 6$, $-6 \le k \le 6$, $-7 \le l \le 9$
Reflections collected	3289	1713
Independent reflections	210 [R(int) = 0.0389]	113 [R(int) = 0.1510]
Completeness to max 2θ (%)	99.5	99.1
Data/restraints/parameters	210 / 0 / 14	113 / 0 / 14
Goodness-of-fit on F^2	1.207	1.116
Final R indices [I > 2σ(I)]	R_1 = 0.0323, wR_2 =	R_1 = 0.0475, wR_2 =

	0.0881	0.0976
R indices (all data)	R_1 = 0.0347, wR_2 = 0.0890	R_1 = 0.0673, wR_2 = 0.1052
Extinction coefficient	0.011(3)	0.008(4)
Largest diff. peak and hole (e/Å $^{-3}$)	4.095 and -2.176	2.614 and -2.575

Table 6.2 Atomic and isotropic temperature parameters (U, Å ^{2}) from single crystal X-ray diffraction data.

Atom	**Site**	**Occupancy**	***x/a***	***y/b***	***z/c***	***U***
			$GdCo_4B$ (cast)			
Gd1	1*a*	1	0	0	0	0.007(1)
Gd2	1*b*	1	0	0	1/2	0.010(1)
Co1	6*i*	1	1/2	0	0.2131(2)	0.008(1)
Co2	2*d*	1	1/3	2/3	1/2	0.013(1)
B1	2*c*	1	1/3	2/3	0	0.008(3)
			GdCo4B (tri-arc)			
Gd1	1*a*	1	0	0	0	0.026(1)
Gd2	1*b*	1	0	0	1/2	0.030(1)
Co1	6*i*	1	1/2	0	0.2133(4)	0.027(1)
Co2	2*d*	1	1/3	2/3	1/2	0.029(2)
B1	2*c*	1	1/3	2/3	0	0.05(2)

Magnetic measurement was performed on solid pieces of the cast and tri-arc $GdCo_4B$ samples on a SQUID (Superconducting Quantum Interference Device) magnetometer using a field cooled (FC) mode with an applied field of 100 Oe and a temperature range from 320 to 650 K. The magnetization vs. temperature plots are shown in **Figure 6.4** and **Figure 6.5**.

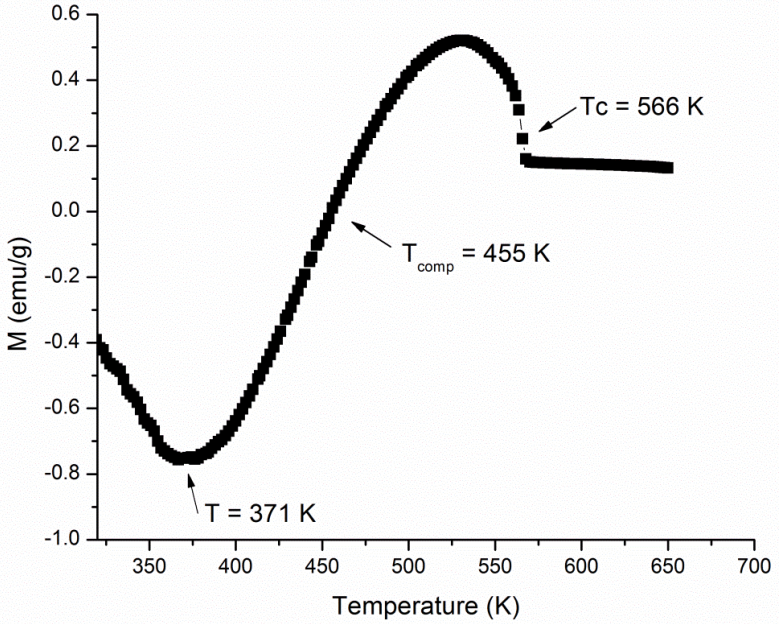

Figure 6.4 Magnetization vs. Temperature plot for the $GdCo_4B$ cast sample under an applied field of 100 Oe.

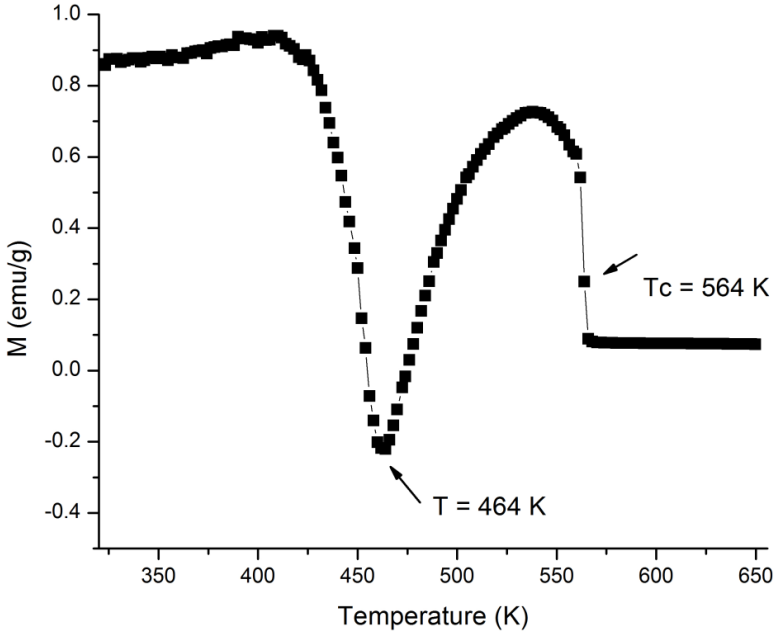

Figure 6.5 Magnetization vs. Temperature plot for the $GdCo_4B$ tri-arc sample under an applied field of 100 Oe.

6.3 Discussion

Based on the powder refinement results, the cast sample (**Figure 6.6**) contains the pure $GdCo_4B$ phase, while the tri-arc sample (**Figure 6.7**) contains a small amount of $GdCo_5$ impurity (less than 5% of the integrated intensity).

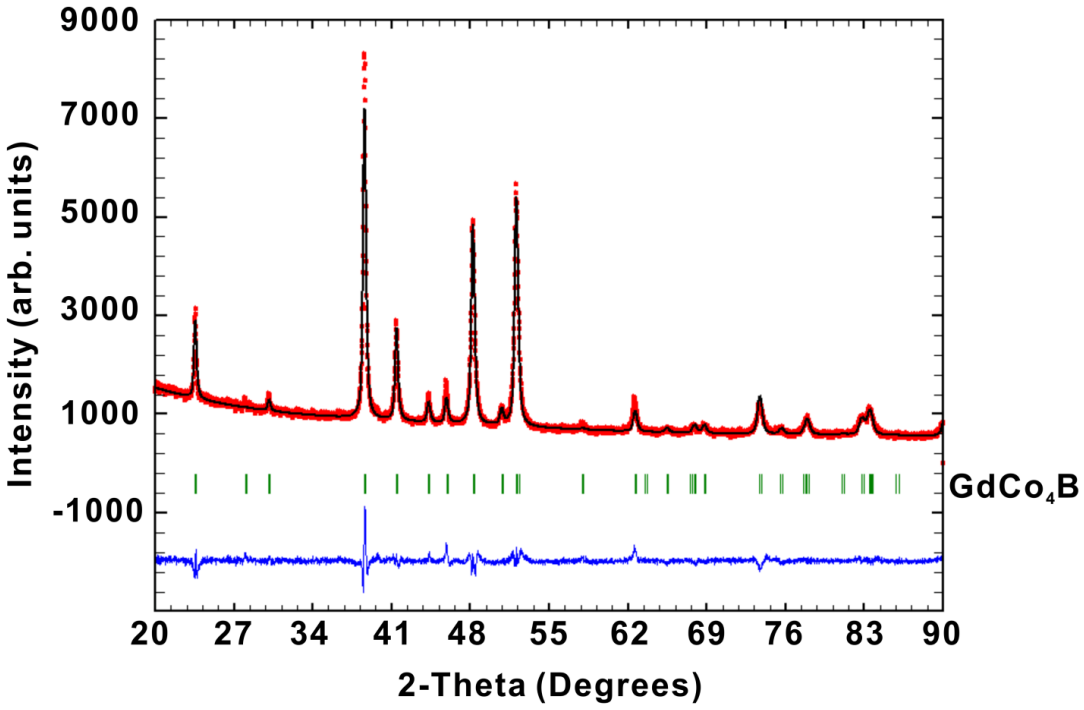

Figure 6.6 The refined powder X-ray pattern for the $GdCo_4B$ cast sample.

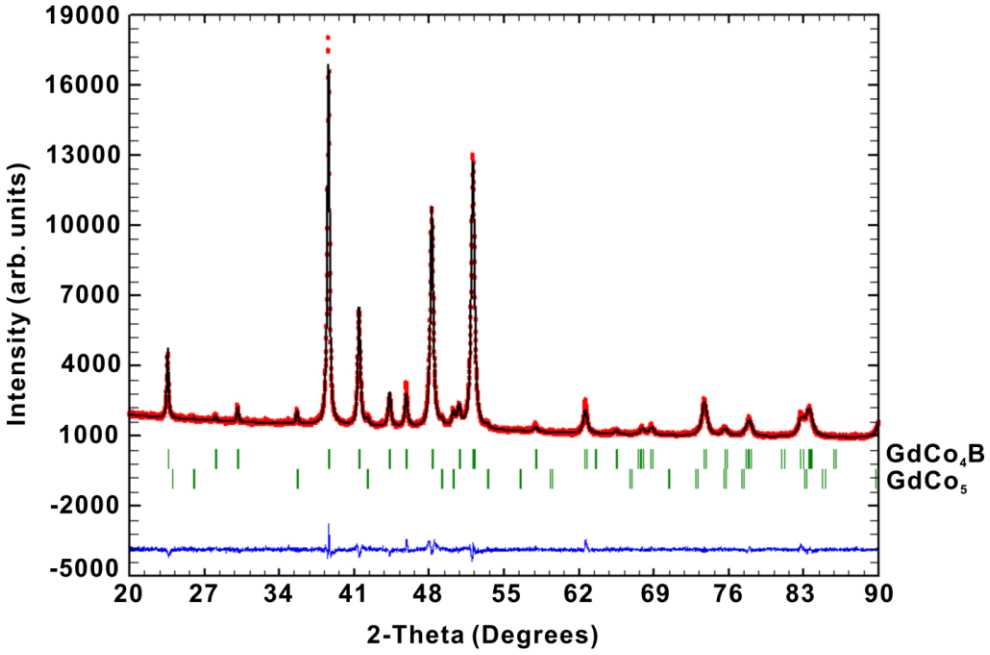

Figure 6.7 The refined powder X-ray pattern for the $GdCo_4B$ tri-arc sample.

The lattice parameters and atomic coordinates of the cast and tri-arc samples obtained from single crystal X-ray diffraction agreed well with literature [106,107]. All the atomic sites are solely occupied by one kind of atom within 3σ.

From the dilatometer measurement data, a small kink which resulted from the change of the sample shrinkage rate during the cooling process, was observed around 462 K. Spontaneous change in the *a* lattice parameter was also reported around this temperature in [115] as the magnetostriction phenomenon (T_C = 496 K).

The M vs. T plots for the cast (**Figure 6.4**) and tri-arc (**Figure 6.5**) samples seem unexpectedly different, but both display nearly identical magnetic transition temperatures, T_C = 566 K for the cast and T_C = 564 K for tri-arc samples. Consequently, no

magnetostriction was observed in this study. The T_C values obtained from this measurement are higher than all the T_C values reported previously in literature, which are between 496 K [115] and 517 K [106,110]. When compared to the magnetic behaviour of a typical ferrimagnet, the cast and tri-arc samples appear to behave differently possibly due to the low field (100 Oe) applied. The magnetic Gd and Co ions are extremely sensitive to the external field. Furthermore, there are multiple number of sublattices that are responsive to the magnetic field in this compound. There are four distinctive crystallographic sites for the Gd and Co atoms combined, which result in different local environments and magnetic responses for atoms located on each specific crystallographic site. The M vs. T plot of the cast sample (**Figure 6.4**) will first be discussed.

As the sample is field-cooled, there is a strong magnetization response coming from one of the sublattices at T_C = 566 K , where the magnetic spins are aligned in the up direction with the external field. This causes a behavioural change of the material from paramagnetic to ferromagnetic-like. Then, as the measurement continues, the magnetization response coming from the other sublattices that have the magnetic moments oriented in the opposite direction, increase. This translates to a decrease in the net magnetization. At 455 K, the material behaves truly like a ferrimagnet where the orientation of the magnetic moments from all the components cancel each other out and there is no net magnetic moment. The magnetization of the opposite component increases further in the down direction (denoted by negative magnetization values) as the material cools down. This continues until around 371 K where another magnetic component with magnetic moments in the up direction dominates and the magnetization increases.

For the tri-arc sample (**Figure 6.5**), the magnetization response in the paramagnetic region (T > 570) contains possible attributes from the $GdCo_5$ (T_C = 1020 K) [117] impurity phase, as seen by the higher than expected magnetization values. Below the Curie temperature, Tc = 564 K, the sublattice with magnetic moments oriented in the direction opposite to the field begins to get magnetized at T = 538 K. The change in the net magnetization direction results in the global minimum at T = 464 K. From Figure 4, two compensation points can be observed in this sample, T_{comp} = 455 and 474 K. The reason for the different magnetic behaviour of the sublattices in the tri-arc and cast samples may be due to the concentrations of Gd and Co in the $GdCo_4B$ phase are not equivalent in the two samples. This results in the magnetic spin alignment of the Gd and Co sublattices at different temperatures.

6.4 Conclusion

The $GdCo_4B$ sample was synthesized by arc-melt and the tri-arc techniques. Based on the high-temperature powder diffraction using a synchrotron source, the unit cell volume increased linearly as a function of temperature. From the dilatometer measurement, a small kink was observed around T = 462 K. Magnetic measurements of both the cast and tri-arc samples confirmed the magnetic transitions at T_C = 566 and 564 K, which are much larger than the ones reported from literature. In summary, no magnetostriction was observed in this experimental study.

References

[1] E. Warburg, *Ann. Phys*. (Leipzig) 13 (1881) 141.

[2] V.K. Pecharsky, K.A. Gschneidner, Jr., *J. Magn. Magn. Mater*. 200 (1999) 44.

[3] C. Zimm, A. Jastrab, A. Stemberg, V.K. Pecharsky, K.A. Gschneidner, Jr., M. Osborne, *Adv. Cryog. Eng*. 43 (1998) 1759.

[4] W.F. Giauque, D.P. MacDougall, *Phys. Rev*. 43 (1933) 768.

[5] V. Provenzano, A.J. Shapiro, R.D. Shull, *Nature*. 429 (2004) 853.

[6] G. Giovanna do Couto, V. Svitlyk, M. Jafelicci, Y. Mozharivskyj, *Solid State Sci*. 13 (2011) 209.

[7] V.K. Pecharsky, K.A. Gschneidner, Jr., *Phys. Rev. Lett*. 78 (1997) 4494.

[8] F. Holtzberg, R.J. Gambino, T.R. Mcguire, *J. Phys. Chem. Solids*. 28 (1967) 2283.

[9] V. Svitlyk, G.J. Miller, Y. Mozharivskyj, *J. Am. Chem. Soc*. 131 (2009) 2367.

[10] V. Svitlyk, Y.Y.J. Cheung, Y. Mozharivskyj, *J. Magn. Magn. Mater*. 322 (2010) 2558.

[11] Y. Mozharivskyj, W. Choe, A.O. Pecharsky, G.J. Miller, *J. Am. Chem. Soc*. 125 (2003) 15183.

[12] V.K. Pecharsky, P.Y. Zavalij, Fundamentals of Powder Diffraction and Structural Characterization of Materials, 2nd ed., Springer Science and Business Media, LLC, New York, 2009.

[13] J. Rodriguez-Carvajal, IUCr Newsletter 26 (2001) 12.

[14] STOE & Cie GmbH, Germany, Darmstadt, (2004).

[15] G.M. Sheldrick, SHELXS-97 - Program for the Solution of Crystal Structures, University of Gottingen, Germany, 1997.

[16] S. Misra, G.J. Miller, *J. Am. Chem. Soc*. 130 (2008) 13900.

[17] L. Morellon, C. Magen, P.A. Algarabel, M.R. Ibarra, C. Ritter, *Appl. Phys. Lett*. 79 (2001) 1318.

[18] C. Ritter, L. Morellon, P.A. Algarabel, C. Magen, M.R. Ibarra, *Phys. Rev. B.* 65 (2002) 094405.

[19] L. Wu, S. Kim, D. Seo, *J. Am. Chem. Soc*. 127 (2005) 15682.

[20] P.H. Tobash, S. Bobev, *J. Am. Chem. Soc*. 128 (2006) 3532.

[21] X.J. Niu, K.A. Gschneidner, Jr., A.O. Pecharsky, V.K. Pecharsky, *J. Magn. Magn. Mater*. 234 (2001) 193.

[22] E.M. Levin, K.A.G. Jr, V.K. Pecharsky, *J. Magn. Magn. Mater*. 231 (2001) 135.

[23] V.K. Pecharsky, K.A. Gschneidner, Jr., *Adv. Mater*. 231 (2001) 683.

[24] V.K. Pecharsky, A.P. Holm, K.A. Gschneidner, Jr., R. Rink, *Phys. Rev. Lett*. 91 (2003) 197204.

[25] V. Svitlyk, B.J. Campbell, Y. Mozharivskyj, *Inorg. Chem*. 48 (2009) 10364.

[26] S. Misra, Y. Mozharivskyj, A.O. Tsokol, D.L. Schlagel, T.A. Lograsso, G.J. Miller, *J. Solid State Chem*. 182 (2009) 3031.

[27] P. Villars, L.D. Calvert, Pearson's Handbook of Crystallographic Data for Intermetallic Phases, ASM International, Materials Park, Ohio, 1991.

[28] P.S. Chizhov, N.R. Khasanova, M. Baitinger, W. Schnelle, Y. Prots, U. Burkhardt, E.V. Antipov, Y. Grin, *Inorg. Chem*. 45 (2006) 7210.

[29] V. Svitlyk, Y. Mozharivskyj, *Solid State Sci*. 11 (2009) 1941.

[30] R.J. Gambino, *J. Less-Common Met*. 12 (1967) 344.

[31] K. Yoshihara, J.B. Taylor, L.D. Calvert, J.G. Despault, *J. Less-Common Met*. 41 (1975) 329.

[32] O. Jepsen, A. Burkhardt, O.K. Andersen, The TB-LMTO-ASA Program, Max-Planck-Institut für Festkrperforschung, Stuttgart, Germany, 1999.

[33] W.R.L. Lambrecht, O.K. Andersen, *Phys. Rev. B.* 34 (1986) 2439.

[34] J. Yao, P. Wang, Y. Mozharivskyj, *Chem. Mater*. 24 (2012) 552.

[35] O.K. Andersen, O. Jepsen, *Phys. Rev. Lett*. 53 (1984) 2571.

[36] P.E. Blochl, O. Jepsen, O.K. Andersen, *Phys. Rev. B*. 49 (1994) 16223.

[37] E. Zintl, *Angew. Chem*. 52 (1939) 1.

[38] H. Schäfer, B. Eisenmann, W. Muller, *Angew. Chem. Int. Ed*. 12 (1973) 694.

[39] G.J. Miller, Chemistry, Structure and Bonding of Zintl Phases and Ions, VCH Publishers, New York, 1996.

[40] L. Pauling, The Nature of the Chemical Bond and the Structure of Molecules and Crystals: An Introduction to Modern Structural Chemistry, 3rd ed., Cornell University Press, Ithaca, NY, 1960.

[41] K.A. Lynchak, Y.B. Kuz'ma, T.Y. Kosolapova, *Porosh-kovaya Metallurgiya*. 12 (1968) 42.

[42] T. Tsutaoka, Y. Nishiume, T. Tokunaga, *J. Magn. Magn. Mater*. 272-276 (2004) E421.

[43] R.E. Treece, J.A. Conklin, R.B. Kaner, *Inorg. Chem*. 33 (1994) 5701.

[44] F. Hulliger, H.R. Ott, *J. Less-Common Met*. 55 (1977) 103.

[45] T. Kasuya, *Prog. Theor. Phys*. 16 (1956) 45.

[46] M.A. Ruderman, C. Kittel, *Phys. Rev*. 96 (1954) 99.

[47] K. Yosida, *Phys. Rev*. 106 (1957) 893.

[48] V.K. Pecharsky, K.A. Gschneidner, Jr., *Appl. Phys. Lett*. 70 (1997) 3299.

[49] L. Morellon, P.A. Algarabel, M.R. Ibarra, J. Blasco, B. Garcia-Landa, Z. Arnold, F. Albertini, *Phys. Rev. B*. 58 (1998) R14721.

[50] L. Morellon, J. Blasco, P.A. Algarabel, M.R. Ibarra, *Phys. Rev. B*. 62 (2000) 1022.

[51] L. Morellon, J. Stankiewicz, B. García-Landa, P.A. Algarabel, M.R. Ibarra, *Appl. Phys. Lett*. 73 (1998) 3462.

[52] E.M. Levin, V.K. Pecharsky, K.A. Gschneidner, Jr., *Phys. Rev. B*. 60 (1999) 7993.

[53] C. Magen, L. Morellon, P.A. Algarabel, C. Marquina, M.R. Ibarra, *J. Phys.: Condens. Matter*. 15 (2003) 2389.

[54] H. Tang, V.K. Pecharsky, G.D. Samolyuk, M. Zou, K.A. Gschneidner, Jr., V.P. Antropov, D.L. Schlagel, T.A. Lograsso, *Phys. Rev. Lett*. 93 (2004) 237203.

[55] W. Choe, V.K. Pecharsky, A.O. Pecharsky, K.A. Gschneidner, Jr., V.G. Young, Jr., G.J. Miller, *Phys. Rev. Lett*. 84 (2000) 4617.

[56] G.S. Smith, A.G. Tharp, Q. Johnson, *Nature*. 210 (1966) 1148.

[57] G.S. Smith, Q. Johnson, A.G. Tharp, *Acta Crystallogr*. 22 (1967) 269.

[58] A.O. Pecharsky, K.A. Gschneidner, Jr., V.K. Pecharsky, C.E. Schindler, *J. Alloys. Compd*. 338 (2002) 126.

[59] C. Magen, Z. Arnold, L. Morellon, Y. Skorokhod, P.A. Algarabel, M.R. Ibarra, J. Kamarad, *Phys. Rev. Lett*. 91 (2003) 207202.

[60] Y. Mudryk, D. Paudyal, V.K. Pecharsky, K.A. Gschneidner, Jr., *Phys. Rev. B*. 77 (2008) 024408.

[61] E.M. Levin, V.K. Pecharsky, K.A. Gschneidner, Jr., G.J. Miller, *Phys. Rev. B*. 64 (2001) 235103.

[62] R.B. Griffiths, *Phys. Rev. Lett*. 23 (1969) 17.

[63] Z.W. Ouyang, V.K. Pecharsky, K.A. Gschneidner, Jr., D.L. Schlagel, T.A. Lograsso, *Phys. Rev. B*. 74 (2006) 094404.

[64] N. Pérez, F. Casanova, F. Bartolomé, L. García, A. Labarta, X. Batlle, *Phys. Rev. B*. 83 (2011) 184411.

[65] S.B. Roy, M.K. Chattopadhyay, P. Chaddah, J.D. Moore, G.K. Perkins, L.F. Cohen, K. a. Gschneidner, V.K. Pecharsky, *Phys. Rev. B*. 74 (2006) 012403.

[66] M. Manekar, M.K. Chattopadhyay, R. Kaul, V.K. Pecharsky, K.A. Gschneidner, Jr., *J. Phys.: Condens. Matter*. 18 (2006) 6017.

[67] S. Velez, J.M. Hernandez, A. Fernandez, F. Macià, C. Magen, P.A. Algarabel, J. Tejada, E.M. Chudnovsky, *Phys. Rev. B*. 81 (2010) 064437.

[68] A.Y. Kozlov, V.V. Pavlyuk, V.M. Davydov, *Intermetallics*. 12 (2004) 151.

[69] H. Wang, S. Misra, F. Wang, G.J. Miller, *Inorg. Chem*. 49 (2010) 4586.

[70] A.S. Chernyshov, Y.S. Mudryk, V.K. Pecharsky, K.A. Gschneidner, Jr., *J. Appl. Phys*. 99 (2006) 08Q102.

[71] A.S. Chernyshov, Y. Mudryk, D. Paudyal, V.K. Pecharsky, K.A. Gschneidner, Jr., D.L. Schlagel, T.A. Lograsso, *Phys. Rev. B*. 80 (2009) 184416.

[72] J. Yao, P. Lyutyy, Y. Mozharivskyj, *Dalton Trans*. 40 (2011) 4275.

[73] J. Yao, Y. Mozharivskyj, *Z. Anorg. Allg. Chem*. 637 (2011) 2039.

[74] J. Yao, P.L. Wang, Y. Mozharivskyj, *J. Alloys. Compd*. 534 (2012) 74.

[75] Y.Y.J. Cheung, V. Svitlyk, Y. Mozharivskyj, *Intermetallics*. 19 (2011) 276.

[76] J.B. Mann, T.L. Meek, L.C. Allen, *J. Am. Chem. Soc*. 122 (2000) 2780.

[77] L.M. Gelato, E. Parthé, *J. Appl. Cryst*. 20 (1987) 139.

[78] Y. Mozharivskyj, A.O. Tsokol, G.J. Miller, *Z. Kristallogr*. 221 (2006) 493.

[79] G.J. Miller, *Eur. J. Inorg. Chem*. (1998) 523.

[80] Y. Mudryk, D. Paudyal, V. Pecharsky, K. Gschneidner, *Phys. Rev. B*. 85 (2012) 014116.

[81] B.N. Harmon, A.J. Freeman, *Phys. Rev. B*. 10 (1974) 1979.

[82] L.W. Roeland, G.J. Cock, F.A. Muller, A.C. Moleman, K.A. McEwen, R.G. Jordan, D.W. Jones, *J. Phys. F: Metal Phys*. 5 (1975) L233.

[83] F. Casanova, S.D. Brion, A. Labarta, X. Batlle, *J. Phys. D: Appl. Phys*. 38 (2005) 3343.

[84] Y.C. Tseng, D. Haskel, N.M. Souza-Neto, Y. Mudryk, V.K. Pecharsky, K.A. Gschneidner, Jr., *Phys. Rev. B*. 78 (2008) 214433.

[85] L. Tan, A. Kreyssig, J.W. Kim, A.I. Goldman, R.J. McQueeney, D. Wermeille, B. Sieve, T. a. Lograsso, D.L. Schlagel, S.L. Budko, V.K. Pecharsky, K.A. Gschneidner, Jr., *Phys. Rev. B*. 71 (2005) 214408.

[86] D. Ryan, J. Cadogan, L. Cranswick, K. Gschneidner, V. Pecharsky, Y. Mudryk, *Phys. Rev. B*. 82 (2010) 224405.

[87] E.M. Levin, V.K. Pecharsky, K.A. Gschneidner Jr., *Phys. Rev. B*. 62 (2000) R14625.

[88] C. Magen, P.A. Algarabel, L. Morellon, J.P. Araújo, C. Ritter, M.R. Ibarra, a. M. Pereira, J.B. Sousa, *Phys. Rev. Lett*. 96 (2006) 167201.

[89] R. Nirmala, Y. Mudryk, V.K. Pecharsky, K.A. Gschneidner, Jr., *Phys. Rev. B*. 76 (2007) 104417.

[90] Z.W. Ouyang, *J. Appl. Phys*. 108 (2010) 033907.

[91] J. Deisenhofer, D. Braak, H.-A. Krug von Nidda, J. Hemberger, R.M. Eremina, V.A. Ivanshin, A.M. Balbashov, G. Jug, A. Loidl, T. Kimura, Y. Tokura, *Phys. Rev. Lett*. 95 (2005) 257202.

[92] K. Strnat, G. Hoffer, J. Olson, W. Ostertag, *J. Appl. Phys*. 38 (1967) 1001.

[93] G. Bruzzone, *J. Less-Common Met*. 25 (1971) 361.

[94] K.H.J. Buschow, A.S. Van Der Goot, *Acta Cryst*. B27 (1971) 1085.

[95] Y.V. Shcherbakova, G.V. Ivanova, N.V. Mushnikov, I.V. Gervasieva, *J. Alloys. Compd*. 308 (2000) 15.

[96] A.V. Lukoyanov, E.E. Kokorina, M.V. Medvedev, I.A. Nekrasov, *Phys. Rev. B*. 80 (2009) 104409.

[97] B. Shen, B. Liang, Z. Cheng, H. Gong, S. Zhang, L. Zhang, *J. Phys. D: Appl. Phys*. 31 (1998) 2438.

[98] Y.V. Knyazev, A.V. Lukoyanov, Y.I. Kuz'min, A.G. Kuchin, I.A. Nekrasov, *Phys. Rev. B.* 73 (2006) 094410.

[99] M.P. Dariel, J.T. Holthuis, M.R. Pickus, *J. Less-Common Met*. 45 (1976) 91.

[100] J.L. Chen, G.H. Wu, D.Q. Zhao, S.X. Gao, W.S. Zhan, Y.X. Li, J.P. Qu, G.Z. Xu, *J. Cryst. Growth*. 222 (2001) 779.

[101] W.G. Haije, T.H. Jacobs, K.H.J. Buschow, *J. Less-Common Met*. 163 (1990) 353.

[102] F. Wang, B. Shen, P. Zhang, Z. Cheng, J. Zhang, H. Gong, B. Liang, X. Sun, Q. Yan, *J. Appl. Phys*. 83 (1998) 3250.

[103] O. Kubaschewski, Iron-Binary Phase Diagrams, Springer-Verlag, Berlin, 1982.

[104] L. Schramm, J. Acker, K. Wetzig, *J. Alloys. Compd*. 414 (2006) 158.

[105] Y.B. Kuzma, N.S. Bilonizko, *Kristallographiya*. 18 (1973) 710.

[106] F. Spada, C. Abache, H. Oesterreicher, *J. Less-Common Met*. 99 (1984) L21-L24.

[107] A.T. Pedziwiatr, S.Y. Jiang, W.E. Wallace, E. Burzo, V. Pop, *J. Magn. Magn. Mater*. 66 (1987) 69.

[108] Z. Drzazga, A. Winiarska, K. Borgiel, T. Mydlarz, *J. Magn. Magn. Mater*. 83 (1990) 155.

[109] E. Burzo, V. Pop, N. Plugaru, *J. Magn. Magn. Mater*. 97 (1991) 147.

[110] T. Ito, H. Ogata, H. Ido, G. Kido, *J. Appl. Phys*. 73 (1993) 5914.

[111] C.V. Thang, N.P. Thuy, J.P. Liu, N.T. Hien, T.D. Hien, *J. Magn. Magn. Mater*. 147 (1995) 55.

[112] Z.G. Zhao, F.R. de Boer, K.H.J. Buschow, *J. Alloys. Compd*. 278 (1998) 69.

[113] R. Ballou, J. Deportes, B. Gorges, R. Lemaire, J.C. Ousset, *J. Magn. Magn. Mater*. 54-57 (1986) 465.

[114] Z. Drzazga, K. Biaas-Borgie, W. Borgie, *J. Magn. Magn. Mater*. 101 (1991) 399.

[115] H. Ido, Y. Suzuki, T. Suzuki, *J. Appl. Phys*. 83 (1998) 7133.

[116] J.E. Barnes, K.P. Trumble, *J. Cryst. Growth*. 160 (1996) 66.

[117] E. Burzo, *Phys. Rev. B*. 6 (1972) 2882.